PB-246 215

ATMOSPHERIC TURBULENCE PROPERTIES IN THE LOWEST 300 METERS

A. H. Weber, et al

North Carolina State University

Prepared for:

Environmental Sciences Research Laboratory

July 1975

DISTRIBUTED BY:

NTIS

National Technical Information Service
U. S. DEPARTMENT OF COMMERCE

PB 246 215
310138

EPA-600/4-75-004
July 1975

Environmental Monitoring Series

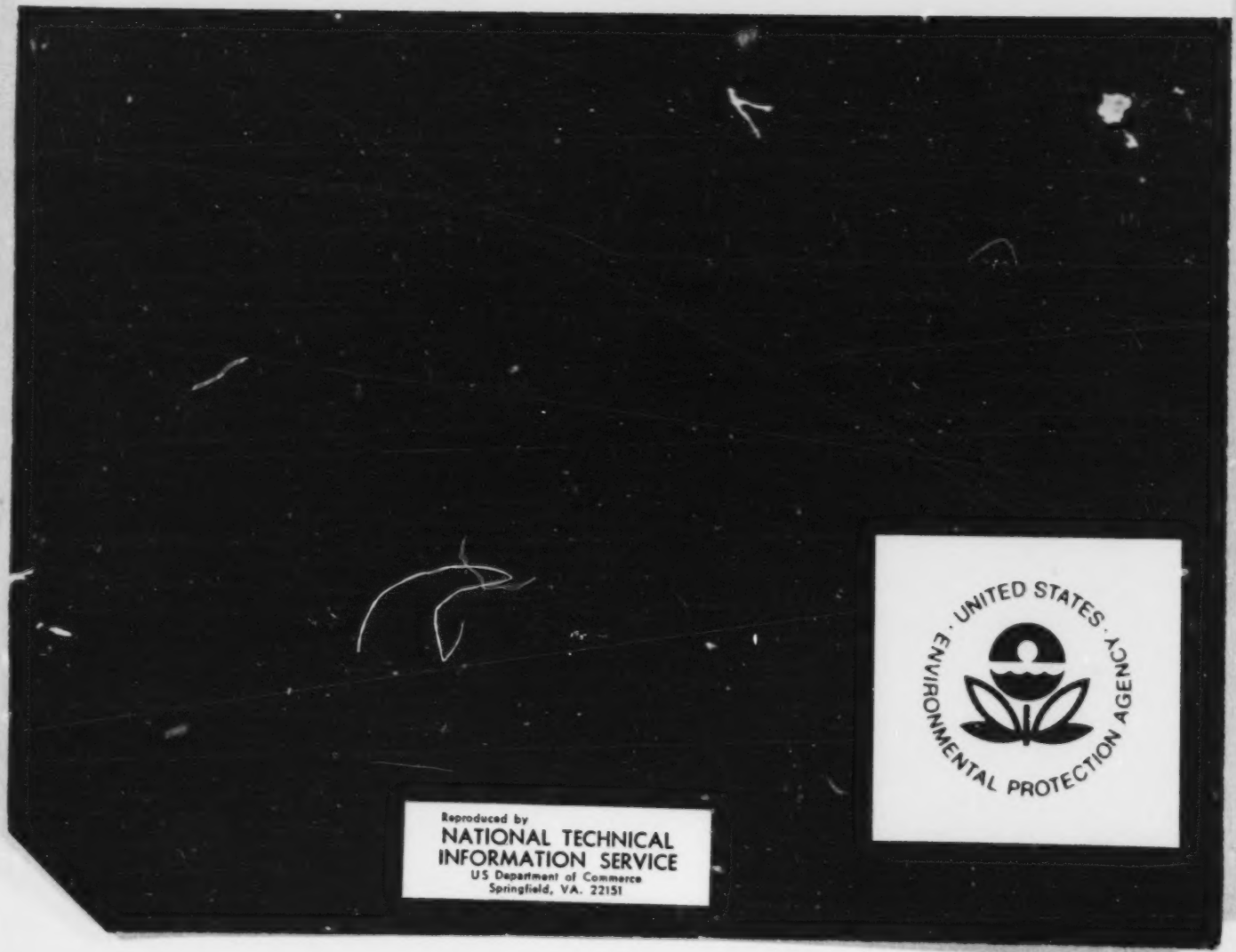

Reproduced by
NATIONAL TECHNICAL
INFORMATION SERVICE
US Department of Commerce
Springfield, VA. 22151

TECHNICAL REPORT DATA
(Please read Instructions on the reverse before completing)

1. REPORT NO.	2.	3. RECIPIENT'S ACCESSION NO.
EPA-600/4-75-004		

4. TITLE AND SUBTITLE	5. REPORT DATE
ATMOSPHERIC TURBULENCE PROPERTIES IN THE LOWEST 300 METERS	July 1975
	6. PERFORMING ORGANIZATION CODE: 65050

7. AUTHOR(S)	8. PERFORMING ORGANIZATION REPORT NO.
A.H. Weber, J.P. Kahler, J.S. Irwin, and W.B. Petersen	

9. PERFORMING ORGANIZATION NAME AND ADDRESS	10. PROGRAM ELEMENT NO.
North Carolina State University Raleigh, N. C. 27607	1AA009
	11. CONTRACT/GRANT NO.: 800662

12. SPONSORING AGENCY NAME AND ADDRESS	13. TYPE OF REPORT AND PERIOD COVERED
Meteorology & Assessment Division, ESRL (MD-80) Environmental Protection Agency Research Triangle Park, N. C. 27711	Final
	14. SPONSORING AGENCY CODE

15. SUPPLEMENTARY NOTES

16. ABSTRACT

Analyses of atmospheric turbulence data for a nonhomogeneous terrain collected at the SRL-WJBJ Meteorological Facility at Beach Island, South Carolina, are presented. Variations of the turbulence parameters are studied within and above the surface layer.

17. KEY WORDS AND DOCUMENT ANALYSIS

a. DESCRIPTORS	b. IDENTIFIERS/OPEN ENDED TERMS	c. COSATI Field/Group
Turbulence 2004 Atmospheric Diffusion	Atmospheric Turbulence Properties-Lowest 300 Meters	Atmospheric Diffusion Atmospheric Physics

18. DISTRIBUTION STATEMENT	19. SECURITY CLASS (This Report)	21. NO. OF PAGES
Release Unlimited	None	164
	20. SECURITY CLASS (This page): None	22. PRICE: 6.25

EPA Form 2220-1 (9-73)

EPA-600/4-75-004

ATMOSPHERIC TURBULENCE PROPERTIES IN THE LOWEST 300 METERS

by

A.H. Weber, J.S. Irwin,
J.P. Kahler, and W.B. Petersen

North Carolina State University
Raleigh, N. C.

Grant No. 800662
ROAP No. 21ADO-33
Program Element No. 1AA009

EPA Project Officer: George W. Griffing

Environmental Sciences Research Laboratory
Office of Air, Land, and Water Use
Research Triangle Park, N. C. 27711

Prepared for

U.S. ENVIRONMENTAL PROTECTION AGENCY
Office of Research and Development
Washington, D. C. 20460

July 1975

1a)

EPA REVIEW NOTICE

This report has been reviewed by the National Environmental Research Center - Research Triangle Park, Office of Research and Development, EPA, and approved for publication. Approval does not signify that the contents necessarily reflect the views and policies of the Environmental Protection Agency, nor does mention of trade names or commercial products constitute endorsement or recommendation for use.

RESEARCH REPORTING SERIES

Research reports of the Office of Research and Development, U.S. Environmental Protection Agency, have been grouped into series. These broad categories were established to facilitate further development and application of environmental technology. Elimination of traditional grouping was consciously planned to foster technology transfer and maximum interface in related fields. These series are:

1. ENVIRONMENTAL HEALTH EFFECTS RESEARCH
2. ENVIRONMENTAL PROTECTION TECHNOLOGY
3. ECOLOGICAL RESEARCH
4. ENVIRONMENTAL MONITORING
5. SOCIOECONOMIC ENVIRONMENTAL STUDIES
6. SCIENTIFIC AND TECHNICAL ASSESSMENT REPORTS
9. MISCELLANEOUS

This report has been assigned to the ENVIRONMENTAL MONITORING series. This series describes research conducted to develop new or improved methods and instrumentation for the identification and quantification of environmental pollutants at the lowest conceivably significant concentrations. It also includes studies to determine the ambient concentrations of pollutants in the environment and/or the variance of pollutants as a function of time or meteorological factors.

This document is available to the public for sale through the National Technical Information Service, Springfield, Virginia 22161.

Publication No. EPA-600/4-75-004

ABSTRACT

Results of analyses of atmospheric turbulence data collected from the SRL-WJBF Meteorological Facility at Beach Island, South Carolina, are presented. The results include the variation of turbulence parameters both within and above the surface layer. The nondimensional wind shear, ϕ_m, is plotted with respect to the ratio of height, z, and Monin-Obukhov length, L. Roughness lengths for two fetches are obtained. Standard deviations of wind elevation, σ_E, and azimuth, σ_A, and σ_E/σ_A are plotted versus the stability parameter z/L. The approximate relationships involving standard deviations of the vertical and lateral wind components, σ_w and σ_v, respectively, and mean vector wind speed U, e.g., $\sigma_w \approx U\sigma_E$ and $\sigma_v \approx U\sigma_A$, are investigated and found to be very accurate in almost all circumstances. The ratio σ_w/u_*, where u_* is surface friction velocity, is found to agree with previous measurements. The variable σ_E is found to be a function of the scaling parameter fz/u_*, where f is the Coriolis parameter, in near neutral stability conditions. Averages of eddy viscosity are plotted with height and stability. The ratio of momentum and heat diffusivities, K_m/K_h, is presented as a function of z/L. The spectral scale, λ_m, and the mixing length are studied and found to be consistent with the results of Pasquill (1972). Properties of spectra measured at 18.3 meters are investigated and found to agree well with previously published results. The turbulence energy budget and dimensionless temperature gradient are compared with other investigators' results.

CONTENTS

		Page
List of Figures		v
List of Tables		viii
Acknowledgments		ix
Sections		
I	Glossary	1
II	Conclusions	4
III	Recommendations	7
IV	Introduction	8
V	Application to Diffusion	9
VI	Tower and Terrain	11
VII	Instruments	14
VIII	Experiment	16
IX	Data Processing	17
X	Surface Friction Velocity	21
XI	Nondimensional Wind Shear, ϕ_m	24
XII	ϕ_m versus z/L For Near Neutral Stabilities	39
XIII	Roughness Lengths	42
XIV	σ_E, σ_A, and σ_E/σ_A versus z/L	45
XV	Transformation Ratios	54
XVI	σ_w/u_*	66
XVII	The Scaling Parameter fz/u_*	74
XVIII	Eddy Viscosity	88
XIX	Ratio of Eddy Diffusivities	91
XX	Spectral Scale, Λ_m, of the Vertical Component and Mixing Length	94
XXI	Spectral Ratios	98
XXII	Normalized Turbulence Velocity Spectra	106
XXIII	The Kolmogorov Constant	112
XXIV	Energy Budget Theory and Dissipation of Turbulence Energy	115
XXV	Dimensionless Temperature Gradient, ϕ_h	126
XXVI	References	140
XXVII	Appendices	144

LIST OF FIGURES

No.		Page
1.	Terrain at SRL-WJBF Tower	13
2.	Plot of u_* - Bivane and Cup Anemometer, Versus u_* - Gill Anemometer	22
3.	Nondimensional Wind Shear, ϕ_m, Versus z/L, $\bar{z}$ = 45.4 m - Method 1	26
4.	ϕ_m Versus z/L, $\bar{z}$ = 113.0 m - Method 1	27
5.	ϕ_m Versus z/L, $\bar{z}$ = 158.9 m - Method 1	28
6.	ϕ_m Versus z/L, $\bar{z}$ = 211.8 m - Method 1	29
7.	ϕ_m Versus z/L, $\bar{z}$ = 273.2 m - Method 1	30
8.	ϕ_m Versus z/L, 54.9 m - Method 2	33
9.	ϕ_m Versus z/L, 114.3 m - Method 2	34
10.	ϕ_m Versus z/L, 160.1 m - Method 2	35
11.	ϕ_m Versus z/L, 213.0 m - Method 2	36
12.	ϕ_m Versus z/L, 274.3 m - Method 2	37
13.	ϕ_m Versus z/L, Near Neutral - Method 1	40
14.	ϕ_m Versus z/L, Near Neutral - Method 2	41
15.	Ln(z) - ψ(z/L) Versus Mean Wind Speed	44
16.	σ_A Versus z/L for South Winds	46
17.	σ_A Versus z/L for Southwest Winds	47
18.	σ_E Versus z/L for South Winds	49
19.	σ_E Versus z/L for Southwest Winds	50
20.	σ_E/σ_A Versus z/L for South Winds	52
21.	σ_E/σ_A Versus z/L for Southwest Winds	53
22.	σ_w/σ_E Versus Magnitude of Mean Vector Wind, U	55
23.	σ_v/σ_A Versus Magnitude of Mean Vector Wind, U	56

No.		Page
24.	σ_u/σ_A Versus Magnitude of Mean Vector Wind, U	57
25.	σ_w/σ_E Versus U - Data Removed by Editing	61
26.	σ_v/σ_A Versus U - Data Removed by Editing	62
27.	σ_u/σ_A Versus U - Data Removed by Editing	63
28.	σ_w/u_*(Local) Versus z/L at 18.3 m	68
29.	σ_w/u_*(Local) Versus z/L at 91.4 m	69
30.	σ_w/u_*(Local) Versus z/L at 304.8 m	70
31.	σ_w/u_*(Surface) Versus z/L at 18.3 m	71
32.	σ_w/u_*(Surface) Versus z/L at 91.4 m	72
33.	σ_w/u_*(Surface) Versus z/L at 304.8 m	73
34.	σ_E Versus fz/u_* For All Levels - Near Neutral	76
35.	σ_A Versus fz/u_* For All Levels - Near Neutral	77
36.	σ_E Versus fz/u_* For All Levels - Stable	83
37.	σ_A Versus fz/u_* For All Levels - Stable	84
38.	σ_E Versus fz/u_* For All Levels - Unstable	85
39.	σ_A Versus fz/u_* For All Levels - Unstable	86
40.	Eddy Viscosity Profile	90
41.	Ratio of Momentum and Heat Diffusivity Versus z/L	93
42.	λ(Max) Profile	96
43.	Mixing Length Profile	97
44.	$S_w(n)/S_u(n)$ Versus Nondimensional Frequency - Logarithmic Plot	102
45.	$S_w(n)/S_u(n)$ Versus Nondimensional Frequency - Linear Plot	103
46.	$S_v(n)/S_u(n)$ Versus Nondimensional Frequency - Logarithmic Plot	104
47.	$S_v(n)/S_u(n)$ Versus Nondimensional Frequency - Linear Plot	105
48.	Normalized w Spectra Versus Nondimensional Frequency	108
49.	Normalized v Spectra Versus Nondimensional Frequency	109

No.		Page
50.	Normalized u Spectra Versus Nondimensional Frequency	111
51.	Observed ϵ Versus Calculated ϵ	121
52.	Nondimensional Dissipation Versus z/L at 18.3 m - Sonic	123
53.	Nondimensional Dissipation Versus z/L - Cup & Bivane	124
54.	ϕ_h Versus z/L at 18.3 m - Method 1	128
55.	ϕ_h Versus z/L at 91.4 m - Method 1	129
56.	ϕ_h Versus z/L at 137.2 m - Method 1	130
57.	ϕ_h Versus z/L at 182.9 m - Method 1	131
58.	ϕ_h Versus z/L at 243.8 m - Method 1	132
59.	ϕ_h Versus z/L at 304.8 m - Method 1	133
60.	ϕ_h Versus z/L at 13.5 m - Method 2	134
61.	ϕ_h Versus z/L at 59.9 m - Method 2	135
62.	ϕ_h Versus z/L at 112.8 m - Method 2	136
63.	ϕ_h Versus z/L at 185.4 m - Method 2	137
64.	ϕ_h Versus z/L at 289.1 m - Method 2	138
65.	ϕ_m Versus z/L, using $\phi_m = (1 - 15\ z/L)^{-1/4}$, $z/L < 0$ and $\phi_m = (1 - 16\ z/L)^{-1/4}$, $z/L < 0$	152

LIST OF TABLES

No.		Page
1.	Points Not Plotted on Figures 3 through 7	31
2.	Points Not Plotted on Figures 8 through 12	38
3.	Analysis of Variance for σ_u/σ_A Versus Mean Wind Velocity	58
4.	Analysis of Variance for σ_v/σ_A Versus Mean Wind Velocity	59
5.	Analysis of Variance for σ_w/σ_E Versus Mean Wind Velocity	60
6.	Analysis of Variance for σ_E Versus σ_w/U	64
7.	Analysis of Variance for σ_A Versus σ_v/U	64
8.	Average σ_w/u_* for Local u_*'s and Surface u_*'s	67
9.	Linear Regression and Variance Analysis of σ_E on ln fz/u_*	78
10.	Linear Regression and Variance Analysis of σ_A on ln fz/u_*	79
11.	Quadratic Regression and Variance Analysis of σ_E on ln fz/u_*	80
12.	Quadratic Regression and Variance Analysis of σ_A on ln fz/u_*	81
13.	Parameters Used to Calculate α_1 as Function of k	113
14.	Values of α_1	113
15.	Calculated and Observed Values of ϵ	119

ACKNOWLEDGMENTS

Sincere appreciation is expressed to Dr. Todd Crawford, who graciously provided the use of the SRL-WJBF meteorological facility during the experiment. Several Savannah River Laboratory scientists, especially Dr. M. M. Pendergast, assisted in many ways. Thanks is also due to Battelle Northwest Laboratory personnel, including Tom Horst, who provided support with several specialized instruments. Larry Rainey, Ray Hollowell and Michael Shipman did much of the original computer programming. A special thanks is due to David Delong who provided assistance and advice to the project from its inception. Appreciation is expressed to Dr. Hans A. Panofsky who provided many suggestions in the analysis of the data.

This research was supported by the Environmental Protection Agency, Meteorology Laboratory, under EPA Grant No. R-800662.

SECTION I

GLOSSARY OF TERMS, ABBREVIATIONS, AND SYMBOLS

The following is a list of symbols used in this report:

g acceleration due to gravity,

k von Karman's constant,

u', v', w' longitudinal, tranverse, and vertical components of the fluctuating part of the wind,

U magnitude of the mean vector wind,

S mean horizontal wind speed,

z vertical coordinate,

θ mean potential temperature,

θ' fluctuating part of potential temperature,

u_* friction velocity $[\tau/\rho]^{1/2}$,

L Monin-Obukhov length scale,

ρ mean density of the air,

τ surface turbulent shearing stress,

$S_w(n)$, $S_v(n)$, $S_u(n)$ vertical, transverse, and longitudinal component of the power spectral density function,

n frequency measured in Hertz,

K wave number measured in radians per meter,

α_1, α_2, α_3 Kolmogorov constants for u, v, and w components of the inertial subrange power spectral density function,

ε dissipation rate for turbulent energy,

σ_E, σ_A standard deviation of the wind elevation and azimuth angles respectively,

σ_u, σ_v, σ_w standard deviation of the u, v, and w component of the wind,

$q^2/2 \equiv (u'^2 + v'^2 + w'^2)/2$ total turbulent kinetic energy,

q_θ specific humidity,

ℓ mixing length.

Some of the results were analyzed in dimensionless form using the dimensionless quantities below, where the overbar symbol designates a time average:

$\phi_h = \frac{-kzu_*}{\overline{w'\theta'}} \frac{\partial\theta}{\partial z}$ . . . . . a dimensionless potential temperature gradient,

$\phi_\varepsilon = \frac{kz\varepsilon}{u_*^3}$ . . . . . a dimensionless dissipation of turbulent energy,

$\phi_m = \frac{kz}{u_*} \frac{\partial U}{\partial z}$ . . . . . a dimensionless wind shear,

$z/L = \frac{-kzg\,\overline{w'\theta'}}{\theta_o u_*^3}$ . . . . . a dimensionless height,

$\psi = \int_o^{z/L} [1 - \phi_m(z/L)]/(z/L)d(z/L)$ . . . correction to be subtracted from logarithmic wind profile to account for non-adiabatic conditions,

fz/u_* (where f is the Coriolis parameter) . . . a dimensionless height,

$K_h/K_m = \phi_m/\phi_h = \frac{-\overline{w'\theta'}\,\partial U/\partial z}{u_*^2\,\partial\theta/\partial z}$ . . ratio of eddy transfer coefficients, and

$f = \frac{nz}{U}$ . . . . . a dimensionless frequency.

Statistical Terms

Degrees of Freedom (D.F.) - The total degrees of freedom equals the number of independent observations. Every coefficient estimated in the regression model accounts for one degree of freedom. The number of degrees of freedom for the deviation from the regression equals the total minus the number of coefficients estimated in the regression. In the analysis of variance tables, degrees of freedom will be abbreviated D.F.

F-test - F is the ratio of two mean squares such that the expected value of the numerator under the null hypothesis is equal to the expected value of the demoninator. For all tests in this report the null hypothesis is that the particular regression coefficient(s) under the source of variation is zero. F values that are not statistically significant at the 5% level are noted by (NS). A value of F that was significant at the 5% level indicates that if the null hypothesis is true less than 1 out of 20 samples will give an F value of this magnitude.

Mean Square - The sum of squares divided by the degrees of freedom.

R^2 - The multiple regression coefficient. It is the proportion of the total variation that can be attributed or explained by the variables in the regression model. An R^2 equal to 1 implies that all of the sample observations lie on the regression equation.

Ninety-five Percent Confidence Interval - The 95% confidence interval of a regression coefficient b is determined by

$$b \pm t_{.05} \ (\sigma_b)$$

where $t_{.05}$ is found from a table of distribution of Students t with the degrees of freedom equal to the degrees of freedom of the deviations from regression. If the observations were repeated many times with the same procedures and regression, 95 percent of the intervals would include the true population value.

Regression Model - It is the model fitted by the sample data. The coefficients in the regression model are determined so that the sum of squares of the deviations of the observed values from the values predicted by the regression model is minimized. It can be shown that the regression model coefficients are the best linear unbiased estimates of the true population coefficients.

Standard Deviation of a Regression Coefficient b - This will be denoted by the symbol σ_b^2.

Sum of Squares - The total sum of squares is the sum of the observations squared. The deviations from regression sum of squares is the sum of the observed values from the values predicted in the regression equation squared. The total sum of squares equals the sum of squares due to regression plus the sum of squares of deviations.

True Population Model - The true relationship between the dependent variables and the independent variable. It is assumed for all true population models in this report that ε is normally distributed with mean 0 and variance σ^2.

SECTION II

CONCLUSIONS

Friction velocities measured by the cup anemometer and bivane systems at the SRL-WJBF tower agree reasonably well with independent measurements by a Gill - u, v, w anemometer and a sonic anemometer. The nondimensional wind shear calculated from the data varies with the stability parameter z/L in a manner that is well modeled by the Businger, Wyngaard, Izumi, Bradley (1971) expressions based on the 1968 Kansas experiment. The departure from BWIB curves seems to start above 160 meters and become progressively worse. The implication is that the simple equations predicted by similarity theory for the surface layer cannot be extended much above 160 m except as a first approximation.

Roughness lengths were found to be about 8 cm and 36 cm for the two predominate wind directions at the tower site.

Both σ_E and σ_A decreased with increasing stability. Height dependencies were characterized by a decrease in the rate of change of σ_E and σ_A with z/L as the height of measurement increased. The value of σ_E and σ_A at the lowest level seemed to be a predictor for values at higher levels. Flow over terrain characterized by larger roughness lengths, z_o, clearly increased the magnitudes of σ_E and σ_A in comparison to flow corresponding to smaller z_o. The variation of σ_E and σ_A with z, z_o, and L agree qualitatively with the nomograms prepared by Panofsky and Prasad (1965).

The approximations,

$$\sigma_w/\sigma_E \simeq U \text{ and} \qquad (2.1)$$

$$\sigma_v/\sigma_A \simeq U \,, \qquad (2.2)$$

were demonstrated to be very good under any of the conditions encountered in this experiment including "quasi-laminar" flow which occurs at night.

The mean over all samples of σ_w/u_* (using friction velocities measured near the surface) for neutral conditions ($|z/L| < 0.05$) is 1.27. This value agrees well with previously published values.

Under near neutral stability conditions, σ_E and σ_A were found to scale with fz/u_*. A quadratic regression of σ_E on ln fz/u_* accounted for 70 percent of the variation of σ_E. A linear regression of σ_A on ln fz/u_* accounted for 67 percent of the variation of σ_A with ln fz/u_*.

Average measured eddy viscosities in neutral conditions ($|z/L| < 0.05$) agree well with the values predicted by the equation:

$$K_m = u_* kz \qquad (2.3)$$

where u_* is taken from the average of the 18.3 m measured values.

The data supported the contention that the ratios of momentum and heat diffusivities, K_m/K_h approach zero for increasing stability when $z/L < 0$. The near neutral value for the ratios was less than 1.

Although there is considerable scatter in the results, the measured spectral scales of the vertical component of velocity agree with the results of Pasquill (1972).

The spectral ratios, $S_w(n)/S_u(n)$ and $S_v(n)/S_u(n)$ calculated from 18.3 m sonic anemometer data corresponding to a stability range of $-0.3 \leq z/L \leq 0.1$ were found to exhibit a distinct trend toward the 4/3 value expected in the inertial subrange.

The normalized spectra measured at 18.3 meters exhibited a systematic progression with z/L during stable conditions but were randomly clustered during unstable conditions. A region separating the stable

from unstable spectra was detected on the v spectra plot indicating an abrupt shift in the scale of turbulence. The spectral peaks and corresponding frequencies were found to be in agreement with the results of the 1968 Kansas experiment. Under stable conditions z/L was found to be an adequate scaling parameter for the spectra.

A Kolmogorov constant calculated from six sonic u spectra corresponding to near neutral stability was found to be 0.5 if a value of 0.4 was assumed for the von Karman constant.

The dissipation of turbulence energy obtained from the 18.3 m sonic spectra was found to be reasonably estimated by

$$\varepsilon = \frac{2.5}{z} u_*^3 (1 - 16\, z/L)^{-1/4}, \quad (z/L \leq 0) \quad \text{or} \tag{2.4}$$

$$\varepsilon = \frac{2.5}{z} u_*^3 (1 + 4.7\, z/L), \quad (z/L \geq 0). \tag{2.5}$$

Similarity theory has proven particularly effective in describing turbulence statistics in the atmospheric surface layer and above up to 100 meters. This was found to be the case in this experiment even though the terrain was nonhomogeneous. In fact a tendency for the atmospheric turbulence statistics to be described by the relatively simple concepts of similarity theory was found at levels well above 100 meters.

SECTION III

RECOMMENDATIONS

The objective of this research program was to measure and study atmospheric turbulence statistics which are relevant to dispersion of air pollutants in the atmosphere. In order to achieve this end it was essential to demonstrate that the quality of data was good. Agreement between different instruments at the same level and concurrence between these measurements and others in the surface layer give resonable assurance that the quality of these data is good. Having extablished data quality makes it possible to have confidence in the findings, i.e. similarity theory can be extended upward beyond the usually defined surface layer over nonhomogeneous terrain. It is also possible to recommend that new investigations using these data be attempted.

New investigations should be directed toward more thoroughly establishing the effect of nonhomogeneous terrain on atmospheric turbulence statistics. Also, the data removed during the editing procedure should be studied, especially those cases demonstrating laminar flow at night. Spectra should be studied for changes with height and stability.

It is gratifying that as an approximation the relatively simple concepts of similarity theory give a reasonable description of atmospheric turbulence properties several meters above the surface layer and for nonhomogeneous fetches.

SECTION IV

INTRODUCTION

The diffusion of gaseous pollutants from tall stacks is directly related to atmospheric turbulence in the planetary boundary layer (PBL). Tall stacks are frequently used in modern fossil-fuel power generating plants and individual stacks can be 1000 ft. (304.8 m) or more in height. Several such stacks are being planned for construction in the future.

Since our knowledge of atmospheric turbulence in the PBL is relatively inadequate, it is of great importance to carry out studies of turbulence in the field and compare findings with theoretical predictions when possible. Many studies of atmospheric turbulence have been accomplished in the surface layer (i.e., the region below 100 meters) but few have examined data above 100 meters. Also, most theories specify homogeneous terrain upwind from the sensor locations. While most towers are sited in non-homogeneous terrain the ideal site for testing theory is perfectly flat and without changes in roughness. There have been few attempts to test turbulence theories for nonhomogeneous fetches and at heights above the surface layer.

Information obtained in this investigation is expected to be ultimately applicable to the design of tall stacks, in particular, to help answer questions regarding the advantage or disadvantage of a particular height of stack for various meteorological conditions.

SECTION V

APPLICATION TO DIFFUSION

Application of the results of this study is found in the Gaussian Plume Diffusion Model. In this model the concentration at a point (x, y) at ground level downwind from a source at effective stack height H is:

$$\chi\,(x,y,;\,H) = \frac{Q}{\pi\sigma_y\sigma_z U} \exp\left(-\frac{y^2}{2\sigma_y^2}\right) \exp\left(-\frac{1}{2}\,\frac{H^2}{\sigma_z^2}\right) , \qquad (5.1)$$

where

U = mean wind speed,

χ = the concentration of the gas or aerosol,

x,y = distance along-wind and cross-wind measured from the source,

H = effective stack height,

Q = source strength, and

σ_y, σ_z = horizontal and vertical standard deviations of concentration.

Cramer (1964) has shown that relationships of the form

$$\sigma_y = \sigma_A x^p \quad \text{and} \qquad (5.2)$$

$$\sigma_z = \sigma_E x^q , \qquad (5.3)$$

where σ_A and σ_E are the standard deviations of wind azimuth and elevation angle, respectively, and p and q are functions of stability, are very useful in predicting the downwind spread of a plume in various stability conditions. A knowledge of the statistical behavior of σ_A and σ_E with height and stability can possibly aid in the use of this model for tall stacks or, perhaps, lead to better models of diffusion in the future.

If one assumes that $\sigma_y = a\sigma_z$, i.e., where the vertical and horizontal cloud growths are simply proportional, then at ground level the maximum concentration is given by:

$$\chi_{max} = \frac{2Q\sigma_z}{\pi H^2 e U \sigma_y} \tag{5.4}$$

where e is the base of the natural system of logarithms. Thus from Eqs. (5.2), (5.3), and (5.4) one can see that the ratio, σ_E/σ_A, is important in determining the maximum concentration.

Because of the close relationship between atmospheric turbulence and plume dispersion it is of interest to see if theories of atmospheric turbulence such as the Monin-Obukhov similarity theory hold at levels higher than the surface layer.

SECTION VI

TOWER AND TERRAIN

The WJBF-TV -- Savannah River Laboratory Meteorological Facility, (hereafter SRL-WJBF tower) is 11 kilometers southeast of Augusta, Georgia, and 23 kilometers southwest of Aiken, South Carolina. The 366 meter tower, whose base stands 121 meters above mean sea level (MSL), has been in use as a meteorological tower since October, 1965. It was then that Savannah River Laboratory (SRL) began its data collection program for reactor safety studies. The instrumentation and several features of the SRL program were summarized in Cooper and Rusche (1968). The instruments are mounted on heavy booms extending about 3 meters outward (direction 225°) from the tower.

In 1973, changes to the system were made to improve the quality of the data. The details of the system's renovations are contained in Crawford (1974). The most significant improvement was the addition of a digital data acquisition system (DAS). The system monitors and records information from 32 channels of data directly on magnetic tape in a format compatible with SRL's IBM 360/195 computer facility.

The WJBF tower is one of three TV towers near the rural community of Beach Island, South Carolina. There is no one dominant form of land use in the immediate vicinity of the tower. Along any given azimuth from the tower, the rolling terrain varies with pine tree forests (average height approximately 12 meters), pastures and fields, and clearings of waist-high scrub and young saplings.

Two major topographical features are the Savannah River and an intermittent stream called Long Branch. The broad Savannah River flows within 5.6 kilometers to the west and within 9.7 kilometers to the

south of the instrumented tower. Long Branch slopes from northwest to southeast and its closest approach to the tower is about 610 meters to the southwest (see Figure 1).

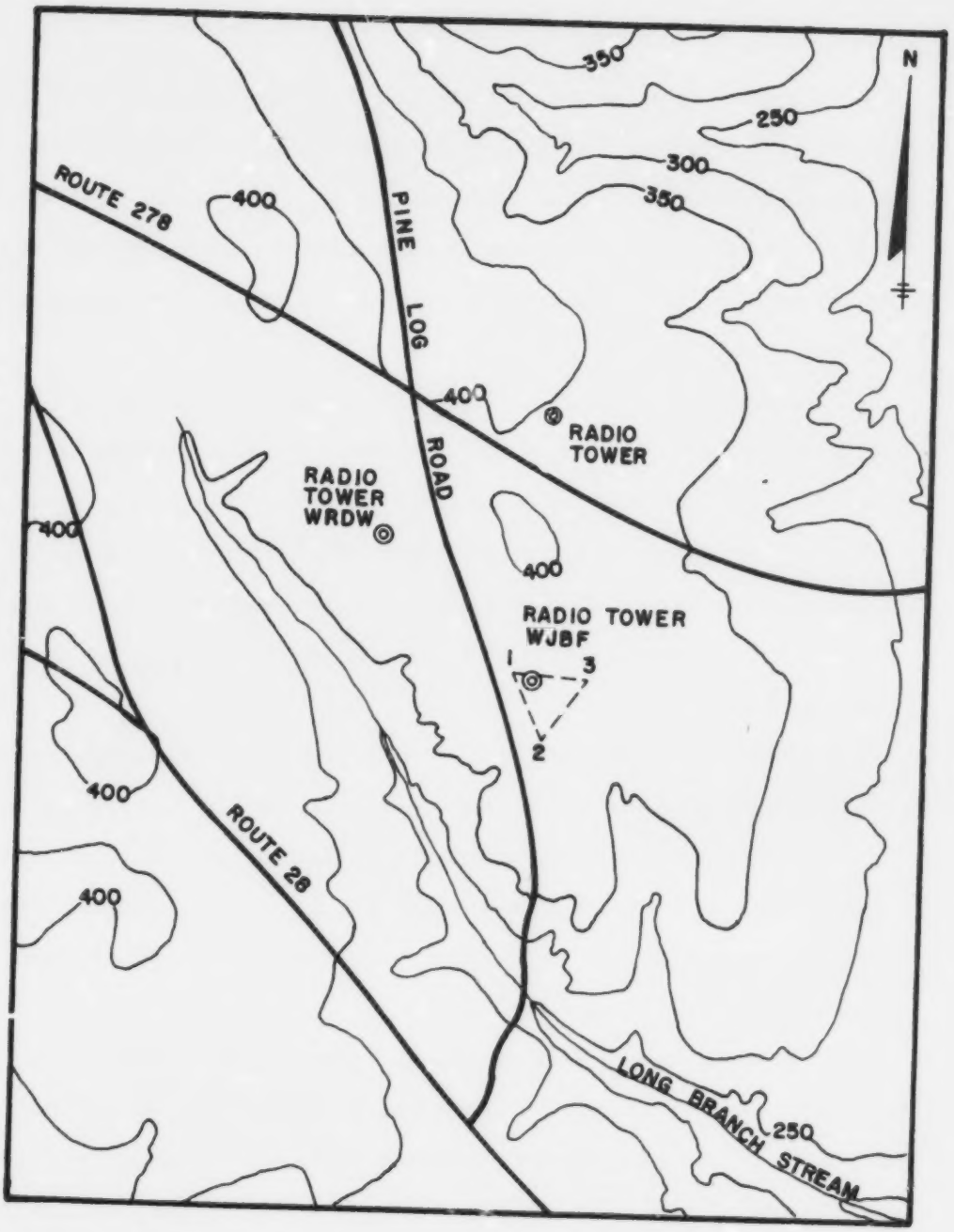

Figure 1. Terrain at SRL-WJBF tower. Dashed equilateral triangle shows location and orientation of pibal observation sites with 304.8 meter baselines. Scale is 2 5/8 inches equals one mile. Contours are for every 50 feet.

SECTION VII

INSTRUMENTS

The temperature sensors used to calculate mean temperature at the six tower levels were (100 ohm) platinum resistance wire thermometers. These thermometers were wind aspirated except at the lowest level which was mechanically aspirated. The response time of the thermometers is on the order of several seconds and they are of no value in measuring turbulent heat flux.

A thermistor attached to a Gill u-v-w anemometer was supplied by Battelle Northwest to measure the heat flux. The fast response thermistor was found (by Battelle) to have a time constant of less than or equal to 0.12 sec (depending on wind speed). This instrument configuration has been used to compute turbulent heat flux on previous occasions by Battelle Northwest with results that compared favorably with simultaneous measurements by the sonic anemometer.

Comparisons between the Gill u-v-w anemometer and the sonic anemometer for measuring stresses are documented in Horst (1973). The instruments seem to agree well for measured turbulence spectra for wavelengths longer than 25 meters (0.2 Hertz at wind speed 5 mps). A correction was applied to the wind measurements of the Gill anemometer to account for cosine response as suggested in Horst (1973).

The wind measuring instruments are Climet cup and bivane systems. The distance constant of the cup anemometers is on the order of 1 m. Averaging circuits for the photo-chopper reduce the frequency response (-3 db point for sine wave input) to about 0.1 Hertz. The characteristics of the bivanes were measured by Brookhaven National Laboratory and found to have a damping ratio of 0.55 and a delay distance of 0.9 m.

Both the sonic anemometer and the Gill anemometer give best results when the mean wind direction is into the open end of the sensor arrays. The sonic anemometer is somewhat more critical in this respect than is the Gill instrument. Light and variable winds are thus a problem in that gusts reach the sensors from unfavorable directions. Constant monitoring of wind direction was necessary during the experiment so that when large excursions of azimuth angle did occur data collection could be interrupted.

SECTION VIII

EXPERIMENT

Climet cup and bivane systems were mounted and leveled with respect to gravity at six levels on the tower (18.3, 91.4, 137.2, 182.9, 243.8, and 304.8 meters). (Refer to Appendix A for further details). Slow response aspirated temperature sensors (platinum resistance wire thermometers) were located at 3.0, 36.6, 91.4, 137.2, 182.8, 335.3 meters. (For further details on instrumentation refer to Cooper and Rusche, 1968, and Crawford, 1974.) Battelle-Northwest maintained and operated three instruments which were attached to two aluminum booms mounted at about 18.3 meters. Included were a Gill u-v-w propeller anemometer with a fast response thermistor (refer to Appendix B for further details) mounted on its vertical arm, and a sonic anemometer.

During the sixteen day period between 13 May and 29 May, 1973, the instruments on the SRL-WJBF tower recorded data unless conditions indicated rain, fog, or other disturbing influences. Also, to further examine the planetary boundary layer, pibal measurements of the wind were taken using double theodolite techniques.

SECTION IX

DATA PROCESSING

To monitor simultaneously all instruments on the tower required 31 of the available 32 channels of the DAS. The DAS had the capability of scanning all 31 channels at several pre-set rates; however, during this experiment either a five or a ten scans-per-second mode was selected. Preceding each scan, information as to the year, day, hour, minute, and second was recorded on the tape. The data on tape were compacted and calibrated at SRL's computer facility and then sent to North Carolina State University for processing at the Triangle Universities Computation Center (TUCC).

Wind velocity measurements were referred to a natural coordinate system, i.e., the x axis was oriented along the mean wind vector, the y axis was oriented perpendicular to the x axis and in the horizontal plane, the z axis was oriented perpendicular to the x and y axes so as to form a right-hand coordinate system. It is important to note that in the natural coordinate system used the mean wind vector did not necessarily lie in the horizontal plane and that at each level of the tower the wind components u, v, and w refer to the natural coordinate system appropriate to that level and 40-minute time period.

The data were time averaged over 40-minute periods. Averages and variances of the turbulence parameters of interest were edited and then analyzed. Out of a total of 239 blocks of data, 119 were retained after editing for further analysis.

The data were edited as follows: (1) data blocks were removed if a particular block did not contain a full 40 minutes of data; (2) 40-minute blocks were removed if an upward transport of momentum was

evidenced, i.e., $-\overline{u'w'} < 0$, because similarity theory does not model such situations; (3) blocks were rejected during conditions where the variance of the vertical velocity fell below 0.01 m^2/sec^2 (during very stable conditions the vertical velocity fluctuations are heavily suppressed leading to a kind of laminar flow); and (5) blocks were rejected during the transition period at sunrise when the rapid surface heating and resultant momentum and heat flux progressively affects higher levels in the PBL. The Monin-Obukhov length scale, L, for such transition conditions computed at the 18.3 meter level, indicated dynamic instability when in fact higher levels of the tower still reflected nighttime conditions, i.e., low vertical velocity variances, positive potential temperature lapse rates and large vertical wind shears; thus the 18.3 meter L value did not characterize the entire region between the ground and the top of the tower. Details of the data block editing procedure are given in Appendix C.

Both the mean wind speed, S, and the magnitude of the mean wind vector, U, were calculated for each 40-minute block. The value of S is always greater than U and this difference can be significant.

The turbulent shear stress was calculated using the expression

$$\tau = \rho \left(\overline{v'w'}^2 + \overline{u'w'}^2\right)^{1/2} = \rho u_*^2. \qquad (9.1)$$

The value of (τ/ρ) at 18.3 meters was assumed to be the surface friction velocity. The term $|\overline{v'w'}|$ was included in the calculation, since it was greater in magnitude than 10 percent of $|\overline{u'w'}|$ values in 59 to 75 percent of the cases (depending upon the level of measurement).

The Monin-Obukhov length scale,

$$L = \frac{-u_*^3}{k \frac{g}{\theta_o} \overline{w'\theta'}}, \qquad (9.2)$$

was calculated using a friction velocity from the Gill u-v-w anemometer mounted at 18.3 meters. Von Karman's constant, k, was assumed to have the value 0.35. The parameter θ_o was obtained from the 3 meter level. The temperature flux, $\overline{w'\theta'}$, was calculated from the Gill u-v-w anemometer and the fast response thermistor at 18.3 meters.

Atmospheric turbulence spectra were calculated using the Fast Fourier Transform (FFT) technique designed by Singleton (1969). Wind speed and direction were converted to components in a Cartesian coordinate system where the x-axis was the direction of the mean wind vector, the y-axis was perpendicular to the mean wind vector and in the horizontal plane, and the z-axis was oriented to form a right handed system. It should be noted that the z-axis was not always oriented along a plumb line. The use of this coordinate system was recommended by Kaimal and Touart (1967). The time series composed of fluctuating velocity components were then multiplied by a cosine taper data window. This resulted in a cosine taper over the beginning and ending 10 percent of the 40-minute time series. The FFT was then applied to the tapered data resulting in a raw spectrum. Squaring and adding the Fourier transformed coefficients resulted in a raw power spectrum estimate. Autocorrelation values were then obtained by applying an inverse FFT. A Parzen lag window was applied to the autocorrelation values followed by another application of the FFT. This was done in order to obtain smoothed power spectral density estimates. These values were then multiplied by 1/0.875 to correct for the effect of the cosine taper data window (Bendat and Piersol, 1971). The standardized frequency bandwidth corresponding to the Parzen lag window (1.86 Hertz) was converted to nondimensional frequency bandwidths with the expression

$$B = \frac{1.86z}{\Delta t(\text{lags})U} \quad . \tag{9.3}$$

When the sonic anemometer was in operation the sampling rate was 10 times per second. The resulting 24,000 data points for each 40-minute sampling period were then reduced to 8,000 data points by 3-point block averaging. In effect, this changed the sampling interval from 0.1 sec. to 0.3 sec. for all data taken while the sonic anemometer was in operation.

SECTION X

SURFACE FRICTION VELOCITY

The instruments nearest to the surface were at a height of 18.3 meters. The data derived from those instruments were used in computing surface friction velocities. Computed friction velocity from the cup and bivane system and the Gill anemometer differed slightly. One can ask if the difference is due only to random error or if there is a real statistical difference in the two measurements. The sonic anemometer also was capable of measuring friction velocity. However, because of difficulties with the sonic anemometer mentioned in Section VII and the fact that the sonic was only present for about one half of the experimental period, this section is limited to a discussion of the differences in friction velocity between the cup and bivane system and the Gill anemometer. A plot of u_* calculated from measurements by the Gill anemometer versus u_* calculated from measurements by the cup and bivane system is shown in Figure 2. Assuming that the true relationship is:

$$u_{*bivane} = \alpha_1 + \beta_1 u_{*Gill} + \varepsilon \qquad (10.1)$$

(where ε is a random error term and is assumed to be normally distributed with mean 0 and variance σ^2), a straight line was fit by the method of least squares to the data yielding the following equation:

$$u_{*bivane} = 0.0188 + 0.8581\ u_{*Gill}, \qquad (10.2)$$

with an estimate of σ^2 equal to 6.06×10^{-4}. One can be 95% sure that the true population constant α_1 and the true population slope β_1 are contained in the following intervals:

$$0.00514 \leq \alpha_1 \leq 0.0325\ , \qquad (10.3)$$

$$.833 \leq \beta_1 \leq .883\ . \qquad (10.4)$$

Reproduced from
best available copy.

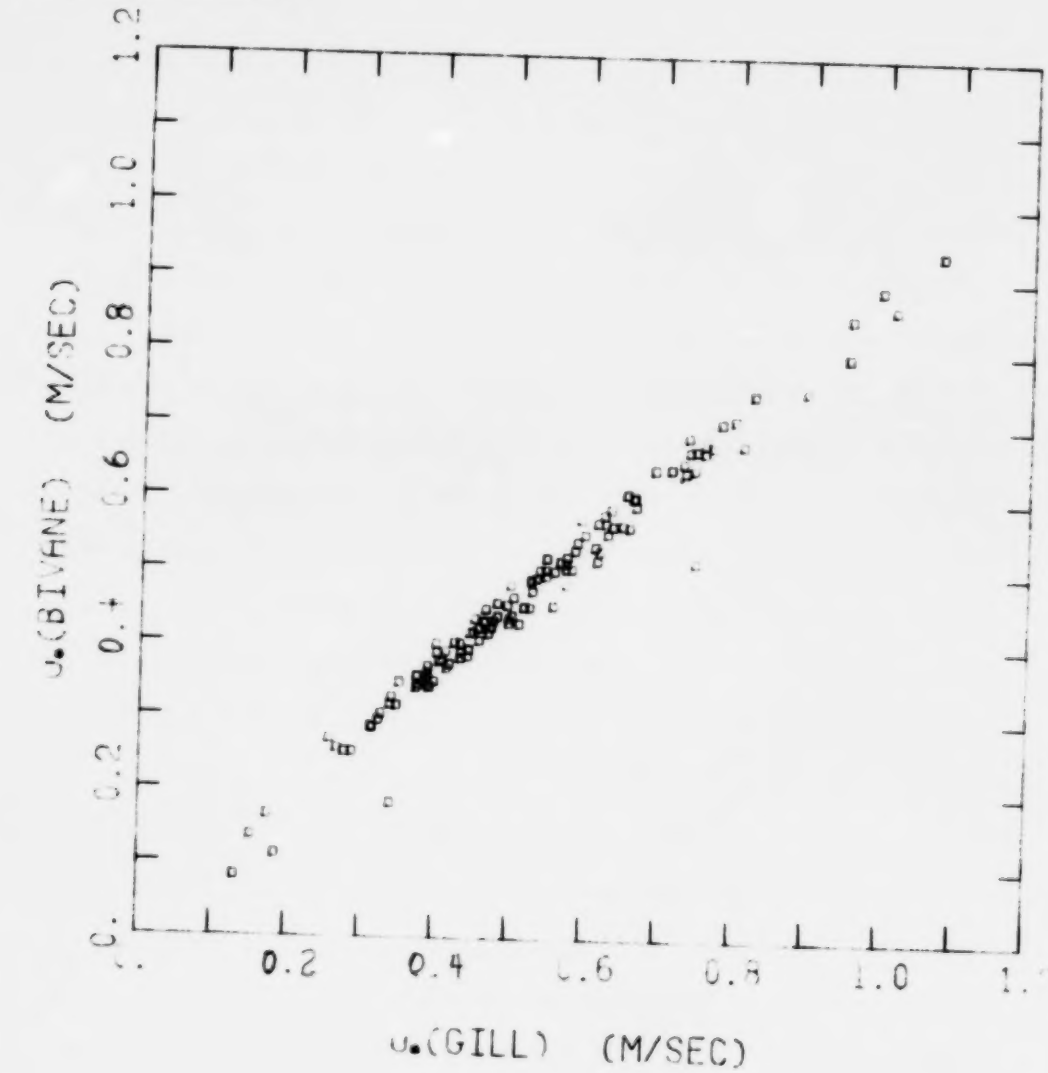

Figure 2. Comparison of friction velocity, u_*, measured by the bivane and cup anemometer at 18.3 meters versus u_* measured by the Gill propellor anemometer at the same height.

From the confidence intervals one can see that α_1 is small but not equal to zero and β_1 is close to but not equal to one as it would be if the true model were of the form:

$$u_{*bivane} = u_{*Gill} + \varepsilon, \tag{10.5}$$

where the friction velocities calculated from both systems differed by only random error. Thus, the sample results indicate a real statistical difference between the two calculated friction velocities. Eq. (10.1) assumes u_{*Gill} as the independent variable (or correct variable) and indicates the predicted friction velocity for the cup and bivane system. However, it is possible to reverse the dependent and independent variables and fit a straight line of the form

$$u_{*Gill} = \alpha_2 + \beta_2 u_{*bivane} + \varepsilon. \tag{10.6}$$

Doing this the regression equation fit is

$$u_{*Gill} = -.00891 + 1.1376\, u_{*bivane}, \tag{10.7}$$

with 95% confidence intervals about α_2 and β_2 of

$$-.0251 \leq \alpha_2 \leq .00724, \text{ and} \tag{10.8}$$

$$1.1051 \leq \beta_2 \leq 1.1701, \tag{10.9}$$

and an estimate of σ^2 of 8.04×10^{-4}.

Because cups have more inertia than the Gill propellers, the Gill instrument was expected to be more responsive and this seems to be reflected in the fact that friction velocities calculated by the Gill anemometer were higher than the bivane values.

SECTION XI

NONDIMENSIONAL WIND SHEAR, ϕ_m

A cornerstone of Monin-Obukhov similarity theory is that given steady conditions and homogeneous terrain, nondimensional wind shear, ϕ_m, is a function of z/L for the surface layer. Results by Businger et al. (1971), show that

$$\phi_m = \frac{kz}{u_*}\frac{\partial U}{\partial z} = (1 - 16\ z/L)^{-1/4}\ ,\ z/L < 0 \quad \text{and} \tag{11.1}$$

$$\phi_m = (1 + 4.7\ z/L),\quad z/L \geq 0 \tag{11.2}$$

(see Appendix E) in the surface layer.

Measurements in this experiment were mostly outside the surface layer and representative of rather nonhomogeneous fetches. Nevertheless plots of ϕ_m vs z/L were made with varying degrees of "success", the lower 3 levels being better than the upper 3 levels of the tower. Two methods of computing ϕ_m were used as described below. In all cases u_* is computed from the 18.3 meter Gill u-v-w anemometer according to the formula:

$$u_* = [(\overline{u'w'})^2 + (\overline{v'w'})^2]^{1/4}\ . \tag{11.3}$$

A series of graphs is presented for which z/L is the abscissa, ϕ_m is the ordinate and each separate plot refers to a different reference level in the calculation of ϕ_m. Each plot contains solid lines which represent the empirical expressions obtained by Businger et al. (1971), hereafter referred to as the BWIB lines (see Appendix E),

$$\phi_m = (1 - 16\ z/L)^{-1/4}\ ,\ z/L < 0 \tag{11.4}$$

$$\phi_m = (1 + 4.7\ z/L)\ ,\ z/L \geq 0, \tag{11.5}$$

and the KEYPS equation (lower line on the unstable side),

$$\phi_m^4 - (18\ z/L)\ \phi_m^3 = 1 \quad \text{(Lumley and Panofsky, 1964)}. \tag{11.6}$$

Method 1. The expression for ϕ_m was approximated by

$$\phi_m = \frac{k\bar{z}}{u_*} \frac{\Delta U}{\Delta z}, \quad \text{where } \bar{z} = \Delta z/(\ln z_2/z_1). \tag{11.7}$$

The variable, $\bar{z}$, represents the appropriate reference level between z_2 and z_1 for ϕ_m. The value of $\bar{z}$ lies between the arithmetic and geometric means. Stearns (1970) used a similar expression.

The difference in mean wind, ΔU, was obtained from values of U corresponding to the 6 levels on the tower equipped with cup and bivane systems and referenced to 5 intermediate levels represented by the $\bar{z}$ given above. No correction was made for overspeeding of the cup anemometers.

The resulting plots (Figures 3 through 7) indicate that ϕ_m is reasonably modeled by similarity theory throughout the height of the tower. Scatter is small at the lower levels and increases with height.

At the 273.2 m level (Figure 7) there is a tendency for the points to fall below or to the right of the line on the stable side and above both lines on the unstable side. This indicates some departure from similarity theory at higher levels of the tower, particularly above 212 m; however the fit was fairly good at the lower levels (Figures 3 through 5). On the 45.4 m plot (Figure 3) the ϕ_m's on the unstable side can be seen to decrease more rapidly near neutral than either the KEYPS or the BWIB expressions predict. A number of points were not plotted because they fell outside the boundaries of the plots (see Table 1).

Method 2. The technique used by Businger et al. (1971) was followed in producing the next set of plots. In order to more precisely duplicate the method used by Businger, mean wind speeds, S, were used in place of magnitudes of the mean vector wind. A quadratic least squares second

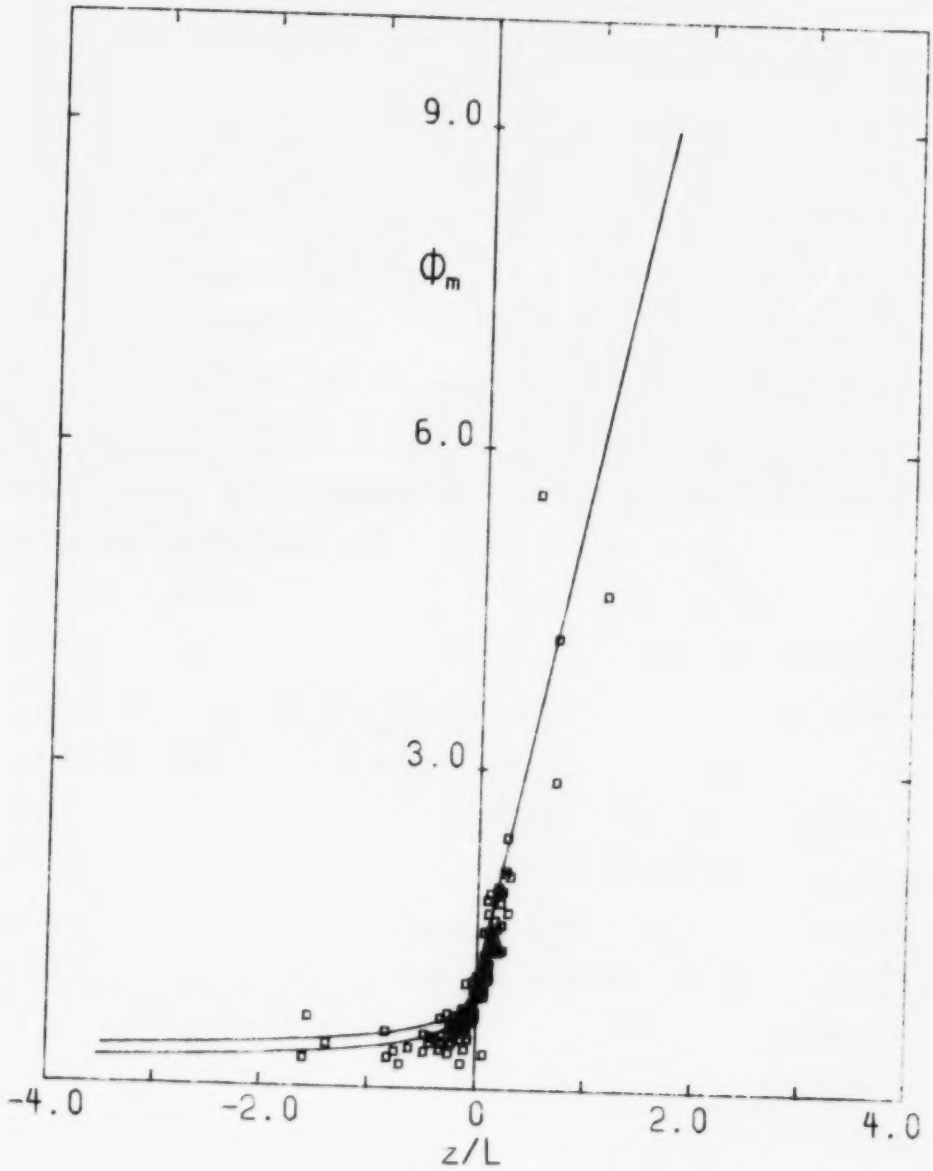

Figure 3. Nondimensional wind shear versus z/L using $\bar{z} = \Delta z/(\ln z_2/z_1)$, Method 1. A total of 119 points are plotted for $\bar{z}$ = 45.4 m. Solid lines represent the BWIB equations and the KEYPS equation (lower solid line for z/L < 0).

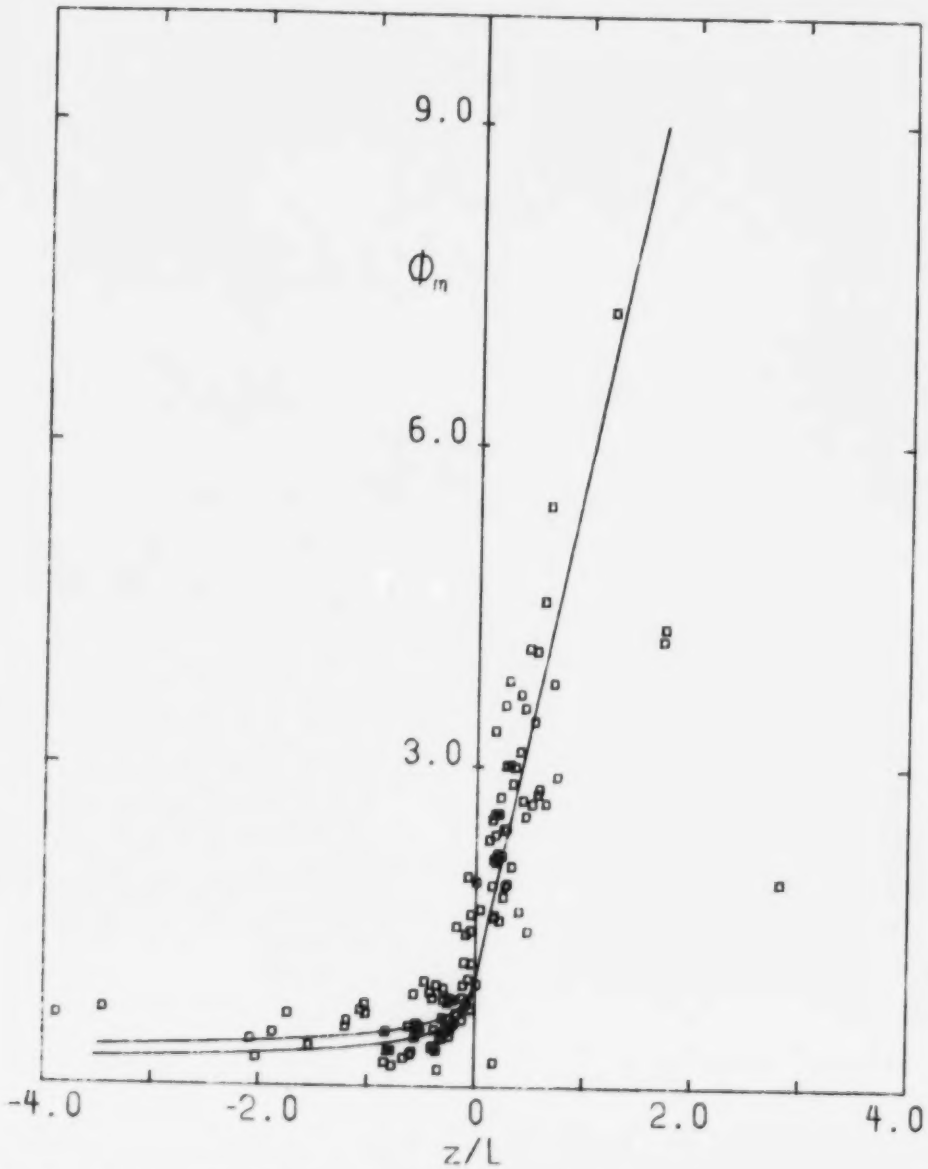

Figure 4. Nondimensional wind shear versus z/L using $\bar{z} = \Delta z/(\ln z_2/z_1)$, Method 1. A total of 114 points are plotted for $\bar{z}$ = 113.0 m. Solid lines represent the BWIB equations and the KEYPS equation (lower solid line for z/L < 0).

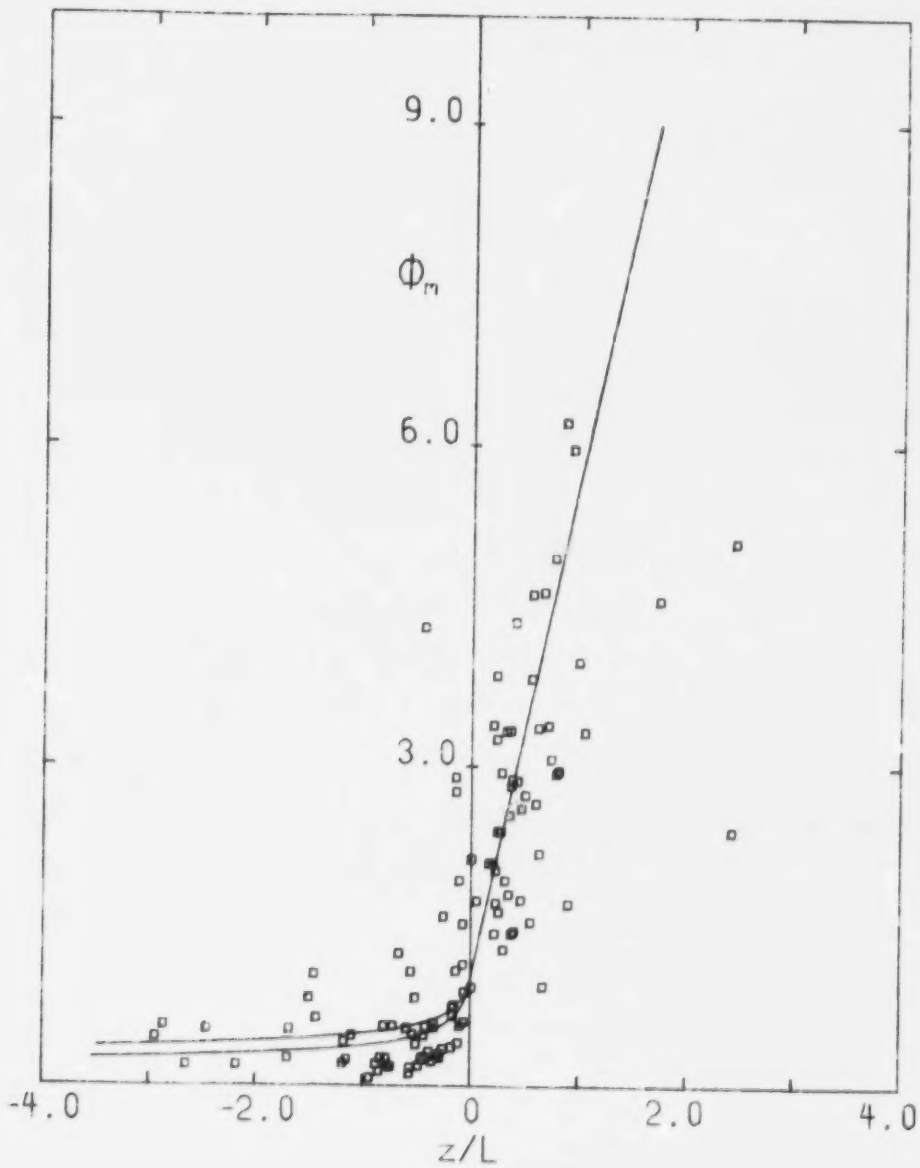

Figure 5. Nondimensional wind shear versus z/L using $\bar{z} = \Delta z/(\ln z_2/z_1)$, Method 1. A total of 112 points are plotted for $\bar{z}$ = 158.9 m. Solid lines represent the BWIB equations and the KEYPS equation (lower solid line for z/L < 0).

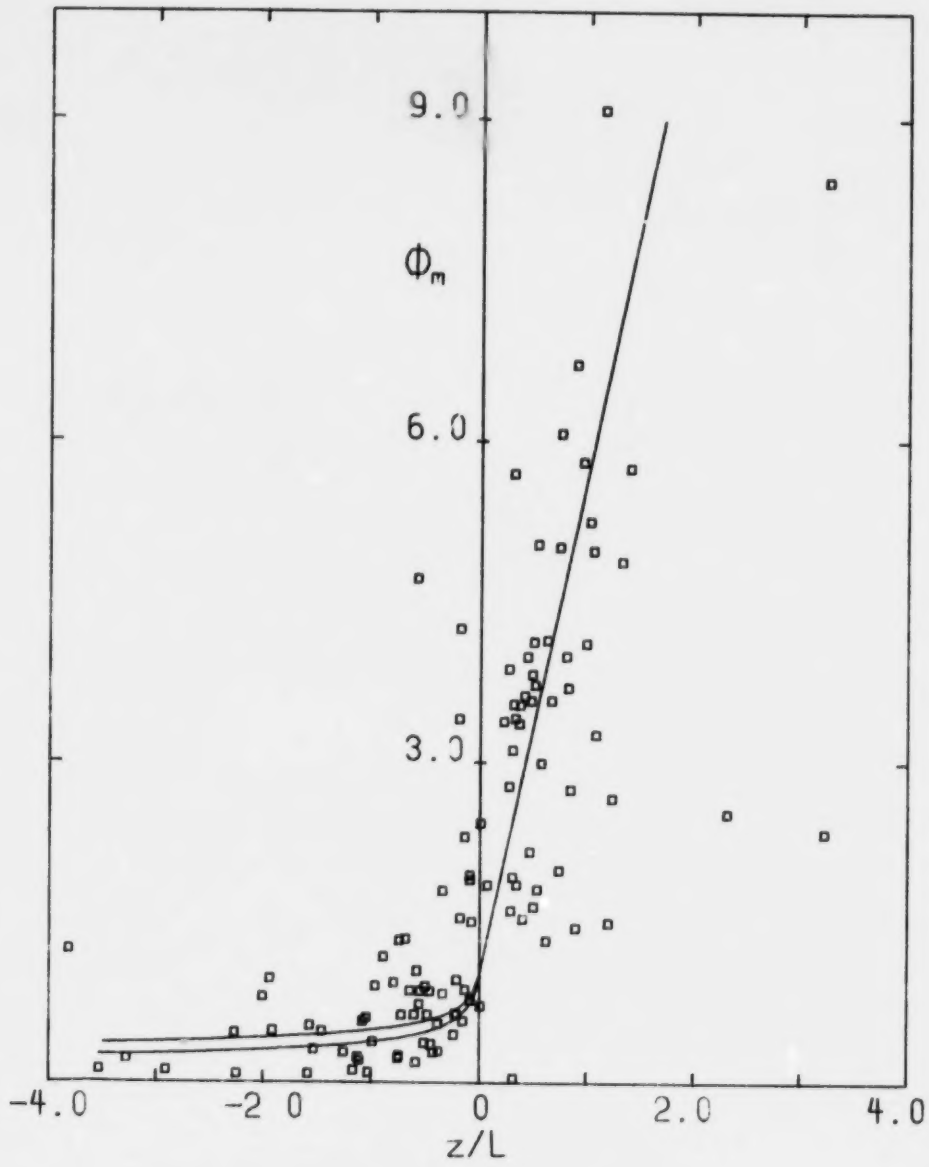

Figure 6. Nondimensional wind shear versus z/L using $\bar{z} = \Delta z/(\ln z_2/z_1)$, Method 1. A total of 112 points are plotted for $\bar{z} = 211.8$ m. Solid lines represent the BWIB equations and the KEYPS equation (lower solid line for $z/L < 0$).

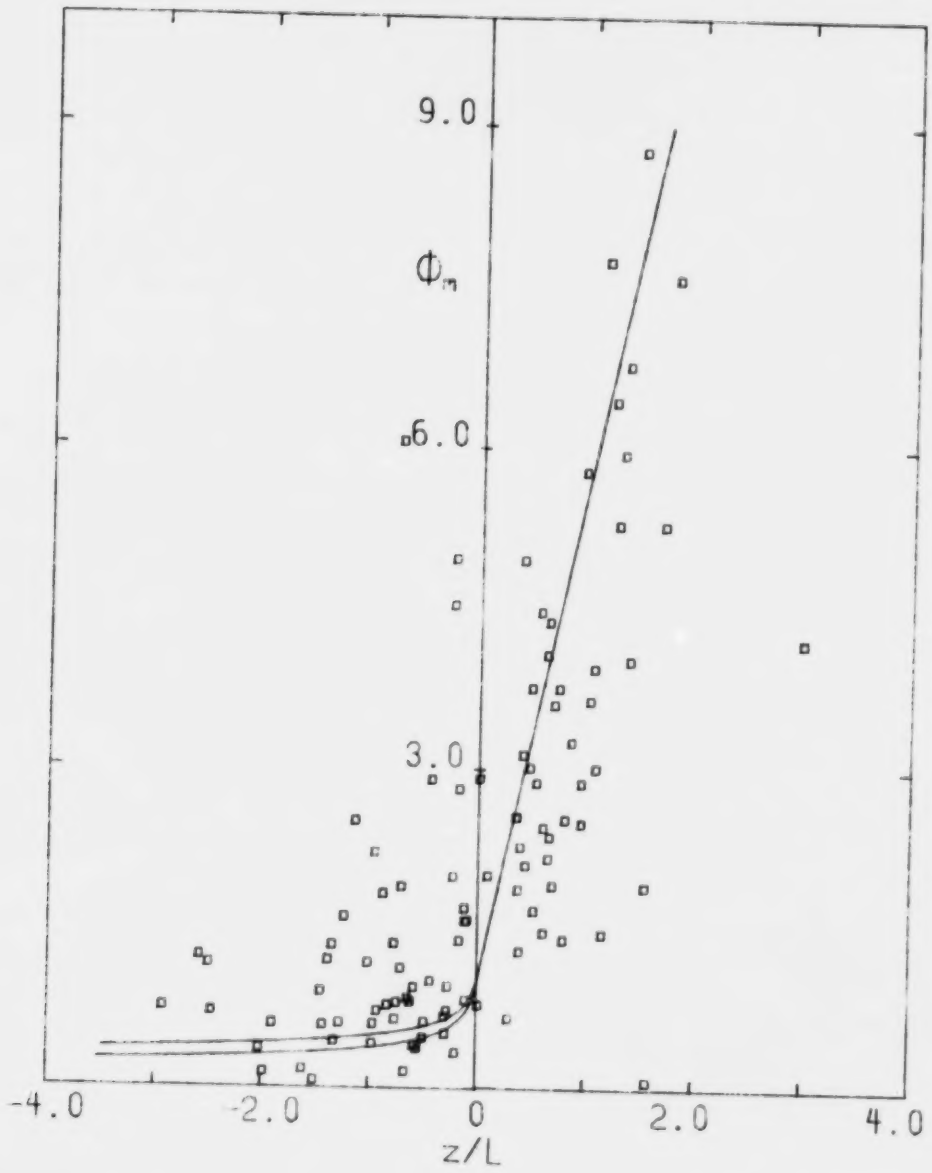

Figure 7. Nondimensional wind shear versus z/L using $\bar{z} = \Delta z/(\ln z_2/z_1)$, Method 1. A total of 102 points are plotted for $\bar{z} = 273.2$ m. Solid lines represent the BWIB equations and the KEYPS equation (lower solid line for $z/L < 0$).

Table 1. CALCULATED NONDIMENSIONAL WIND SHEARS WHICH WERE NOT PLOTTED ON FIGURES 3 THROUGH 7. COMMENTS REFER TO THE LAYER IN WHICH ϕ_m WAS CALCULATED.

Level	Comments
113.0	Fit the trend in the data.
113.0	Fit the trend in the data.
113.0	Large positive wind shear.
113.0	Large positive wind shear.
113.0	Large positive wind shear.
158.9	Negative wind shear.
158.9	Fit the trend in the data.
158.9	Negative wind shear.
158.9	Negative wind shear.
158.9	Negative wind shear.
158.9	Fit the trend in the data.
158.9	Fit the trend in the data.
211.8	Small positive wind shear.
211.8	Fit the trend in the data.
211.8	Negative wind shear.
211.8	Fit the trend in the data.
211.8	Negative wind shear.
211.8	Fit the trend in the data.
211.8	Fit the trend in the data.
273.2	Negative wind shear.
273.2	Negative wind shear.
273.2	Negative wind shear.
273.2	Fit the trend in the data
273.2	Negative wind shear.
273.2	Negative wind shear.
273.2	Fit the trend in the data.
273.2	Fit the trend in the data.
273.2	Fit the trend in the data.
273.2	Negative wind shear.
273.2	Negative wind shear.
273.2	Fit the trend in the data.
273.2	Fit the trend in the data.
273.2	Large change in wind direction.
273.2	Large change in wind direction.
273.2	Negative wind shear.
273.2	Large change in wind direction.

order polynomial regression of the form $S = A(\ln z)^2 + B \ln z + C$ was fitted to the mean cup speeds using the 6 tower measurement heights of 18.3, 91.4, 137.2, 182.3, 243.8 and 304.8 meters. This was done for each 40-minute time block yielding 119 regression equations for the wind profiles corresponding to each time block. Each regression equation was then differentiated with respect to ln z yielding 119 expressions for dS/d (ln z). Numerical values for dS/d (ln z) were then obtained for each time block and tower level. These were reduced 10 percent to compensate for overspeeding of the cups. The dimensionless shear was calculated for each level and time using the expression

$$\phi_m = \frac{k}{u_*} \frac{dS}{d(\ln z)} = \frac{k}{u_*} (2A \ln z + B). \qquad (11.8)$$

Plots of ϕ_m versus z/L were produced for five intermediate levels using this technique (Figures 8 through 12). These plots are very similar in appearance to those produced by Method 1 but with a small reduction in the amount of scatter. As with the previous method the scatter increases with height. A number of points were not plotted because they fell outside the boundaries of the plot (see Table 2).

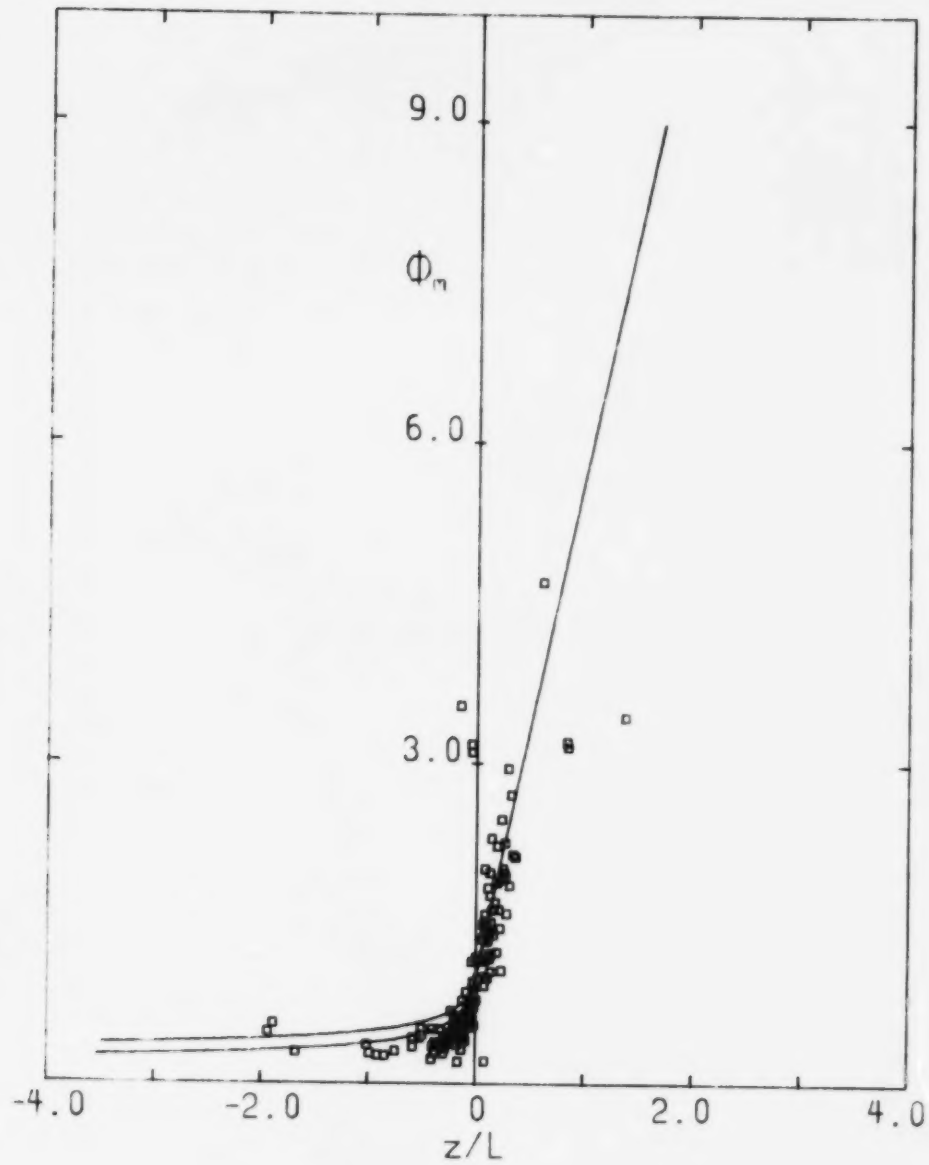

Figure 8. Nondimensional wind shear versus z/L using Businger's method (Method 2). A total of 119 points are plotted for the 54.9 m level. Solid lines represent the BWIB equations and the KEYPS equation (lower solid line for $z/L < 0$).

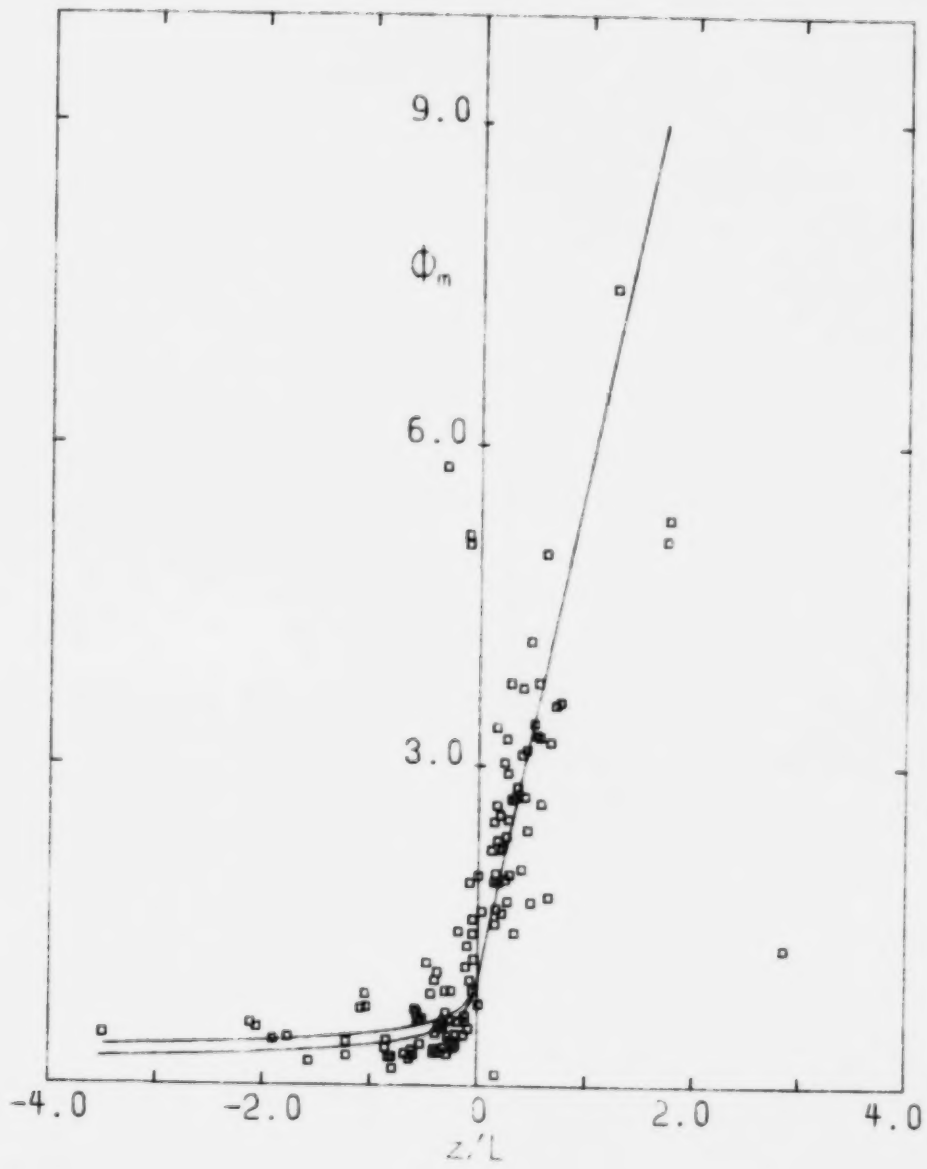

Figure 9. Nondimensional wind shear versus z/L using Businger's method (Method 2). A total of 118 points are plotted for the 114.3 m level. Solid lines represent the BWIB equations and the KEYPS equation (lower solid line for $z/L < 0$).

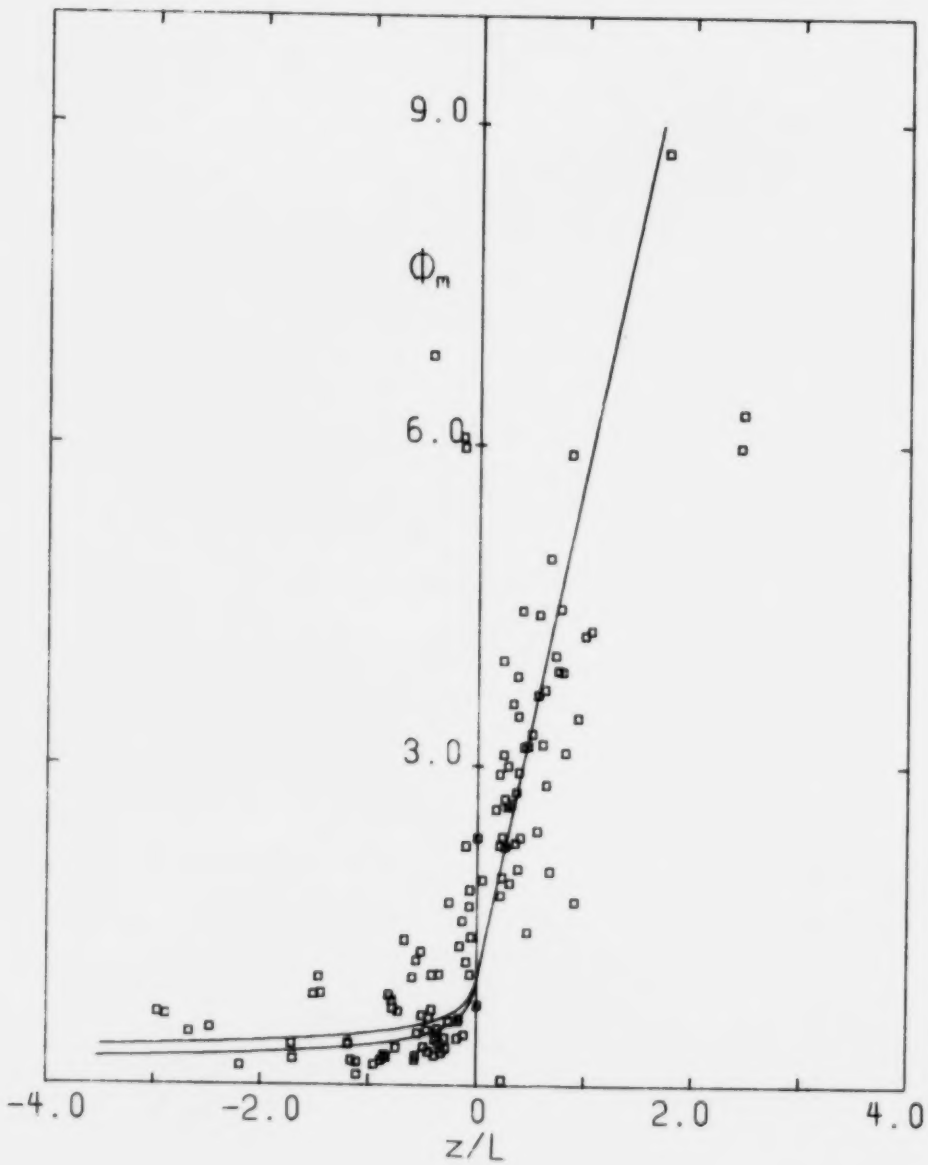

Figure 10. Nondimensional wind shear versus z/L using Businger's method (Method 2). A total of 116 points are plotted for the 160.1 m level. Solid lines represent the BWIB equations and the KEYPS equation (lower solid line for $z/L < 0$).

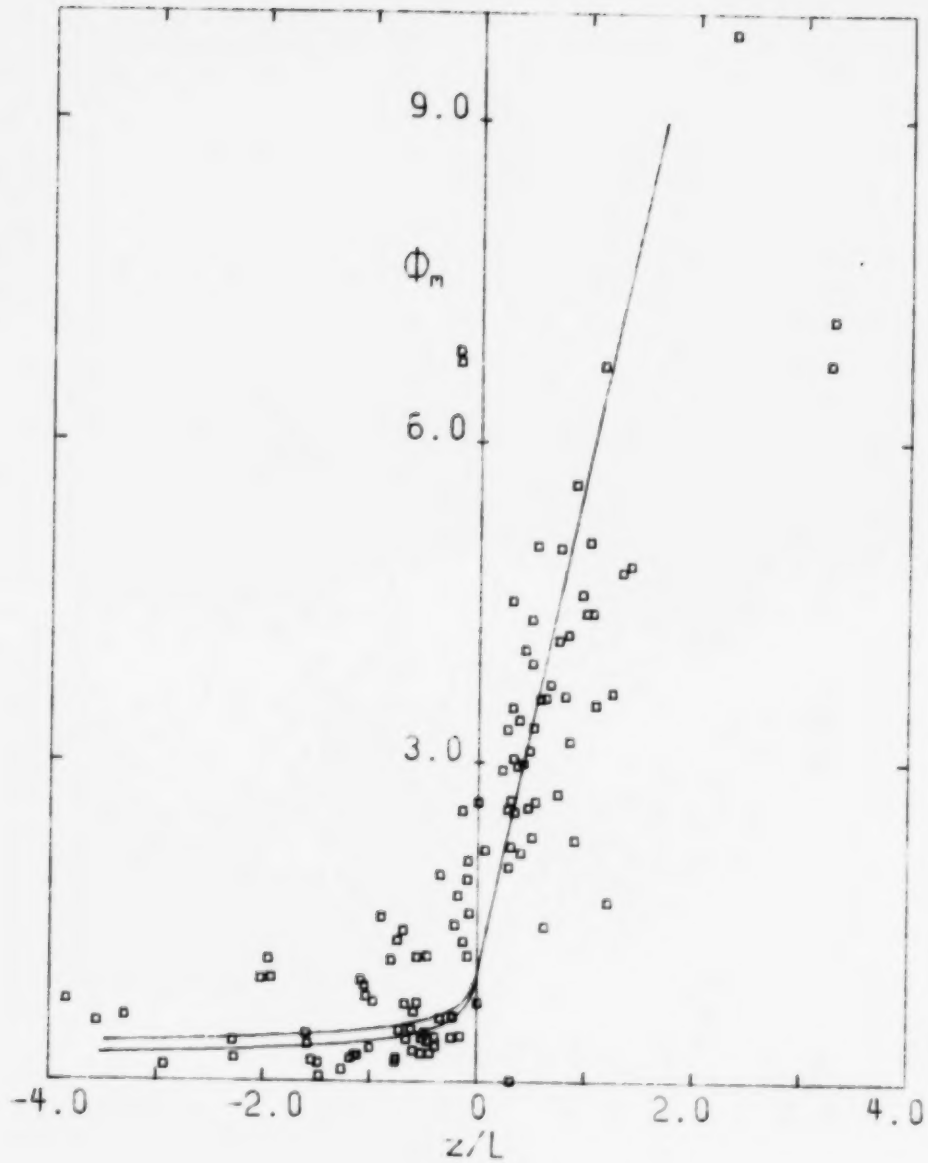

Figure 11. Nondimensional wind shear versus z/L using Businger's method (Method 2). A total of 115 points are plotted for the 213.4 m level. Solid lines represent the BWIB equations and the KEYPS equation (lower solid line for $z/L < 0$).

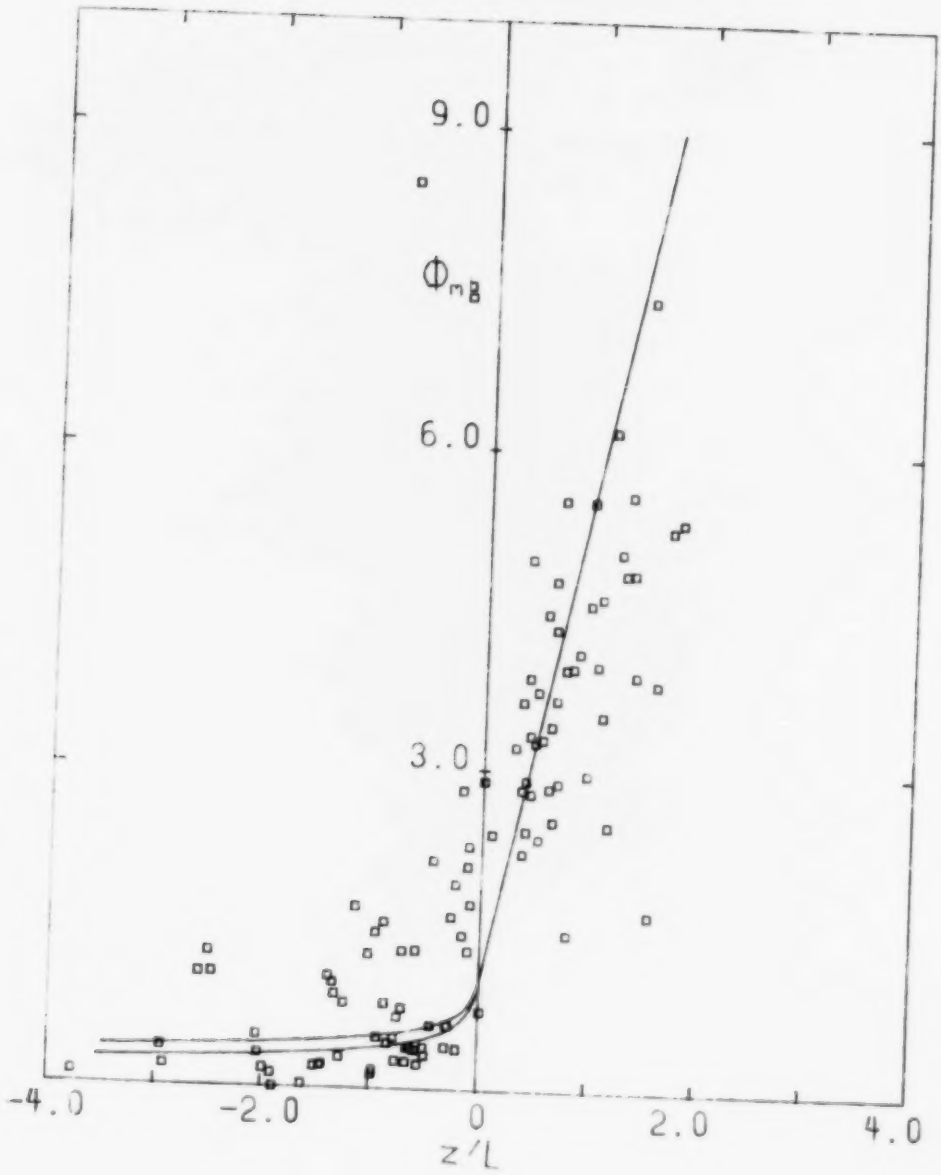

Figure 12. Nondimensional wind shear versus z/L using Businger's method (Method 2). A total of 107 points are plotted for the 274.3 m level. Solid lines represent the BWIB equations and the KEYPS equation (lower solid line for $z/L < 0$).

Table 2. CALCULATED NONDIMENSIONAL WIND SHEARS WHICH WERE NOT PLOTTED ON FIGURES 8 THROUGH 12. COMMENTS REFER TO THE LAYER IN WHICH ϕ_m WAS CALCULATED.

Level	Comments
114.3	Fit the trend in the data.
160.1	Fit the trend in the data.
160.1	Fit the trend in the data.
160.1	Fit the trend in the data.
213.4	Did not fit trend in the data.
213.4	Fit the trend in the data.
213.4	Fit the trend in the data.
213.4	Fit the trend in the data.
274.3	Did not fit trend in the data.
274.3	Fit the trend in the data.
274.3	Did not fit the trend in the data.
274.3	Fit the trend in the data.
274.3	Fit the trend in the data.
274.3	Fit the trend in the data.
274.3	Fit the trend in the data.
274.3	Fit the trend in the data.
274.3	Fit the trend in the data.
274.3	Did not fit the trend in the data.
274.3	Did not fit the trend in the data.
274.3	Fit trend - large positive wind shears.

SECTION XII

ϕ_m vs z/L FOR NEAR NEUTRAL STABILITIES ($-0.1 < z/L < 0.1$)

It is generally assumed that if the appropriate conditions for similarity theory are met, the intercept of ϕ_m at $z/L = 0$ should equal one. Based upon this assumption, values for von Karman's constant have been determined by choosing a value that would force ϕ_m to one at $z/L = 0$. An expanded view of those points corresponding to near neutral z/L values is presented in the next series of plots so that a visual assessment can be made of what the intercept may be. The plots have two scales labeled according to the value of von Karman's constant that is assumed (i.e., 0.35 or 0.4). The solid line on all plots represents the BWIB line.

Plotting the ϕ_m's calculated using Method 1 against z/L resulted in relatively small scatter at low levels for near neutral stability (Figure 13). At the lowest level (45.5 m) the points fall below the BWIB line indicating a k near 0.43. The points are very nearly parallel in trend to the BWIB line. At the higher levels, few points fall in the near neutral range but those points plotted have a higher center of gravity than those referenced to lower levels.

The near neutral plot of points (Figure 14) calculated using Method 2 referenced to the lowest level are below but nearly parallel to the BWIB line. The position of the points seems to support a $k = 0.4$. The center of gravity of the points moves progressively upward as the reference level increases.

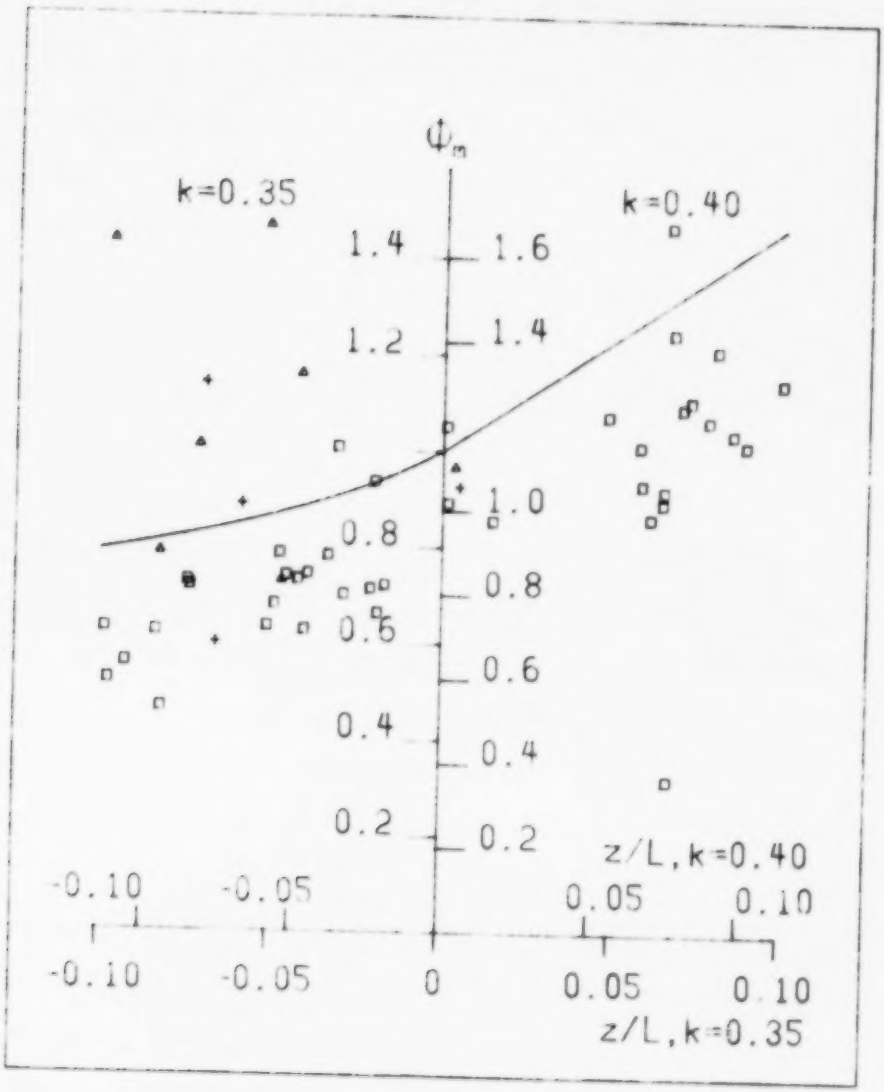

Figure 13. Nondimensional wind shear Ψ_m versus z/L using Method 1. Reference levels are 45.4 m (squares), 113 m (triangles), and 158.9 m (crosses). The solid line is the BWIB line. Upper and right side scales are for k = 0.40 whereas lower and left side scales are for k = 0.35.

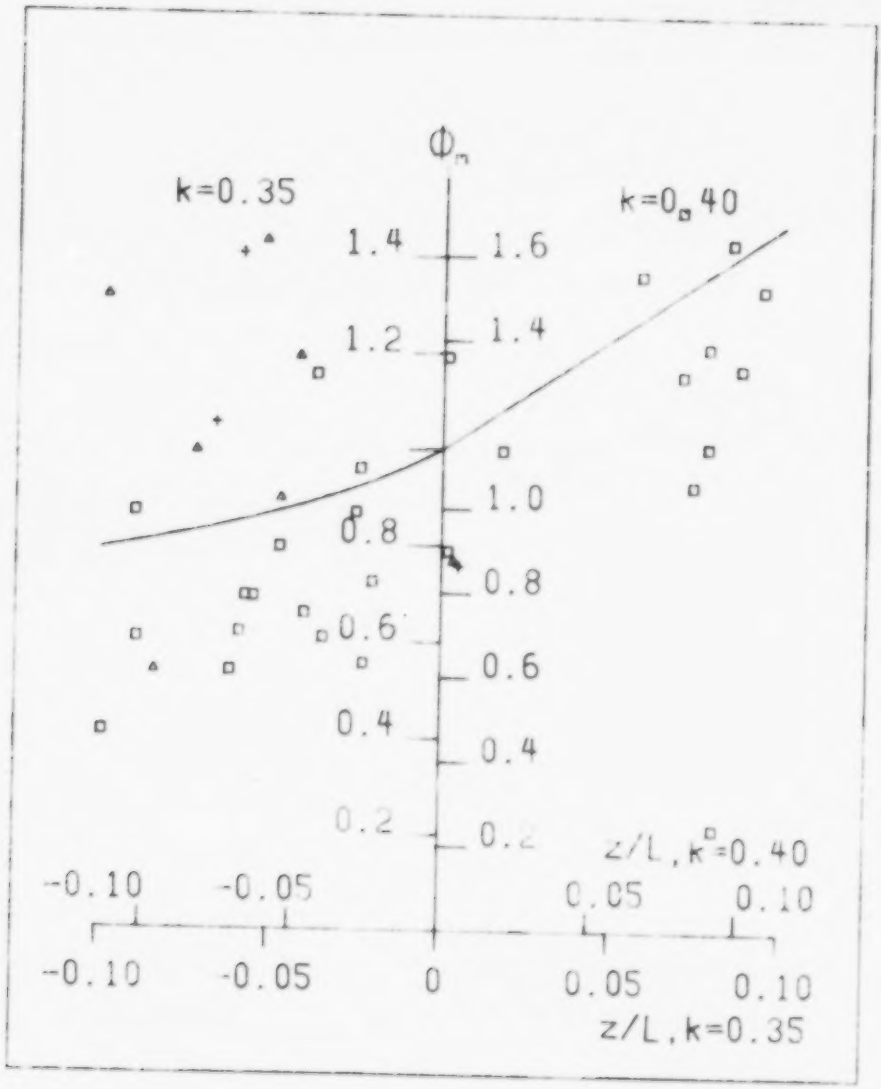

Figure 14. Nondimensional wind shear ϕ_m versus z/L using Method 2. Reference levels are 54.9 m (squares), 114.3 m (triangles), and 160.1 m (crosses). The solid line represents the BWIB line.

SECTION XIII

ROUGHNESS LENGTHS

The terrain to the south was relatively flat, rising less than 8 meters in 900 meters, and more homogeneous than the terrain to the southwest. The roughness elements to the south varied from 60 centimeter grass and shrubs to a plowed field about 300 meters from the tower. The plowed field extended out to 900 meters where tall trees dominated the landscape.

The terrain to the southwest sloped down from the tower about 2.5 degrees in the first 700 meters from the tower. The foliage within the first 300 meters of the tower is similar to that to the south. Beyond 300 meters the terrain consists of trees and patches of pasture land.

Roughness lengths z_o can be determined from the following equation:

$$\ln z - \psi(z/L) = \frac{kU}{u_*} + \ln(z_o). \qquad (13.1)$$

This form allows a linear extrapolation when $\ln(z) - \psi(z/L)$ is plotted versus the mean wind speed, U. In this case, k/u_* is the slope and $\ln(z_o)$ is the intercept for $U = 0$. Use of the expression for $\psi(z/L)$ as derived by Paulson (1970) makes it possible to determine roughness length in unstable conditions. The criterion selected to define unstable conditions was whenever $z/L < -0.05$ at 18.3 meters. Of the 119 data blocks, 40 were determined to be unstable.

Since there were two modes of wind direction in these data, south and southwest (Irwin 1974), data during unstable conditions were separated according to mode based on the 18.3 meter winds. Figure 15

is a plot of the average of all profiles of wind speed versus $\ln(z) - \psi(z/L)$ for each height. The intercept value of south wind profiles using the 18.3 meter and 91.4 meter levels was -2.25, which corresponds to a roughness length near 8 centimeters. The z_o from the southwest was determined similarly to be 36 centimeters. These results seem reasonable considering the terrain features. Panofsky and Townsend (1964) showed that the turbulence parameters measured at a given height reflect the roughness elements of terrain at a distance upwind approximately 10 times the height of the instrument.

Surprisingly, the average profile for the southwest winds yielded a linear relation for all levels of the tower with no abrupt or even noticeable changes in slope. This seems to imply that the z_o for southwest winds experiences no changes in value at distances beyond 300 meters from the tower (this contradicts visual observations of the roughness elements). It is possible that profile averaging has obscured properties of the individual profiles so that this contradiction appears. The same effect may have produced the kink in the mean profile representing the south mode.

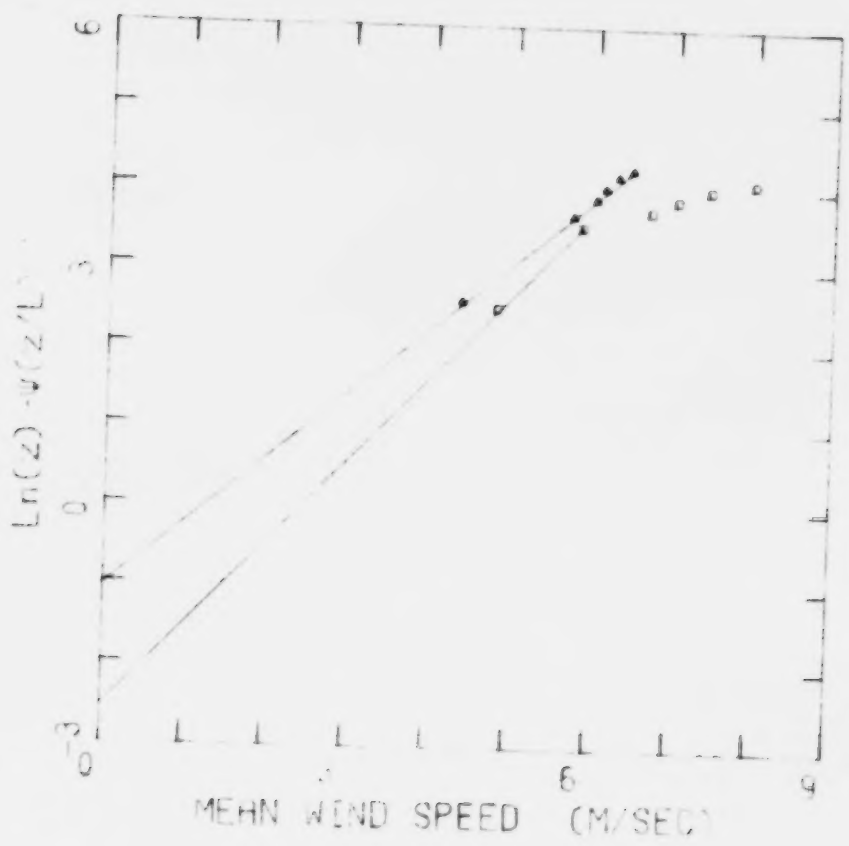

Figure 15. ln(z) - ψ(z/L) versus mean wind speed. Triangles and squares are wind from the southwest and south, respectively.

SECTION XIV

σ_E, σ_A, AND σ_E/σ_A VERSUS z/L

According to similarity theory (see Section XXIV)

$$\sigma_w = u_* \phi_w (z/L) \text{ and} \tag{14.1}$$

$$\sigma_v = u_* \phi_v (z/L), \tag{14.2}$$

where ϕ_w and ϕ_v are universal functions of z/L. Using (13.1), (15.3), and (15.4), we obtain

$$\sigma_E \cong \sigma_w/U \text{ and} \tag{14.3}$$

$$\sigma_A \cong \sigma_v/U . \tag{14.4}$$

Thus $\sigma_E = \dfrac{k\phi_w(z/L)}{\ln z/z_o - \psi(z/L)}$ and $\sigma_A = \dfrac{k\phi_v(z/L)}{\ln z/z_o - \psi(z/L)}$, (14.5 & 14.6)

if $U = \dfrac{u_*}{k}[\ln z/z_o - \psi(z/L)]$. It is seen that σ_E and σ_A are universal functions of z/z_o and z/L. Panofsky and Prasad (1965) produced nomograms relating σ_E and σ_A to $\ln z/z_o$ and z_o/L.

In this analysis σ_E, σ_A, and σ_E/σ_A were plotted against z/L. The plots were split into the two predominant wind direction modes of south and southwest. These modes correspond to roughness lengths of 8 cm (mode 1) and 36 cm (mode 2), respectively, as shown above. The data were split into modes so that the variability of z_o with wind direction could be removed (i.e. z_o = const in each figure). The variables σ_E and σ_A should then display a z/L dependency plus an additional height dependency due to $\ln z/z_o$.

Figures 16 and 17 show σ_A vs z/L for the south (mode 1) and southwest (mode 2) modes respectively. The symbols identify the height at which σ_E and σ_A were measured. The statistic, σ_A, displays more variation and generally higher values for flow over rougher terrain (mode 2)

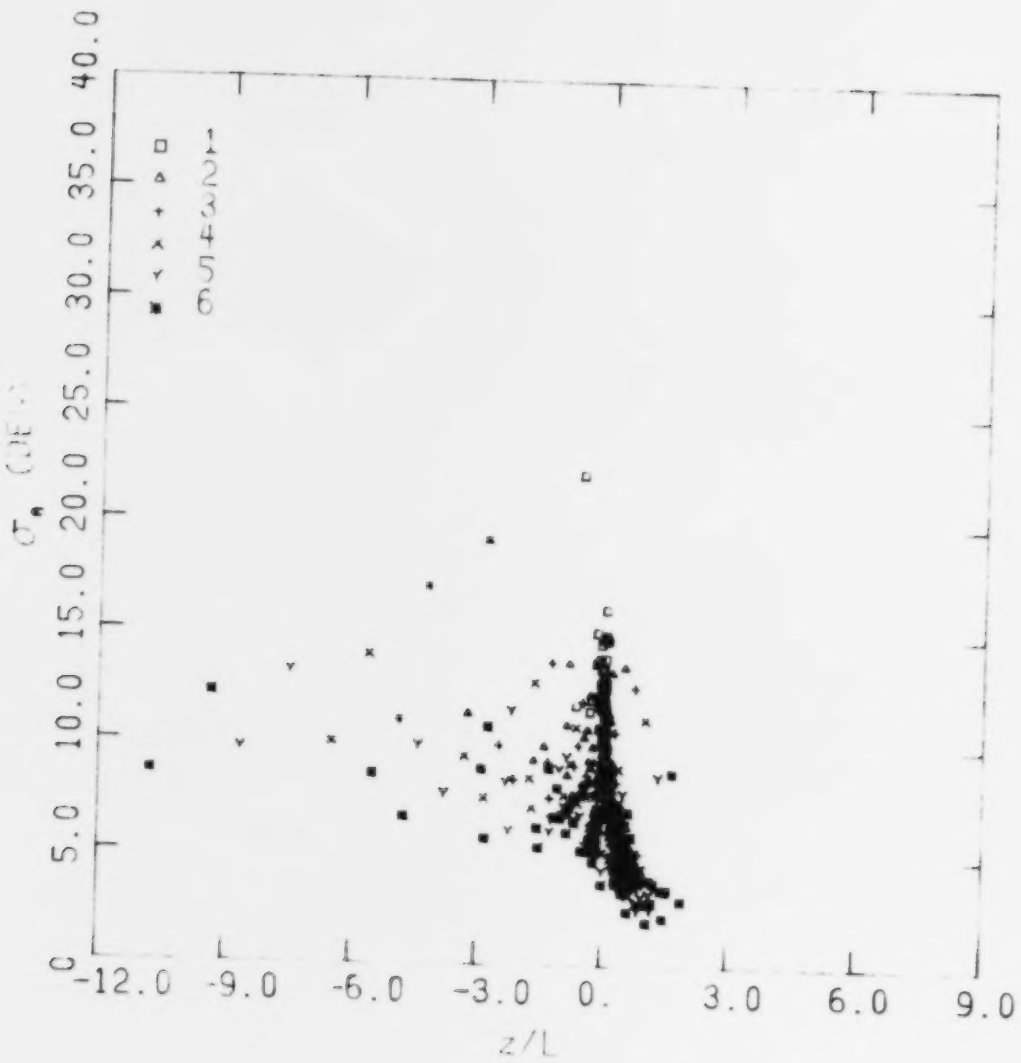

Figure 16. σ_A versus z/L for mode 1 (south winds). Symbols correspond to measurement heights of 18 m (1), 91 m (2), 137 m (3), 183 m (4), 244 m (5), and 305 m (6).

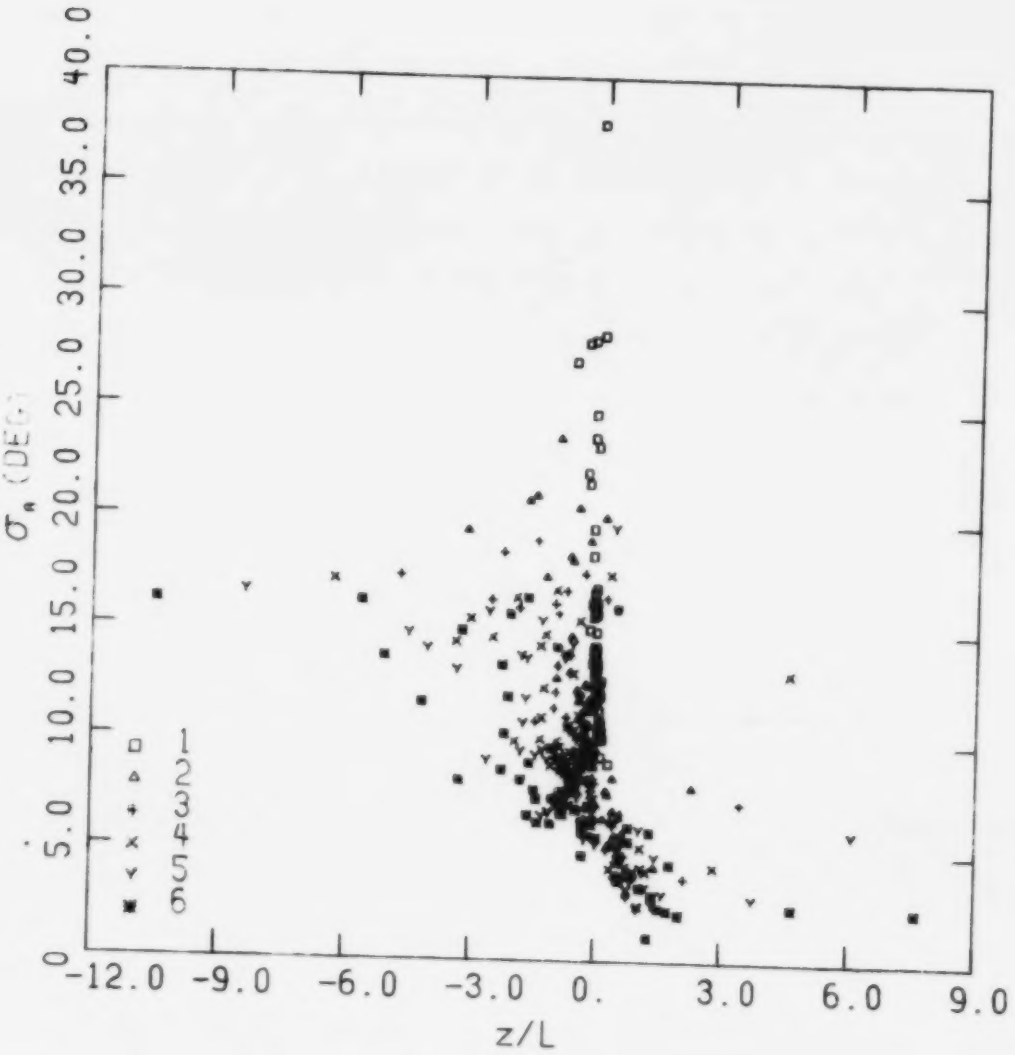

Figure 17. σ_A versus z/L for mode 2 (southwest winds). Symbols correspond to measurement heights of 18 m (1), 91 m (2), 137 m (3), 183 m (4), 244 m (5), and 305 m (6).

than for flow over the terrain associated with the smaller z_o, (mode 1). The σ_A values in Figure 16 for $z/L < 0$ seem to indicate a systematic progression of σ_A to lower values as the reference height increases. This might reflect the effect of sampling times on σ_A, i.e. longer samples of data are needed at the higher levels to obtain a stationary value for the average. If sample lengths are not critical at these heights then σ_A at the lowest levels may be a predictor for the σ_A values higher up on the tower. For $z/L > 0$, σ_A decreases as z/L increases.

The large amount of scatter in σ_A values near $z/L = 0$ is puzzling especially since extremely light winds are absent from the data. W. S. Lewellen has pointed out (personal communication) that according to invariant modeling the atmosphere seems to possess hysteresis, i.e. it remembers its previous stability condition when passing through neutral. This might account for the larger scatter. Other possible explanations are that slight shifts in azimuth reflect strikingly different terrain and that some levels of the tower are affected more than others. This problem is still undergoing investigation.

Values of σ_E were plotted against z/L using data corresponding to modes 1 and 2 (Figures 18 and 19 respectively). The different roughnesses corresponding to modes 1 and 2 apparently have a very significant effect on σ_E (i.e. the highest values for σ_E are approximately twice as large on the mode 2 plot as compared with those on the plot corresponding to mode 1). σ_E tends to take on higher values at the lower reference levels and lower values at higher levels. The mode 1 plot exhibits a tendency for σ_E to be nearly constant with height when σ_E is near its

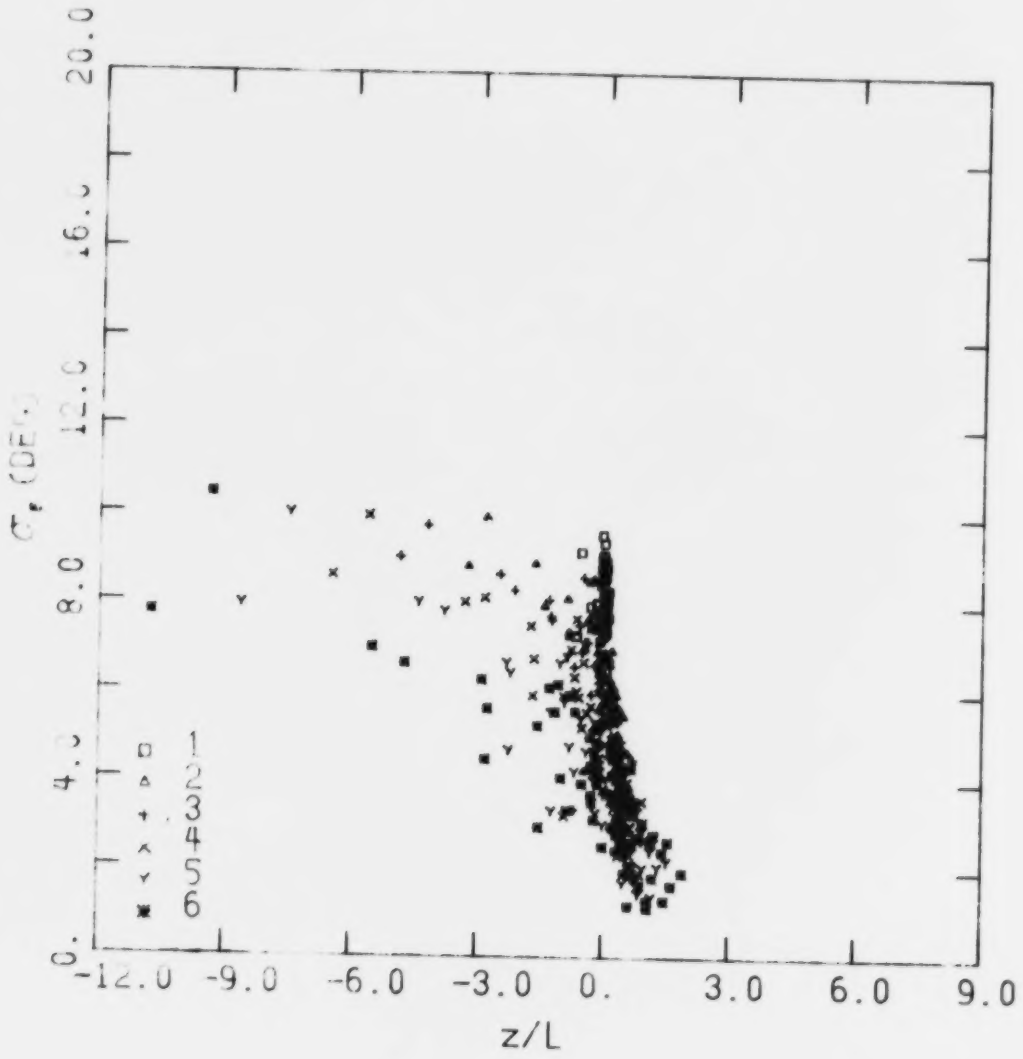

Figure 18. σ_E versus z/L for mode 1 (south winds). Symbols correspond to measurement heights of 18 m (1), 91 m (2), 137 m (3), 183 m (4), 244 m (5), and 305 m (6).

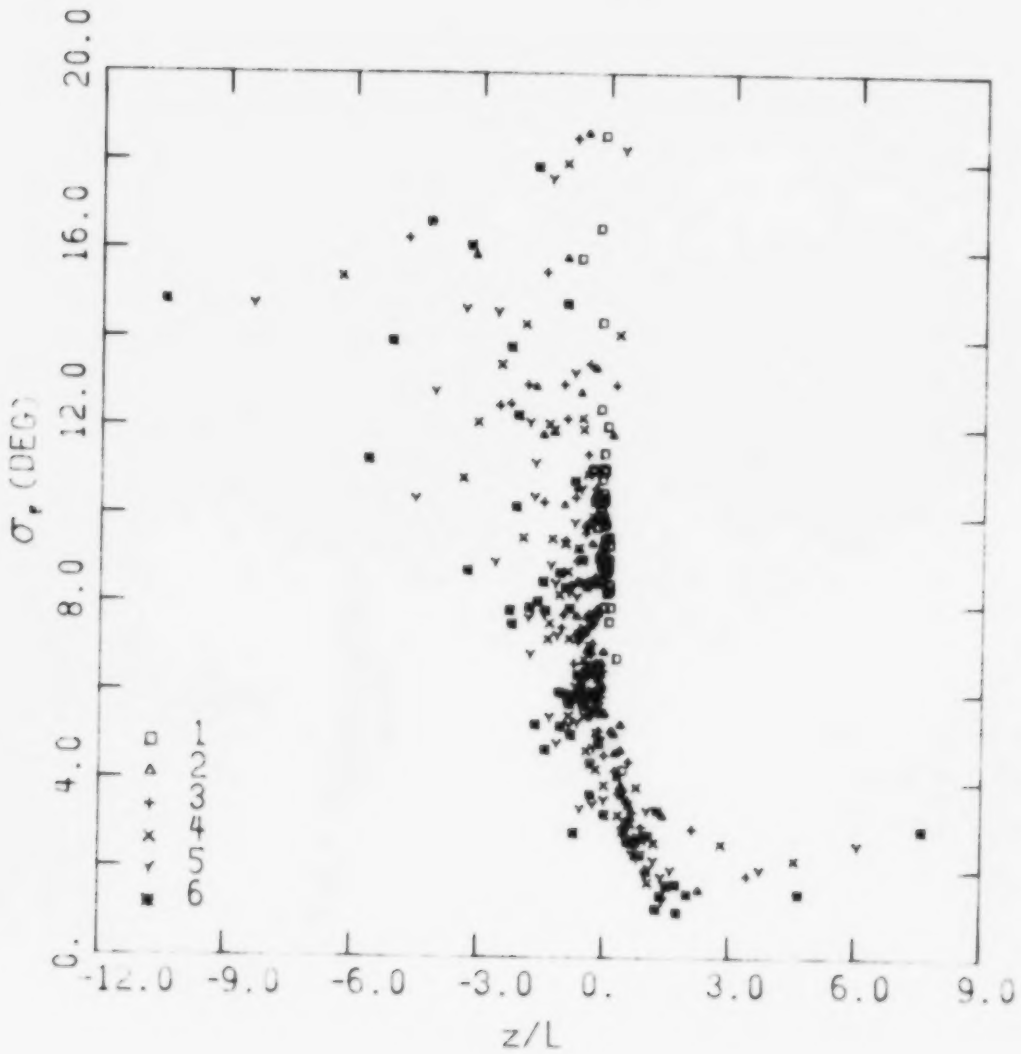

Figure 19. σ_E versus z/L for mode 2 (southwest winds). Symbols correspond to measurement heights of 18 m (1), 91 m (2), 137 m (3), 183 m (4), 244 m (5), and 305 m (6).

maximum value and for σ_E to decrease with height when σ_E is slightly less than the maximum. Figure 19 (mode 2) displays considerably more scatter than Figure 18 (mode 1) which, apparently, is an effect of the rougher fetch traversed by the air.

A qualitative comparison of the plotted σ_E and σ_A trends with the nomograms prepared by Panofsky and Prasad (1965) resulted in fair agreement. If σ_A and σ_E were functions of z/L only, then for any z/L value these parameters should each equal a constant (i.e. no additional height dependency whatsoever). Although there seems to be a dependency on z/L, there are also systematic changes due to other effects that could be attributed to a need for additional length scales.

A result of similarity theory is the relationship,

$$\sigma_E/\sigma_A = \phi_w(z/L)/\phi_v(z/L), \text{ where} \qquad (14.5)$$

ϕ_w and ϕ_v are universal functions of z/L. This result implies that if the conditions for similarity theory are met (i.e. steady-state, horizontally homogeneous, atmospheric surface layer), then σ_E/σ_A should be a function of z/L only. Horizontal homogeneity is not a valid assumption considering the terrain surrounding the tower. Also, most of the levels at which the measurements were made exceed those generally included in the surface layer. Because of these restrictions, σ_E/σ_A may be dependent upon additional scaling parameters.

Plots of σ_E/σ_A vs z/L were produced corresponding to data from modes 1 and 2 (Figures 20 and 21). Although both plots display roughly similar trends, the ratios corresponding to the rougher terrain (mode 2) have a greater range of values than the mode 1 ratios. It is likely that the difference is terrain induced. In general, the ratios tend to be higher under unstable conditions and lower during stable conditions regardless of mode.

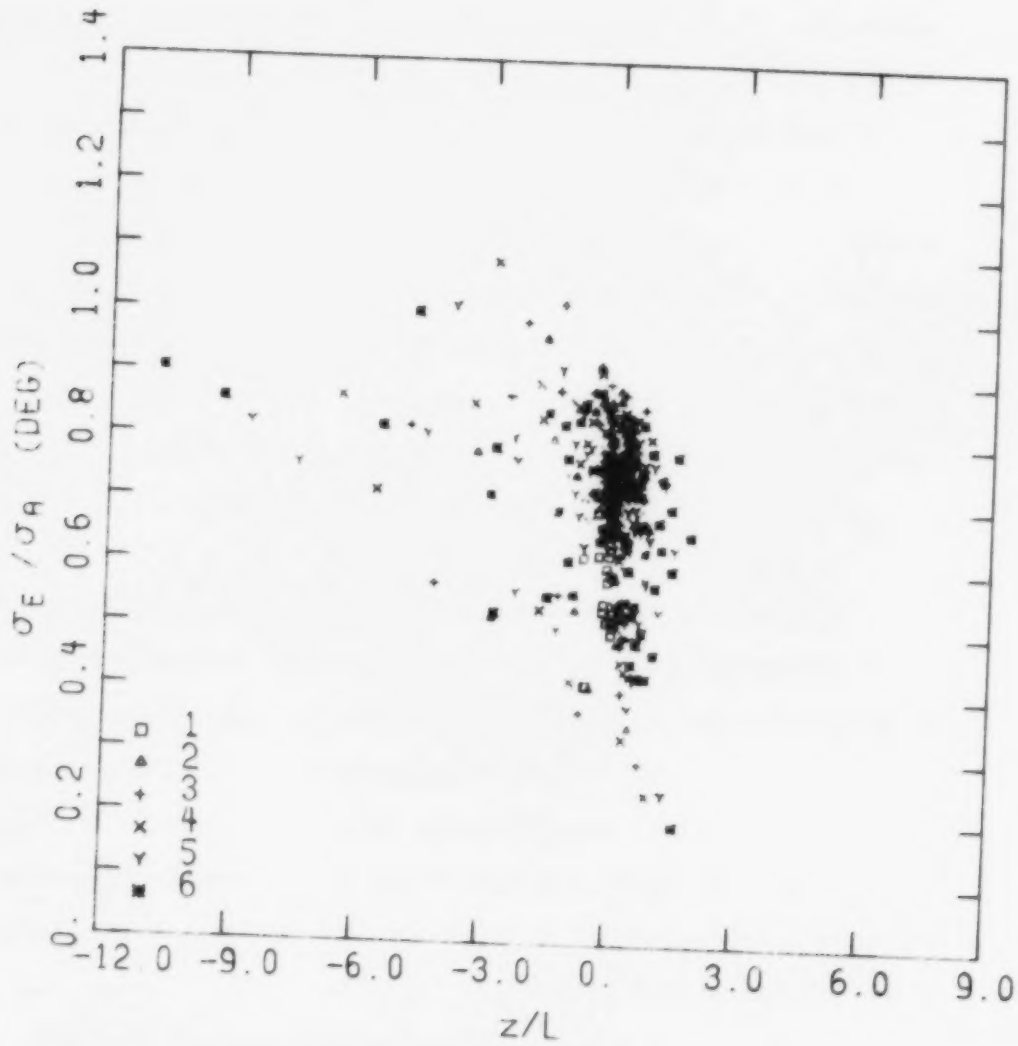

Figure 20. σ_E/σ_A versus z/L for mode 1 (south winds). Symbols correspond to measurement heights of 18 m (1), 91 m (2), 137 m (3), 183 m (4), 244 m (5), and 305 m (6).

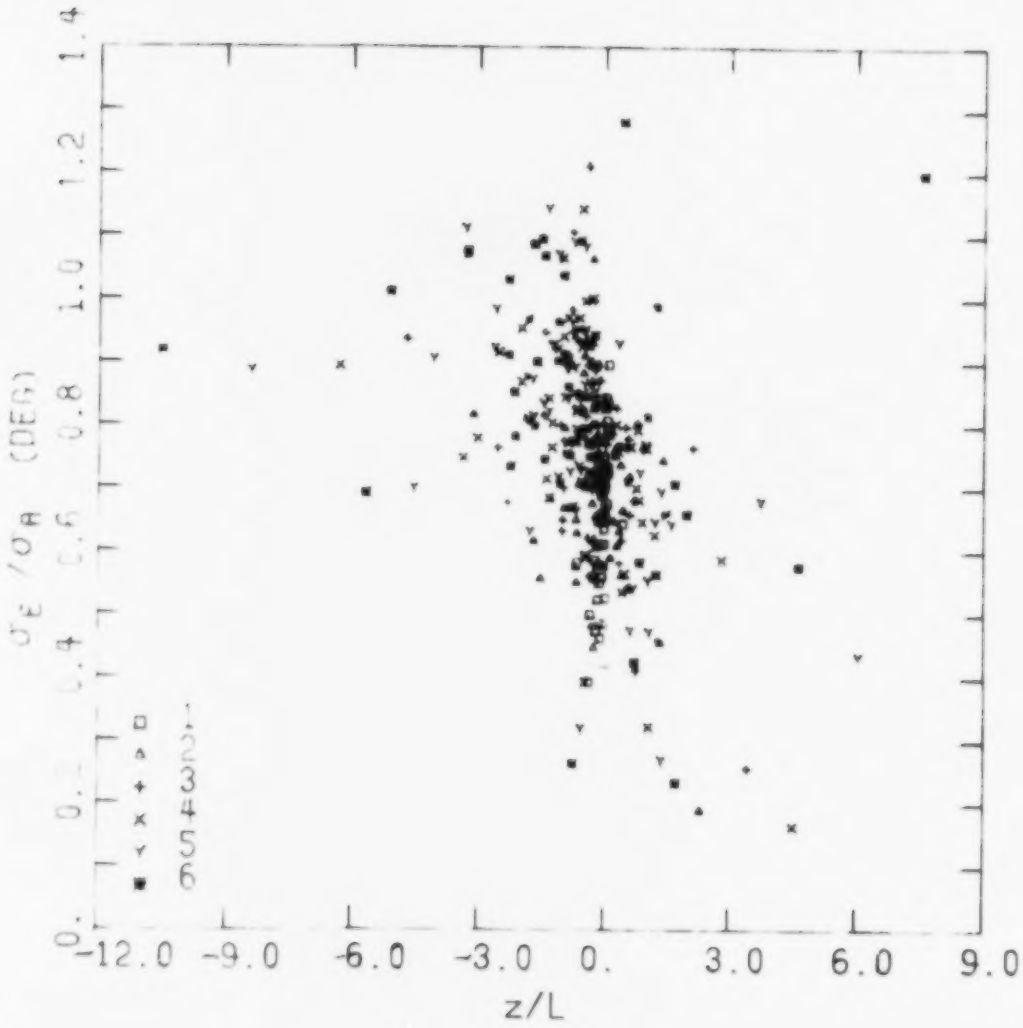

Figure 21. σ_E/σ_A versus z/L for mode 2 (southwest winds). Symbols correspond to measurement heights of 18 m (1), 91 m (2), 137 m (3), 183 m (4), 244 m (5), and 305 m (6).

SECTION XV

TRANSFORMATION RATIOS

In this section the validity of the following approximations is analyzed:

$$\sigma_v = \sigma_A U, \tag{15.1}$$

$$\sigma_w = \sigma_E U . \tag{15.2}$$

The rationale justifying these approximations discussed by Irwin (1974) is based upon the assumption that double correlation terms such as $\overline{v'v'}$ are much larger than the triple and higher correlation terms such as $\overline{v'v'u'}$ and others. If the rather questionable assumption that $\sigma_v = \sigma_u$ is made, then $\sigma_u = \sigma_A U$. These relationships have a practical significance in that the terms on the right can be measured directly from standard equipment making the transformation to a streamline coordinate system unnecessary.

Regression and variance analyses and plots of σ_v/σ_A, σ_u/σ_A and σ_w/σ_E versus the magnitude of the mean vector wind were accomplished using data corresponding to the 119 time periods selected in accordance with the editing criteria of Petersen (1974).

The σ_w/σ_E and σ_v/σ_A (Figures 22 and 23) display remarkably little scatter. The statistics from the regression analyses strongly support this conclusion with R^2's (coefficient of multiple regression) of .993 and .995, respectively. As expected, the σ_u/σ_A (Figure 24) contains considerably more scatter than the others but still results in a respectable $R^2 = .778$. Tables 3, 4, and 5 present regression and variance analyses. In order to determine how much scatter was eliminated through editing, new plots were made using only the points which had

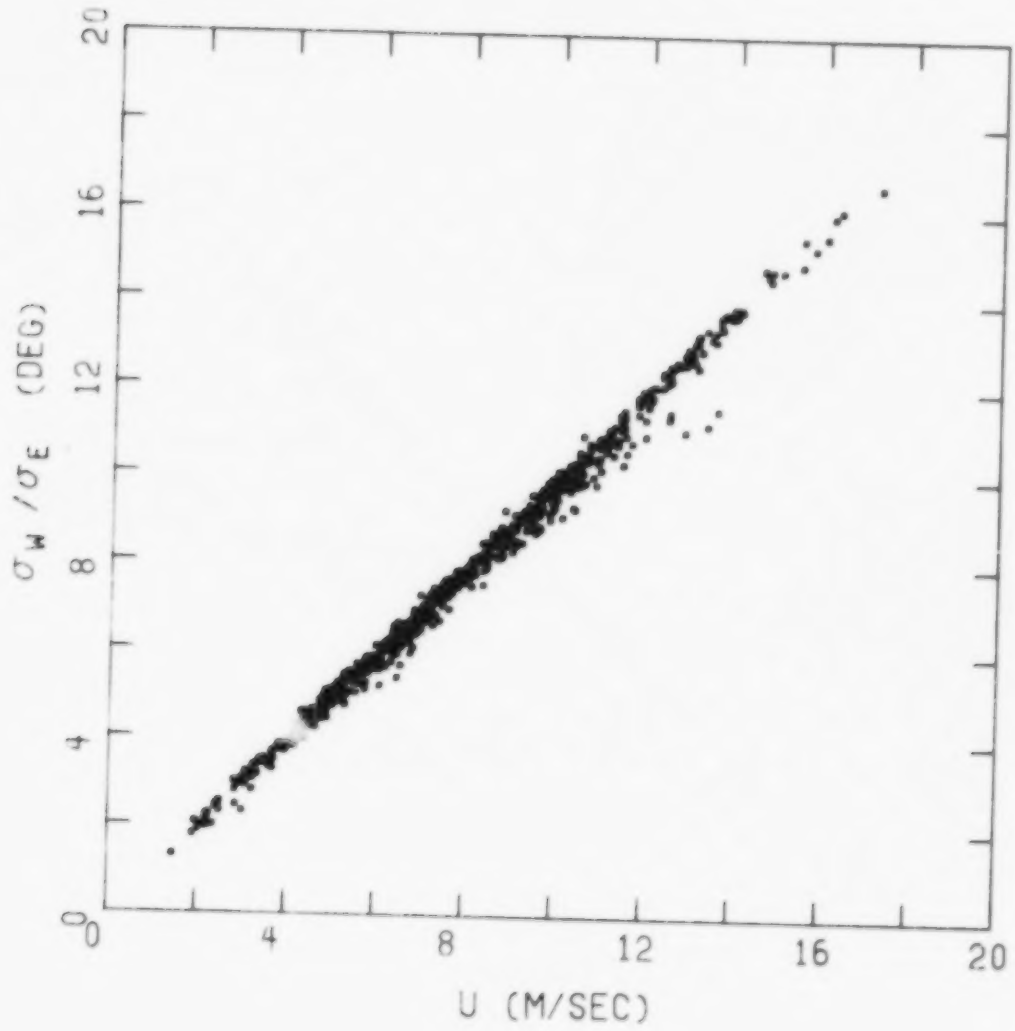

Figure 22. The ratio, σ_w/σ_E, versus the magnitude of the mean vector wind, U, using edited data.

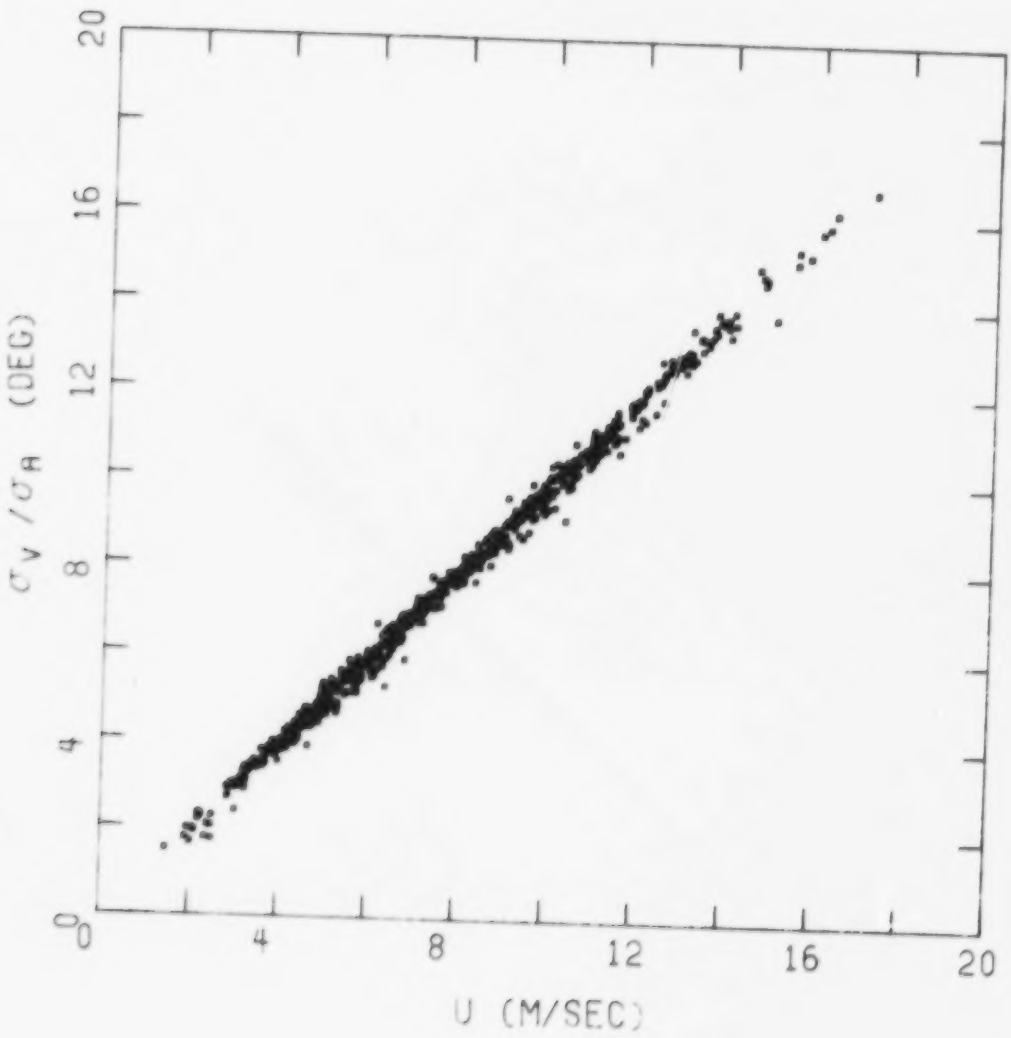

Figure 23. The ratio, σ_v/σ_A, versus the magnitude of the mean vector wind, U, using edited data.

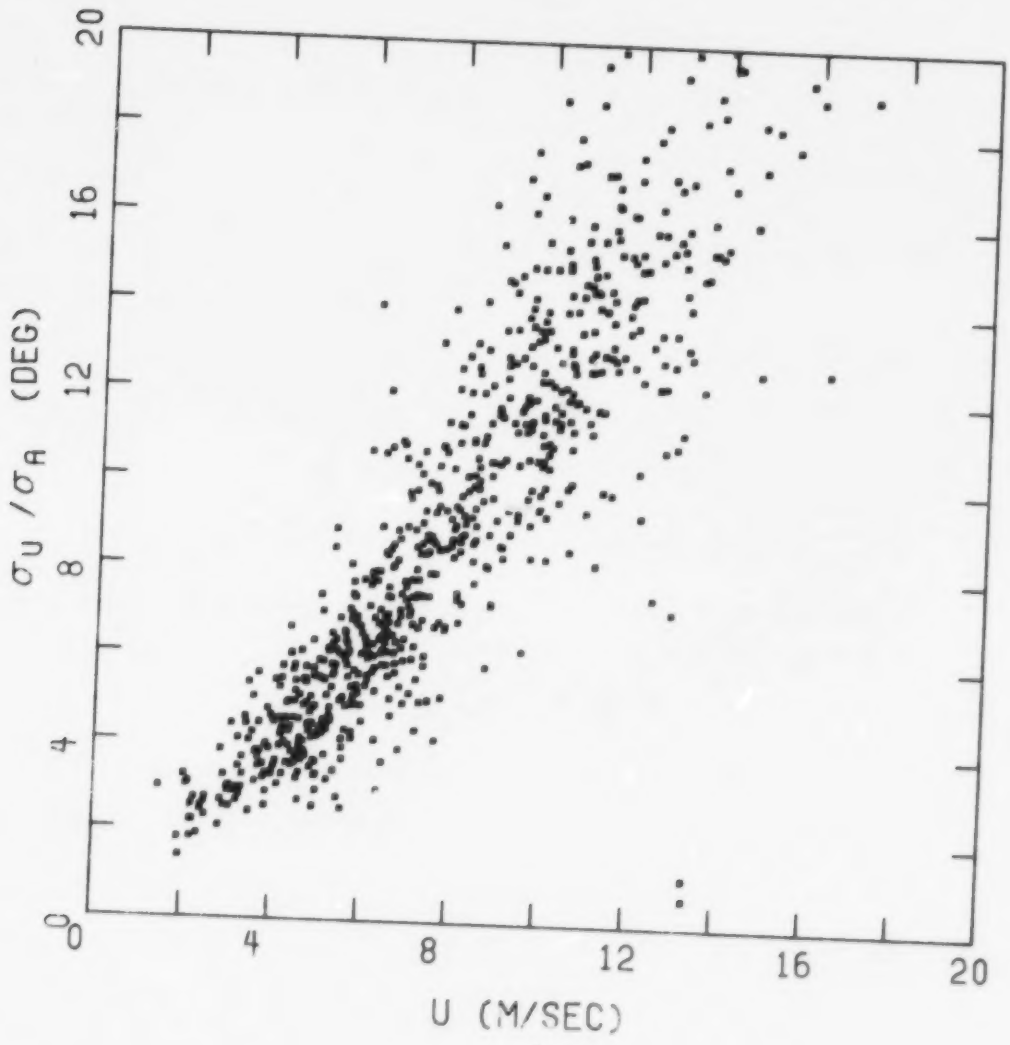

Figure 24. The ratio, σ_u/σ_A, versus the magnitude of the mean vector wind, U, using edited data.

Table 3. ANALYSIS OF VARIANCE FOR σ_u/σ_A VERSUS THE MEAN WIND VELOCITY U

Source of variation	D.F.	Sum of Squares	Mean Square
Average	1	57506.9	57506.9
Linear regression	1	11068.5	11068.5
Deviations from regression	712	3156.5	4.4
Total	714	71731.9	

R^2 = Multiple regression coefficient = 0.778

Assuming the true population model is given by

$$\sigma_w/\sigma_A = \alpha_1 + \beta_1 U + \varepsilon ,$$

where ε is normally distributed with mean 0 and variance σ^{2*}.

The regression model is $\sigma_w/\sigma_A = a_1 + b_1 U$ where a_1 is the estimate of α_1 and b_1 is the estimate of β_1.

The regression coefficients are

$$a_1 = -1.083 \text{ with a standard deviation } \sigma_{a_1} = 0.216 ,$$

$$b_1 = 1.286 \text{ with a standard deviation } \sigma_{b_1} = 0.026.$$

The 95 percent confidence intervals for α_1 and β_1 are given by

$$-1.506 \leq \alpha_1 \leq -0.660 ,$$

$$1.235 \leq \beta_1 \leq 1.337 .$$

* This assumption will be the same for all population models included in this report and will be omitted from all following tables.

Table 4. ANALYSIS OF VARIANCE FOR σ_v/σ_A VERSUS THE MEAN WIND VELOCITY U

Source of variation	D.F.	Sum of Squares	Mean Square
Average	1	41955.0	41955.0
Linear regression	1	6533.7	6533.7
Deviations from regression	712	33.0	0.046
Total	714	48521.7	

$R^2 = 0.995$

Assuming the true population model is $\sigma_v/\sigma_A = \alpha_2 + \beta_2 U + \varepsilon$,

then the regression model is $\sigma_v/\sigma_A = a_2 + b_2 U$,

where $a_2 = -0.063$ and the standard deviation $\sigma_{a_2} = 0.022$,

and $b_2 = 0.988$ and the standard deviation $\sigma_{b_2} = 0.003$.

The 95 percent confidence intervals for α_2 and β_2 are

$$-0.106 \leq \alpha_2 \leq -0.020,$$

$$0.982 \leq \beta_2 \leq 0.994.$$

Table 5. ANALYSIS OF VARIANCE FOR σ_w/σ_E VERSUS THE MEAN WIND VELOCITY U

Source of variation	D.F.	Sum of Squares	Mean Square
Average	1	41169.4	41169.4
Linear regression	1	6357.4	6357.4
Deviations from regression	712	46.1	0.065
Total	714	47572.9	$R^2 = 0.993$

True population model: $\sigma_w/\sigma_E = \alpha_3 + \beta_3 U + \varepsilon$

Regression model: $\sigma_w/\sigma_E = a_3 + b_3 U$

$a_3 = -0.028$ and $\sigma_{a_3} = 0.026$ $\quad$ $b_3 = 0.975$ and $\sigma_{b_3} = 0.003$

The 95 percent confidence intervals for α_3 and β_3 are

$-0.079 \leq \alpha_3 \leq -.023$ and $0.969 \leq \beta_3 \leq 0.981$.

been removed, (Figures 25, 26 and 27). Amazingly little scatter was detected on the σ_w/σ_E and σ_v/σ_A plots indicating that this relationship is very good under any of the conditions encountered in this experiment including "quasi-laminar" flow which occurs at night. The σ_u/σ_A plot showed a fair increase in scatter for the plot using the points removed during editing. Thus editing seemed to improve this relationship more than it did the other two.

Linear regressions of σ_E on σ_w/U and σ_A on σ_v/U were done in order to obtain regression equations for σ_E and σ_A in terms of σ_w/U and σ_v/U directly. The regressions yielded R^2's of 0.991 and 0.982, respectively. The regression and variance analyses are contained in Tables 6 and 7.

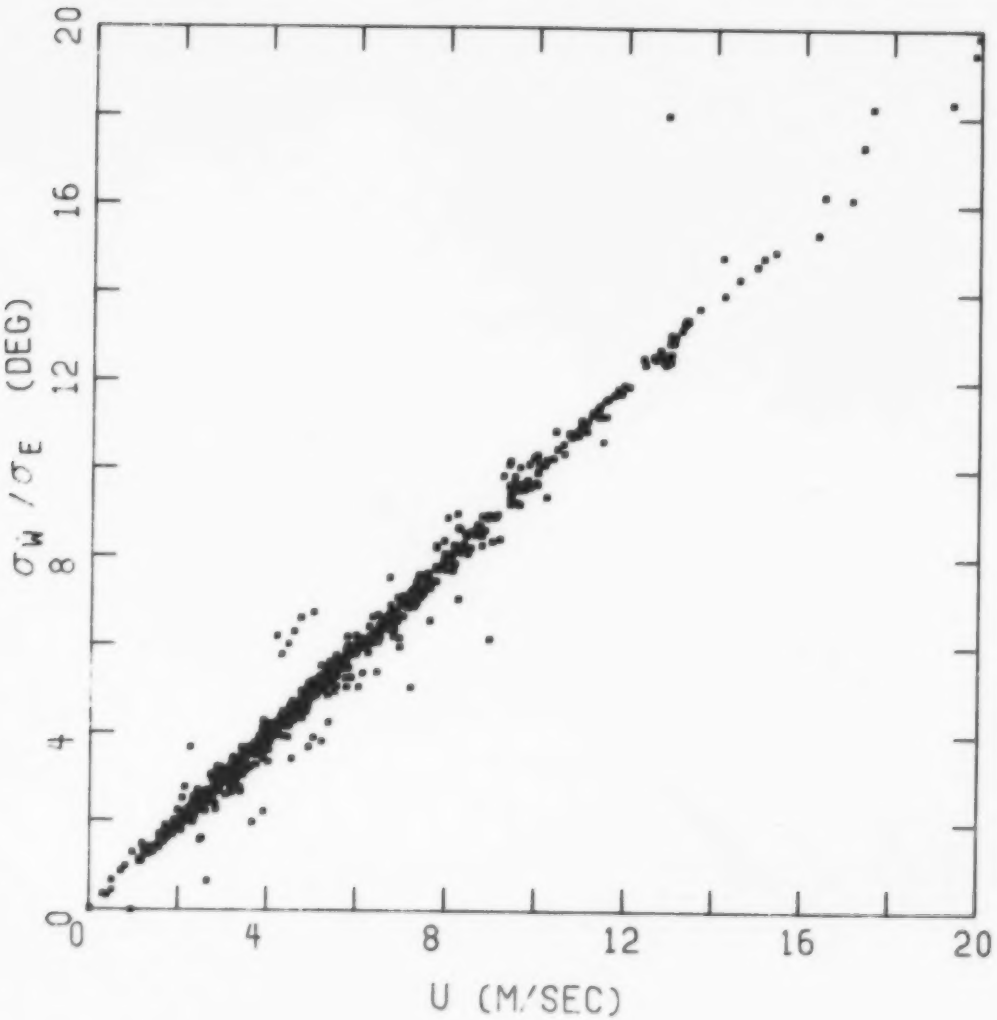

Figure 25. The ratio, σ_w/σ_E, versus the magnitude of the mean vector wind, U, using data removed during editing.

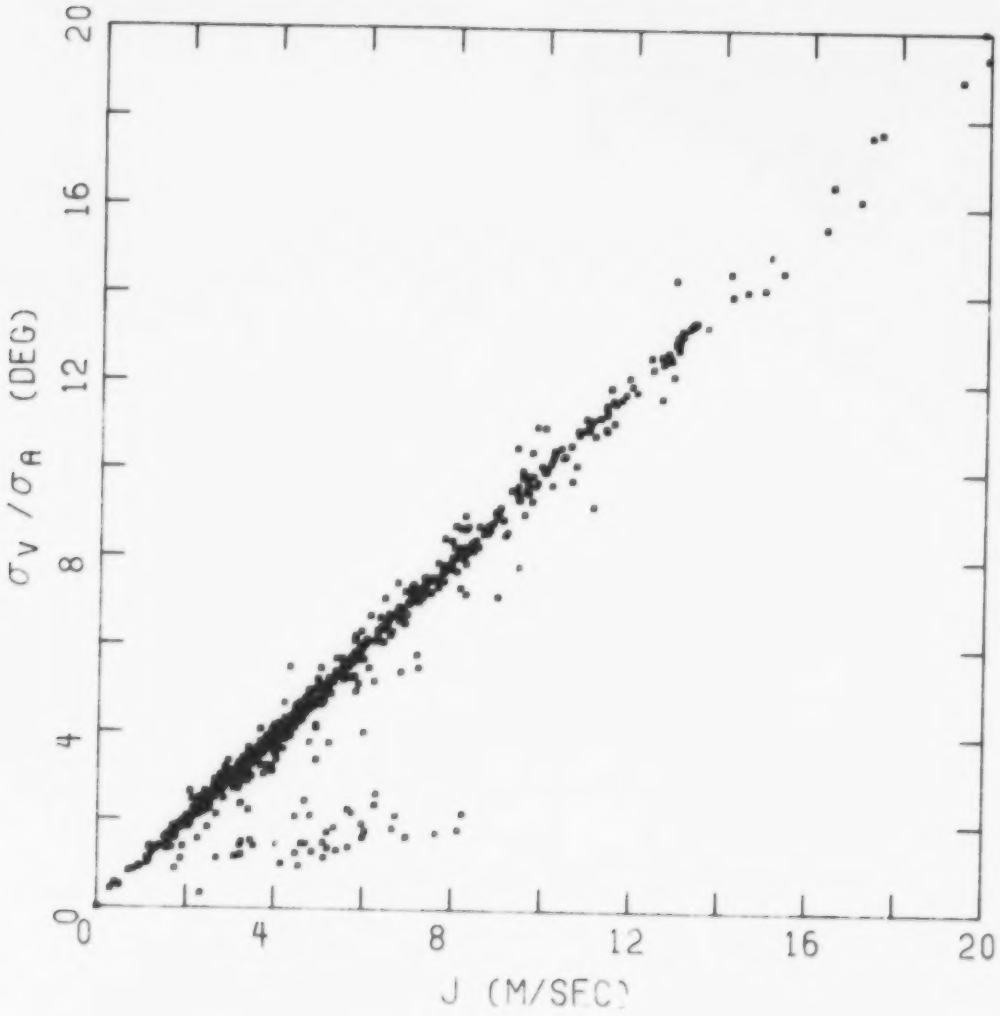

Figure 26. The ratio, σ_v/σ_A, versus the magnitude of the mean vector wind, U, using data removed during editing.

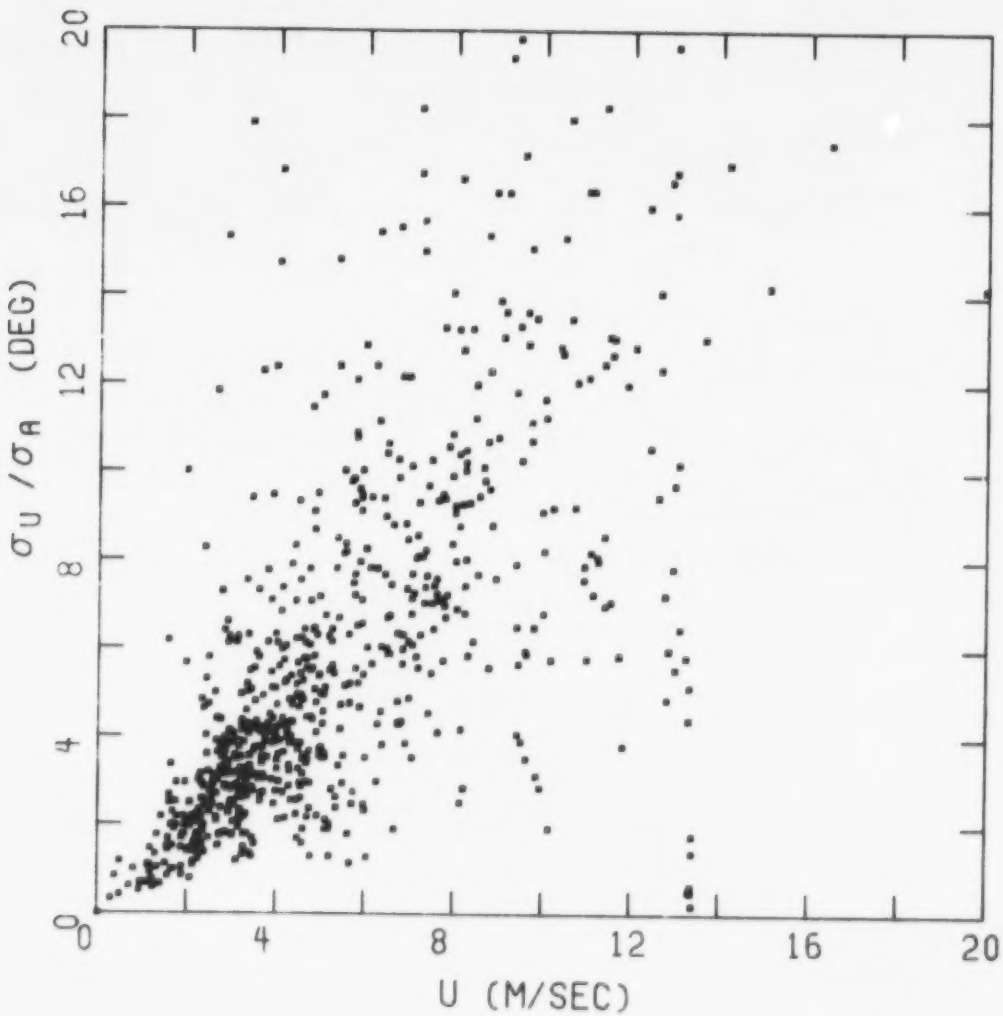

Figure 27. The ratio, σ_u/σ_A, versus the magnitude of the mean vector wind, U, using data removed during editing.

Table 6. ANALYSIS OF VARIANCE FOR σ_E VERSUS σ_w/U.

Source of variation	D.F.	Sum of Squares	Mean Squares
Average	1	8.9865	8.9865
Linear Regression	1	2.4386	2.4386
Deviations from regression	712	0.0229	0.3219×10^{-4}
Total	714	11.448	$R^2 = 0.991$

True Population Model: $\sigma_E = \alpha_1 + \beta_1 \sigma_w/U + \epsilon$

Regression Model: $\sigma_E = a_1 + b_1 \sigma_w/U$

$a_1 = 0.00059$ and $\sigma_{a_1} = 0.00046$. $b_1 = 1.028$ and $\sigma_{b_1} = 0.0037$.

The 95 percent confidence intervals of α_1 and β_1 are

$.00031 \leq \alpha_1 \leq .00149$ and $1.273 \leq \beta_1 \leq 1.287$

Table 7. ANALYSIS OF VARIANCE FOR σ_A VERSUS σ_v/U.

Source of variation	D.F.	Sum of Squares	Mean Squares
Average	1	17.2573	17.2573
Linear Regression	1	4.2286	4.2286
Deviations from regression	712	0.0783	0.00011
Total	714	21.5642	$R^2 = 0.982$

True Population Model: $\sigma_A = \alpha_2 + \beta_2 \sigma_v/U + \epsilon$

Regression Model: $\sigma_A = a_2 + b_2 \sigma_v/U$

$a_2 = -0.00336$ and $\sigma_{a_2} = 0.00090$. $b_2 = 1.049$ and $\sigma_{b_2} = 0.0054$.

The 95 percent confidence intervals of α_2 and β_2 are

$-0.00186 \leq \alpha_2 \leq 0.00512$ and $1.038 \leq \beta_2 \leq 1.059$

It can be concluded from these results that the approximations,

$$\sigma_v \simeq \sigma_A U \quad \text{and} \tag{15.3}$$

$$\sigma_w \simeq \sigma_E U \,, \tag{15.4}$$

are extremely good in the range of velocities used. The approximation,

$$\sigma_u \simeq \sigma_A U \,, \tag{15.5}$$

is not nearly as good as the first two and should probably be written as

$$\sigma_u \simeq \sigma_A (a + b\, U) \,, \tag{15.6}$$

where for this study

$$a = -1.08 \quad \text{and} \tag{15.7}$$

$$b = 1.29. \tag{15.8}$$

It is also implied from these results that triple and higher correlation terms are indeed very small and in most cases can be ignored.

SECTION XVI

σ_w/u_*

Similarity theory predicts that in neutral conditions ($|z/L| < 0.05$) σ_w/u_* is a constant, about 1.2 to 1.3 (see Panofsky, 1972). Irwin (1974) using the SRL-WJBF tower data determined the ratio to be 1.45. Figures 28 through 30 are scatter plots of σ_w/u_* using local u_* values. It is important to note the distinction in the manner in which u_* was calculated. Irwin did not include the $\overline{v'w'}$ component in his calculation of u_*. Figures 31 through 33 are scatter plots of σ_w/u_*, where u_* is the surface u_*. The u_*'s calculated from the Gill anemometer at the 18.3 meter level were used as surface u_*'s. In Table 8 are the mean values of σ_w/u_*, local and surface, for neutral conditions. The weighted mean value for σ_w/u_* (local) for all levels is 1.49. The weighted mean for σ_w/u_* (surface) is 1.27, in good agreement with Panofsky (1972).

Table 8. THE AVERAGE RATIOS OF σ_w/u_* FOR LOCAL u_*'s AND SURFACE u_*'s (GILL u_*'s). THE NUMBERS IN PARENTHESIS ARE THE STANDARD DEVIATIONS.

Level	σ_w/u_* Local	Number of Data Points	σ_w/u_* Gill	Number of Data Points
18.3	1.452 (.144)	54	1.301 (.138)	54
91.4	1.384 (.224)	7	1.354 (.221)	7
137.2	1.458 (.226)	3	1.254 (.256)	3
182.9	1.794 (.037)	2	0.984 (.168)	2
243.8	1.997 (.417)	2	0.899 (.088)	2
304.8	2.229 (.872)	2	0.853 (.049)	2

Weighted mean for σ_w/u_* local = 1.493 (0.193)

Weighted mean for σ_w/u_* Gill = 1.271 (0.185)

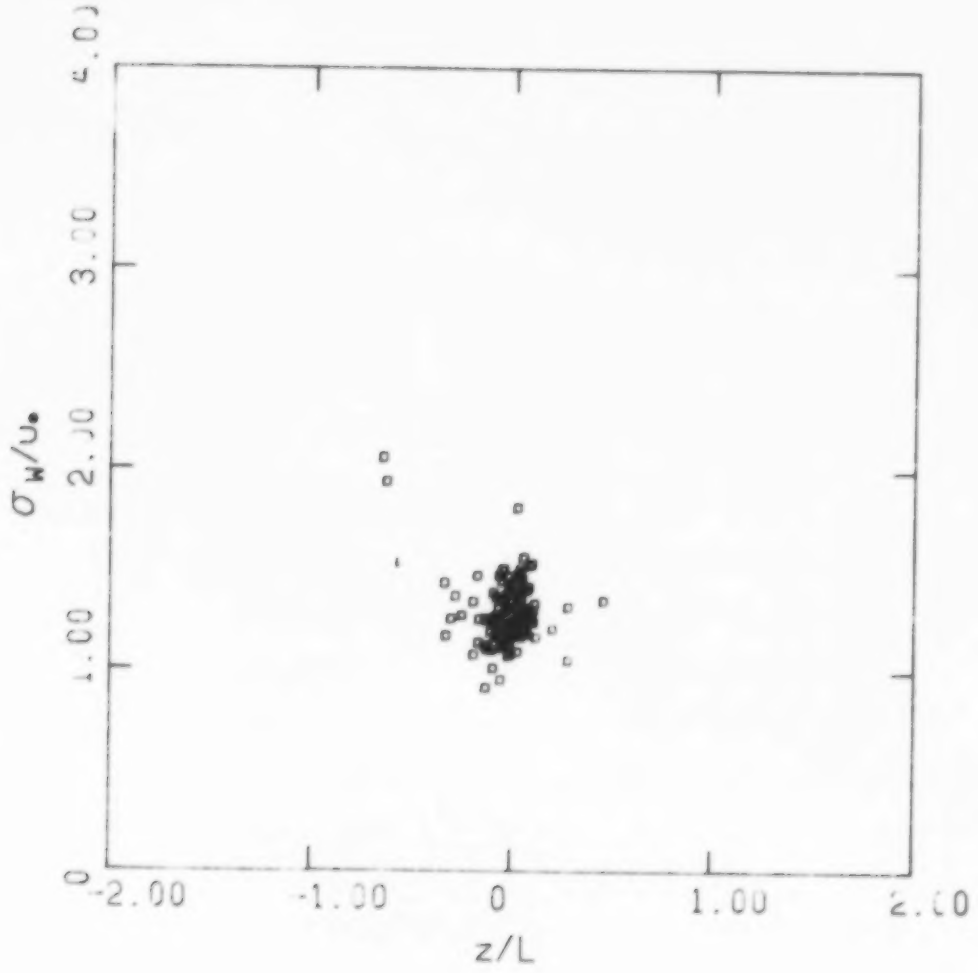

Figure 28. Ratio of standard deviation of vertical velocity to local friction velocity as a function of z/L at 18.3 meters.

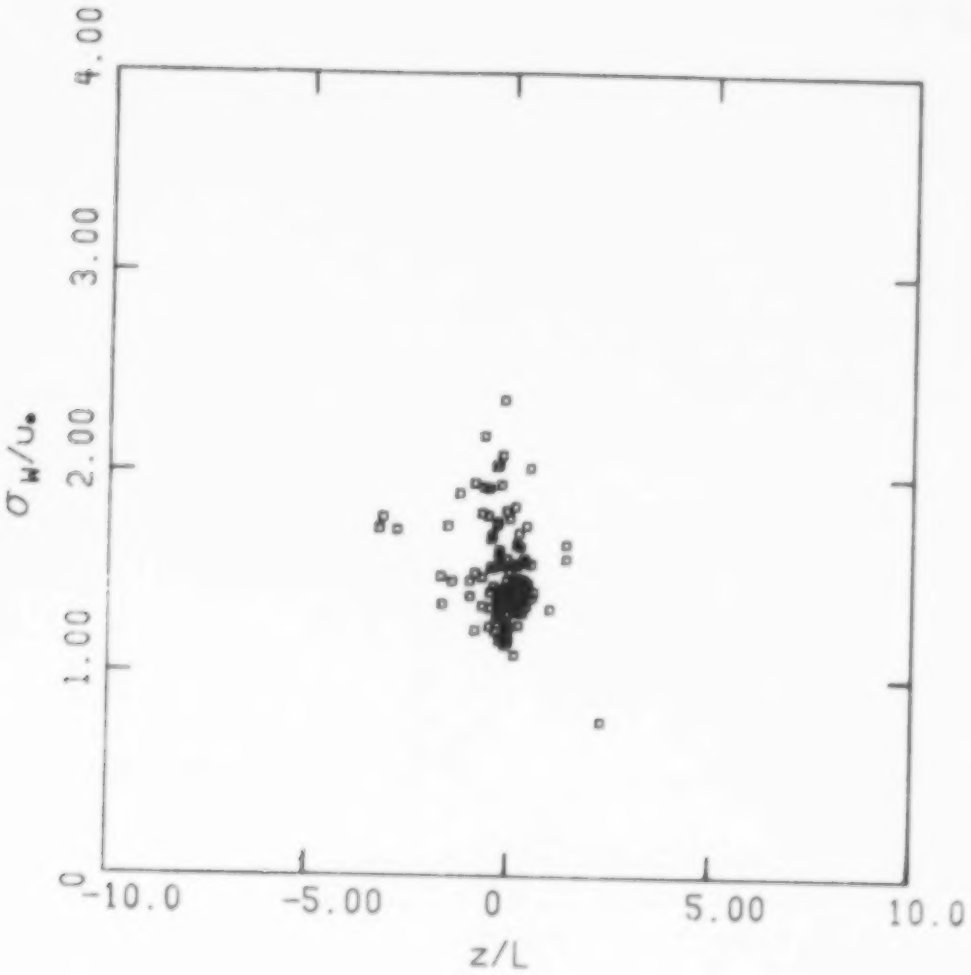

Figure 29. Ratio of standard deviation of vertical velocity to local friction velocity as a function of z/L at 91.4 meters.

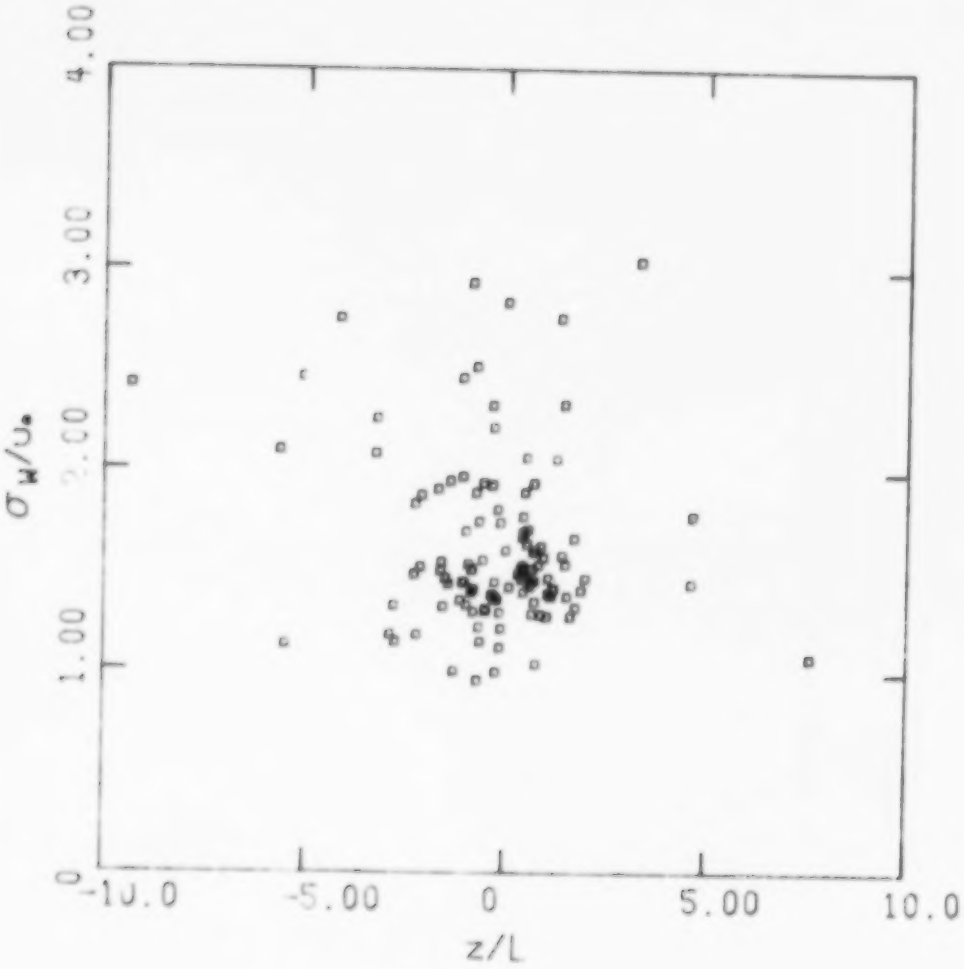

Figure 30. Ratio of standard deviation of vertical velocity to local friction velocity as a function of z/L at 304.8 meters.

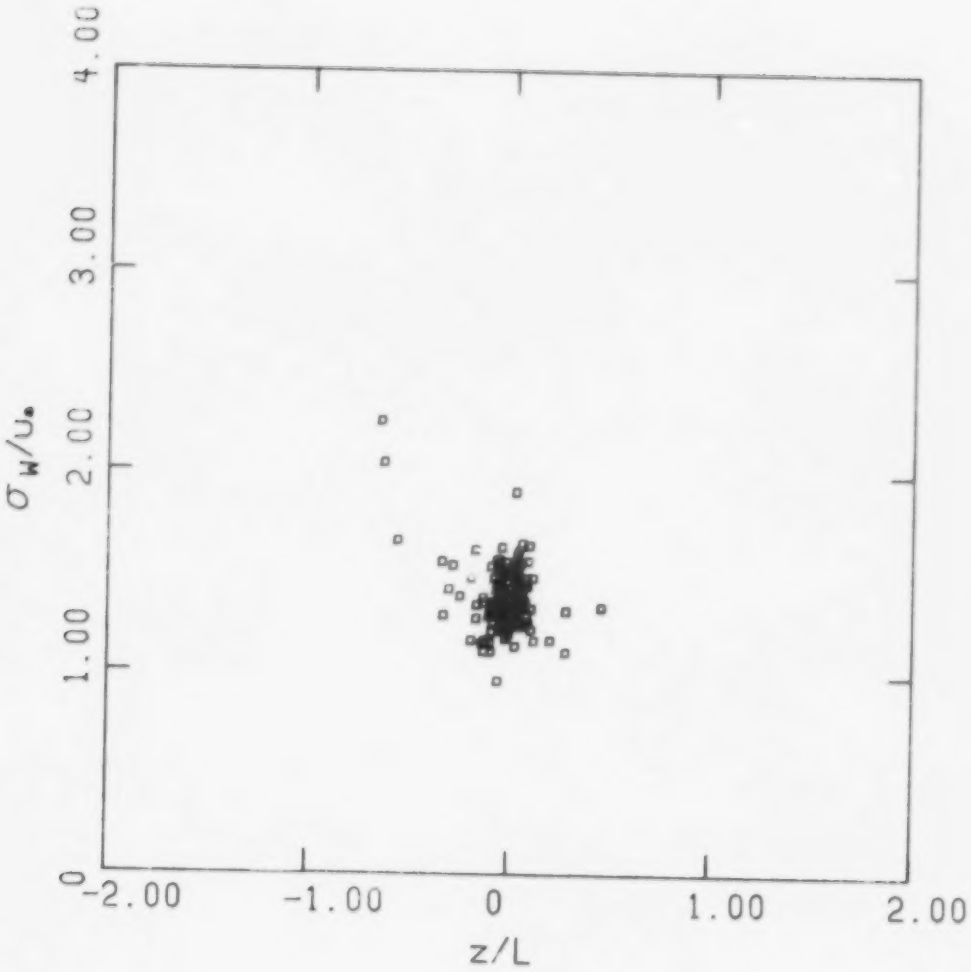

Figure 31. Ratio of standard deviation of vertical velocity to surface friction velocity as a function of z/L at 18.3 meters.

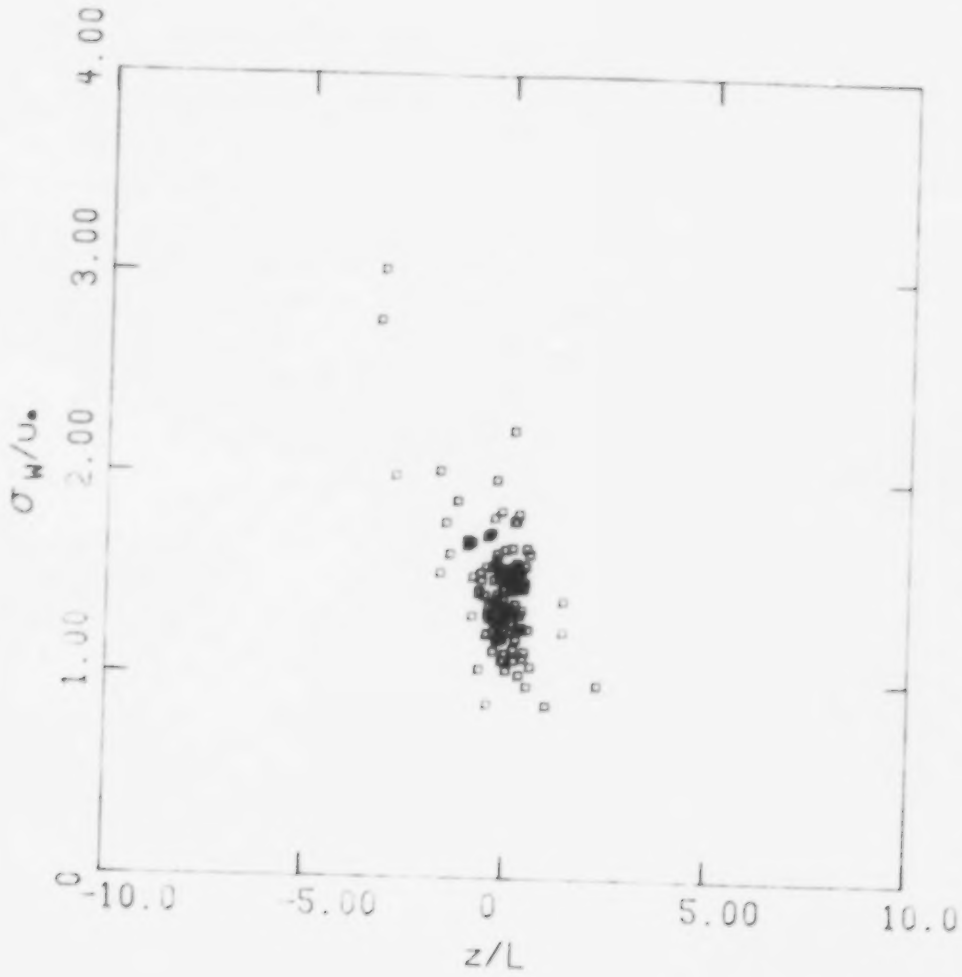

Figure 32. Ratio of standard deviation of vertical velocity to surface friction velocity as a function of z/L at 91.4 meters.

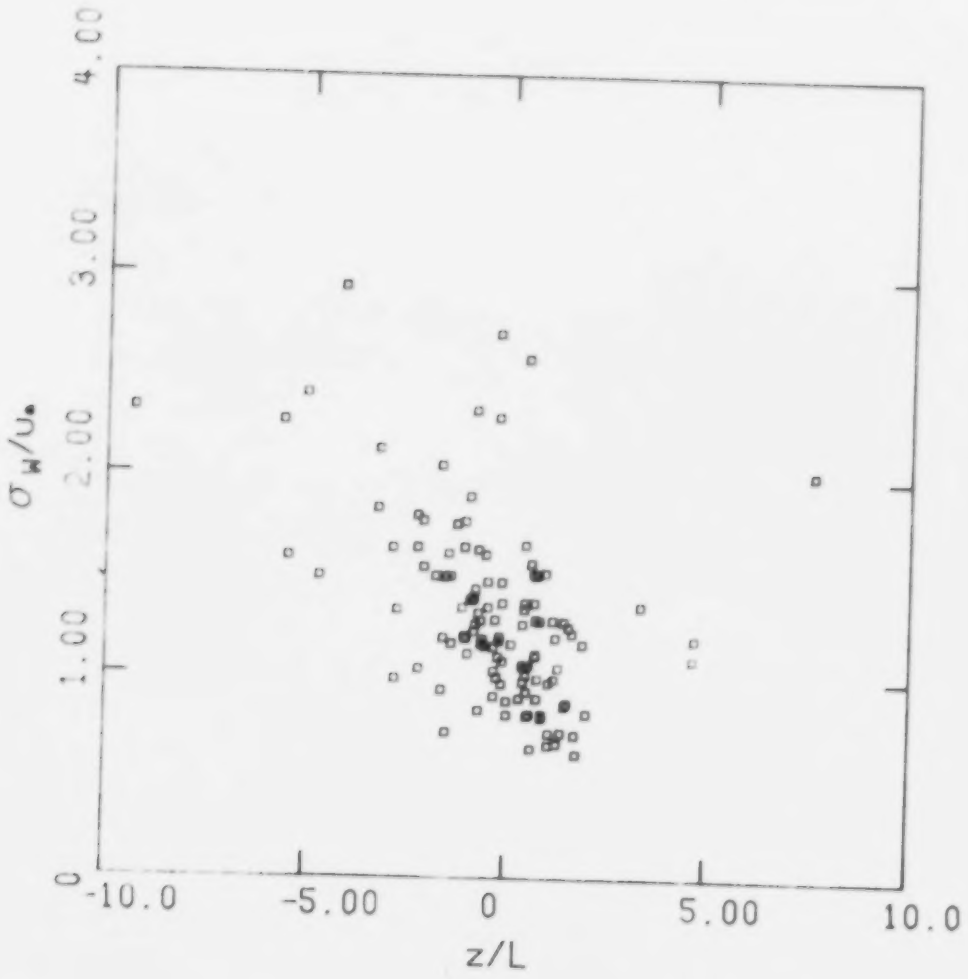

Figure 33. Ratio of standard deviation of vertical velocity to surface friction velocity as a function of z/L at 304.8 meters.

Reproduced from
best available copy.

SECTION XVII

THE SCALING PARAMETER, fz/u_*

It is generally accepted that $u_*/(\beta f)$ is the thickness of the neutral Ekman layer, where β is a constant between 0.3 and 0.5 and u_* and f denote the surface friction velocity and Coriolis parameter, respectively. If σ_A and σ_E were functions of z/L only, then for any z/L value these parameters should each equal a constant (i.e., no additional height dependency whatsoever). This, however, has not been found to be the case. Although there seems to be a dependency on z/L, there are also systematic changes due to other effects that could be attributed to a need for additional length scales.

Above the surface layer (i.e., the Ekman layer) the Coriolis parameter becomes important. This suggests a scaling height related to the thickness of the Ekman layer under neutral conditions, fz/u_*. Other choices of additional scaling parameters include z/z_o where z_o is the surface roughness length and z/z_o' where z_o' is the upstream or bulk roughness length associated with a sufficiently long fetch (possibly 15 km) traversed by the air. Blackadar and Tennekes (1968) derived a velocity defect law valid in the Ekman layer under conditions of steady, horizontally homogeneous flow and for neutral atmospheric stability that was a function of $\ln fz/u_*$. The relationship between σ_E and $\ln fz/u_*$ is discussed in Appendix D.

In this analysis data corresponding to neutral stabilities, defined as $z/L \leq |0.05|$ were selected resulting in 54 time blocks of data, two of which were discarded because both the wind azimuth and the elevation angle standard deviations were anomalously large at all levels of the

tower. For convenience, values for the same time blocks were used for all levels of the tower. This implies a linear increase in ranges of z/L values with height. For example, at the 304.8 m level, instead of a range of z/L values between ±0.05, the range is ±0.83. It was expected that this biasing effect would produce some scatter in the plots for the higher levels. Values of fz/u_* were computed for each set of σ_E and σ_A using a Coriolis parameter for 33° latitude and the surface friction velocity, u_*.

Figure 34 is a scatter plot of σ_E versus fz/u_* for six levels (18.3 to 304.8 meters) and neutral stabilities ($-0.05 \leq z/L \leq +0.05$) defined at 18.3 m. The solid regression line accounting for 70 percent of the variation of σ_E with fz/u_* is described by

$$\sigma_E = -5.9 - 3.8 \ln (fz/u_*) - 0.2 [\ln (fz/u_*)]^2. \qquad (17.1)$$

Tables 9 and 11 provide regression and variance analysis data from linear and quadratic regression of σ_E on $\ln fz/u_*$.

Figure 35 is an analogous plot for σ_A versus fz/u_* -- again for all levels (18.3 meters to 304.8 meters) and neutral stability ($-0.05 \leq z/L \leq +0.05$) defined at 18.3 meters. The fitted line accounting for more than 67 percent of the variation of σ_A with fz/u_* is described by

$$\sigma_A = -1.75 - 2.35 \ln fz/u_*.$$

The plots show a distinct dependency on fz/u_*. Some striking features are: (1) a similarity in trend and in scatter between the plot of σ_E and the plot of σ_A. (2) An extremely rapid drop in the ordinate value with a relatively minute increase in the abscissa at the low end of the scale. (3) σ_E and σ_A seem to approach fixed values asymptotically at large values of fz/u_*.

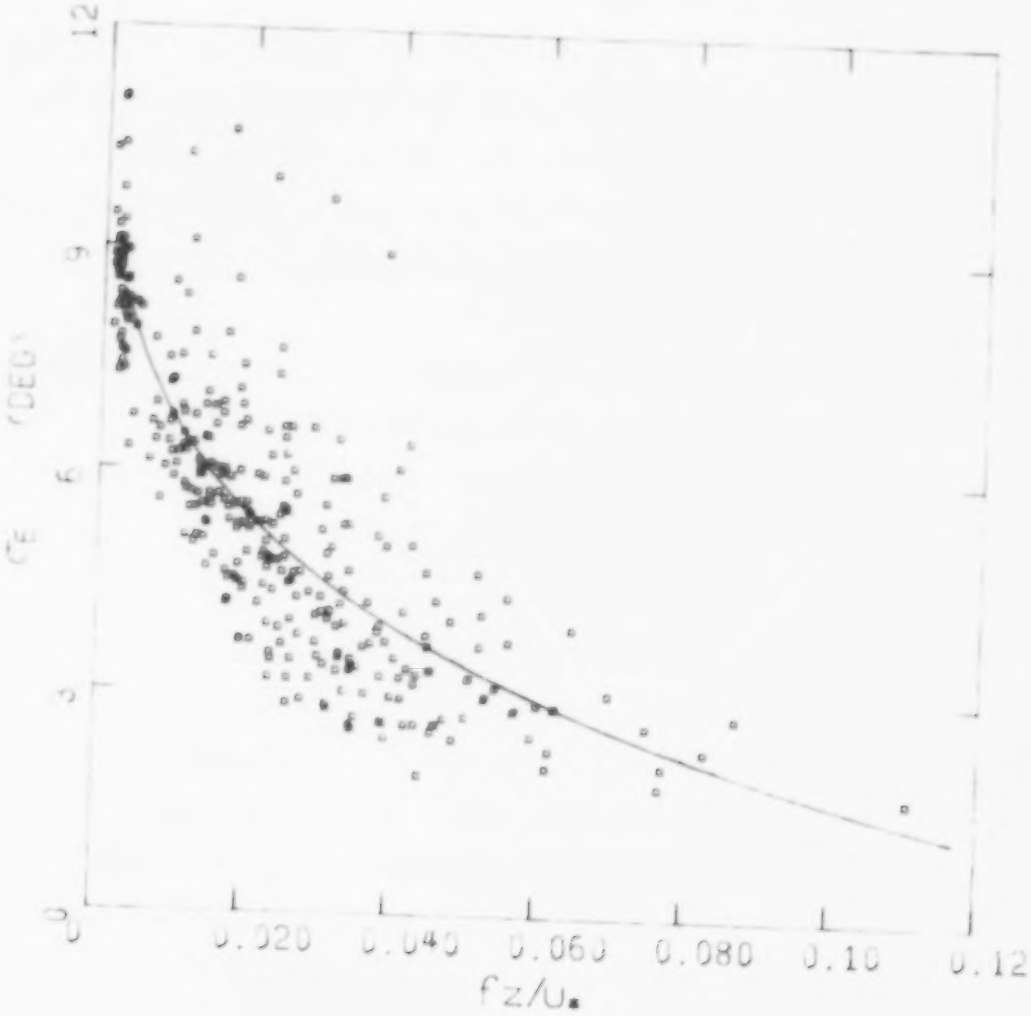

Figure 34. σ_E versus the scaling parameter, fz/u_*, for all levels (18.3 to 304.8 m) under near neutral stability conditions ($-0.05 \leq z/L \leq 0.05$) as defined at 18.3 m. The solid line is a regression fit that accounts for 70 percent of the variation of σ_E with ln fz/u_*. The regression equation is:
$\sigma_E = -5.9 - 3.8 \ln fz/u_* - 0.2(\ln fz/u_*)^2$.

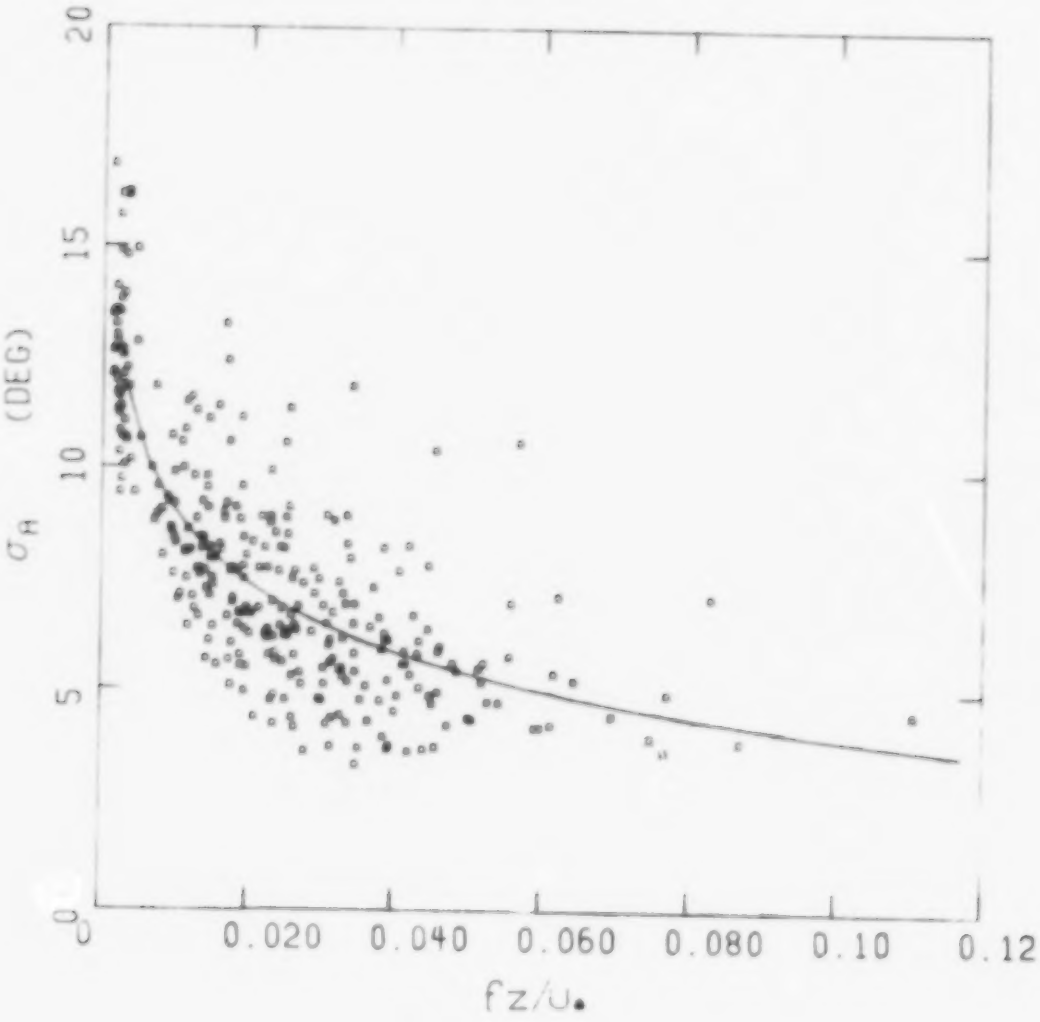

Figure 35. σ_A versus the scaling parameter, fz/u_*, for all levels (18.3 to 304.8 m) under near neutral stability conditions ($-0.05 \leq z/L \leq 0.05$) as defined at 18.3 m. The solid line is a regression fit that accounts for 67 percent of the variation of σ_E with ln fz/u_*. The regression equation is:

$\hat{\sigma}_A = -1.75 - 2.35 \ln fz/u_*$.

Table 9. LINEAR REGRESSION AND VARIANCE ANALYSIS OF σ_E ON $\ln(fz/u_*)$ FOR NEAR NEUTRAL STABILITY.

Source of variation	Sum of Squares	D.F.	Mean Square	F
Average	9604.750	1	9604.750	2251.09
Linear Term	906.099	1	906.099	667.44
Total due to regression	10510.848	2	5255.422	3871.21
Deviations from regression	420.846	310	1.358	
Total	10931.695	312	35.037	$R^2 = 0.684$

True Population Model: $\sigma_E = \alpha_1 + \beta_1 \ln(fz/u_*) + \epsilon$

Regression Model: $\sigma_E = a_1 + b_1 \ln(fz/u_*)$

$a_1 = -1.465$ and $s_{a_1} = 0.028$. $b_1 = -1.717$ and $s_{b_1} = 0.066$

The 95 percent confidence intervals for α_1 and β_1 are

$-1.520 \leq \alpha_1 \leq -1.410$ and $-1.846 \leq \beta_1 \leq -1.588$

Table 10. LINEAR REGRESSION AND VARIANCE ANALYSIS OF σ_A ON $\ln(fz/u_*)$ FOR NEAR NEUTRAL STABILITY.

Source of variation	Sum of Squares	D.F.	Mean Square	F
Average	19271.445	1	19271.455	2366.25
Linear Term	1701.895	1	1701.895	634.85
Total due to regression	20973.305	2	10486.652	3911.90
Deviations from regression	831.020	310	2.681	
Total	21804.324	312	69.886	$R^2 = 0.672$

True Population Model: $\sigma_E = \alpha_1 + \beta_1 \ln(fz/u_*) + \varepsilon$

Regression Model: $\sigma_E = a_1 + b_1 \ln(fz/u_*)$

$a_1 = -1.753$ and $\sigma_{a_1} = 0.393$. $b_1 = -2.353$ and $\sigma_{b_1} = 0.093$

The 95 percent confidence intervals for α_1 and β_1 are

$-2.523 \leq \alpha_1 \leq -0.982$ and $-2.535 \leq \beta_1 \leq -2.170$

Table 11. QUADRATIC REGRESSION AND VARIANCE ANALYSIS OF σ_E ON $\ln(fz/u_*)$ FOR NEAR NEUTRAL STABILITY.

Source of variation	Sum of Squares	D.F.	Mean Square	F
Average	9604.750	1	9604.750	2251.09
Linear Term	906.099	1	906.099	667.44
Quadratic Term	19.960	1	19.960	15.38
Total due to regression	10530.809	3	3510.270	2705.69
Deviations from regression	400.886	109	1.297	
Total	10931.695	312	35.037	$R^2 = 0.70$

True Population Model: $\sigma_E = a_1 + a_1 \ln(fz/u_*) + a_2[\ln(fz/u_*)]^2 + \varepsilon$

Regression Model: $\sigma_E = a_1 + b_1 \ln(fz/u_*) + b_2[\ln(fz/u_*)]^2$

$a_1 = -5.941$ and $\sigma_{a_1} = 1.173$. $b_1 = -3.811$ and $\sigma_{b_1} = 0.059$.

$b_2 = -0.231$ and $\sigma_{b_2} = 0.059$.

The 95 percent confidence intervals for a_1, β_1 and β_2 are

$-8.240 \leq a_1 \leq -3.642$, $-4.865 \leq \beta_1 \leq -2.756$,

and $-0.347 \leq \beta_2 \leq -0.172$

Table 12. QUADRATIC REGRESSION AND VARIANCE ANALYSIS OF σ_A ON $\ln(fz/u_*)$ FOR NEAR NEUTRAL STABILITY.

Source of variation	Sum of Squares	D.F.	Mean Square	F
Average	19271.445	1	19271.445	2366.25
Linear Term	1701.859	1	1701.859	634.85
Quadratic Term	1.690	1	1.690	0.63(NS)
Total due to regression	20974.992	3	6991.664	2605.03
Deviations from regression	829.329	309	2.684	
Total	21804.324	312	69.886	$R^2 = 0.672$

(NS) indicates the term is not statistically significant at the .05 level as determined by the F-Test. This indicates the true model should be a linear relation.

True Population Model: $\sigma_A = \alpha_1 + \beta_1 \ln(fz/u_*) + \beta_2[\ln(fz/u_*)]^2 + \epsilon$

Regression Model: $\sigma_A = a_1 + b_1 \ln(fz/u_*) + b_2[\ln(fz/u_*)]^2$

$a_1 = -0.451$ and $\sigma_{a_1} = 1.687$. $b_1 = -1.744$ and $\sigma_{b_1} = 0.773$.

$b_2 = 0.067$ and $\sigma_{b_2} = 0.085$

The 95 percent confidence intervals for α_1, β_1 and β_2 are

$-3.758 \leq \alpha_1 \leq 2.856$, $-3.260 \leq \beta_1 \leq -0.229$,

and $-0.100 \leq \beta_2 \leq 0.234$.

Tables 10 and 12 provide regression and variance analysis data from linear and quadratic regressions of σ_A on ln fz/u_*.

Figure 36 is a plot of σ_E versus fz/u_* for stable conditions ($0.45 \leq z/L \leq 0.55$) for all levels. The regression line accounting for nearly 45 percent of the variation of σ_E with fz/u_* is

$$\sigma_E = 1.75 - 1.02 \ln fz/u_*. \qquad (17.3)$$

Figure 37 is a plot of σ_A versus fz/u_* for stable conditions ($0.45 \leq z/L \leq 0.55$). The regression line in this case accounts for only 17.2 percent of the variation of σ_A with fz/u_*. The plot seems to indicate that there is very little trend of the standard deviation of the azimuth angle with fz/u_* and appears to be nearly a constant value approximately equal to 5 degrees.

Figure 38 is a plot of σ_E versus fz/u_* for unstable conditions in the range ($-0.55 \leq z/L \leq -0.45$). The regression line accounts for only 18.4 percent of variation of σ_E with ln fz/u_*. In this case the range of values for fz/u_* is fairly small and the scatter on the plot appears to be quite large.

Figure 39 is a plot of σ_A versus ln fz/u_* for unstable conditions ($-0.55 \leq z/L \leq -0.45$). The regression line in this case accounts for 24.5 percent of variation of σ_A with ln fz/u_*. Scatter on this plot is somewhat smaller than that of the standard deviation of the elevation angle.

In conclusion, it has been found that under neutral atmospheric conditions the standard deviation of the elevation and azimuth angle of the wind is scaled quite well with the parameter fz/u_*. Under stable atmospheric conditions the relationship is not as clearly

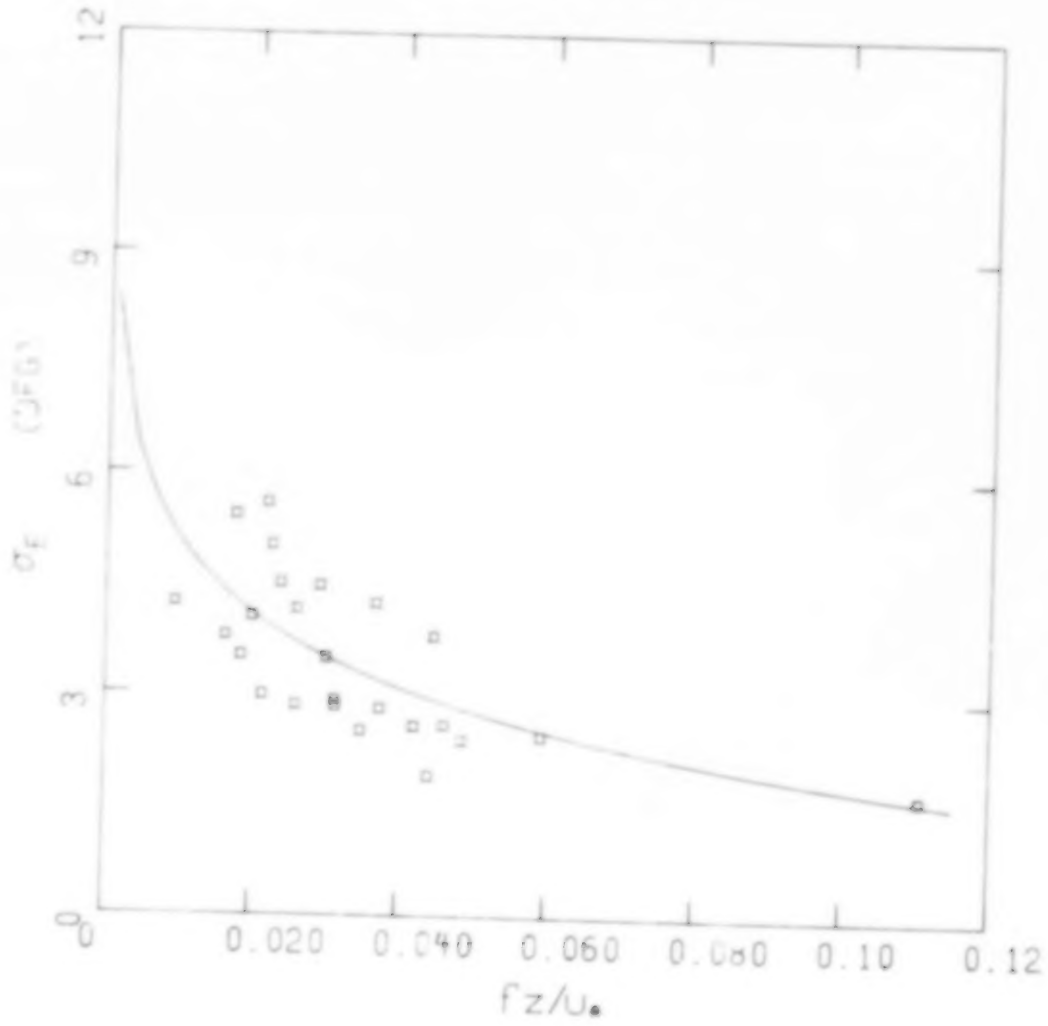

Figure 36. σ_E versus the scaling parameter, fz/u_*, for all levels (18.3 to 304.8 m) under stable conditions ($0.45 \leq z/L \leq 0.55$) defined at all levels. The solid line is a regression fit that accounts for nearly 45 percent of the variation of σ_E with ln fz/u_*.

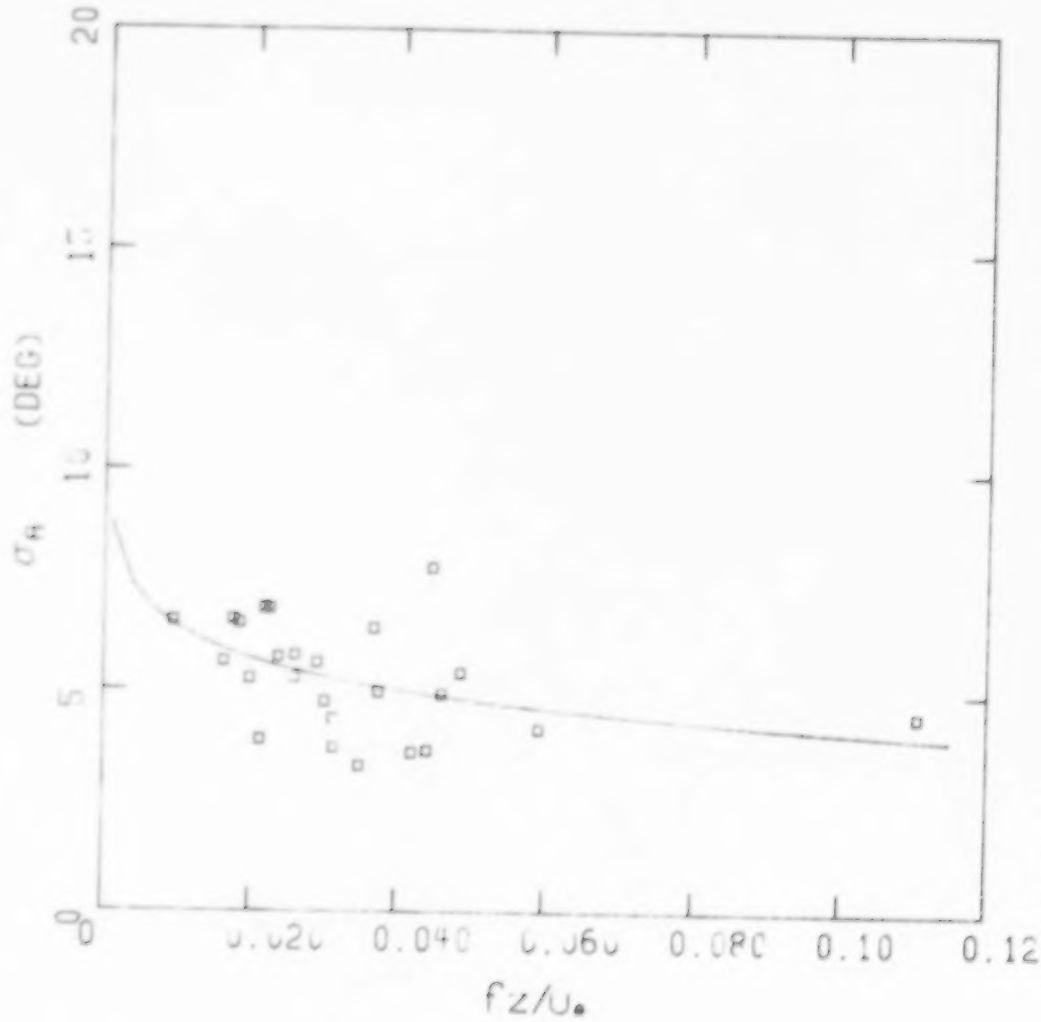

Figure 37. σ_A versus the scaling parameter, fz/u_*, for all levels (18.3 to 304.8 m) under stable conditions ($0.45 \leq z/L \leq 0.55$) defined at all levels. The solid line is a regression fit that accounts for 17 percent of the variation of σ_A with ln fz/u_*.

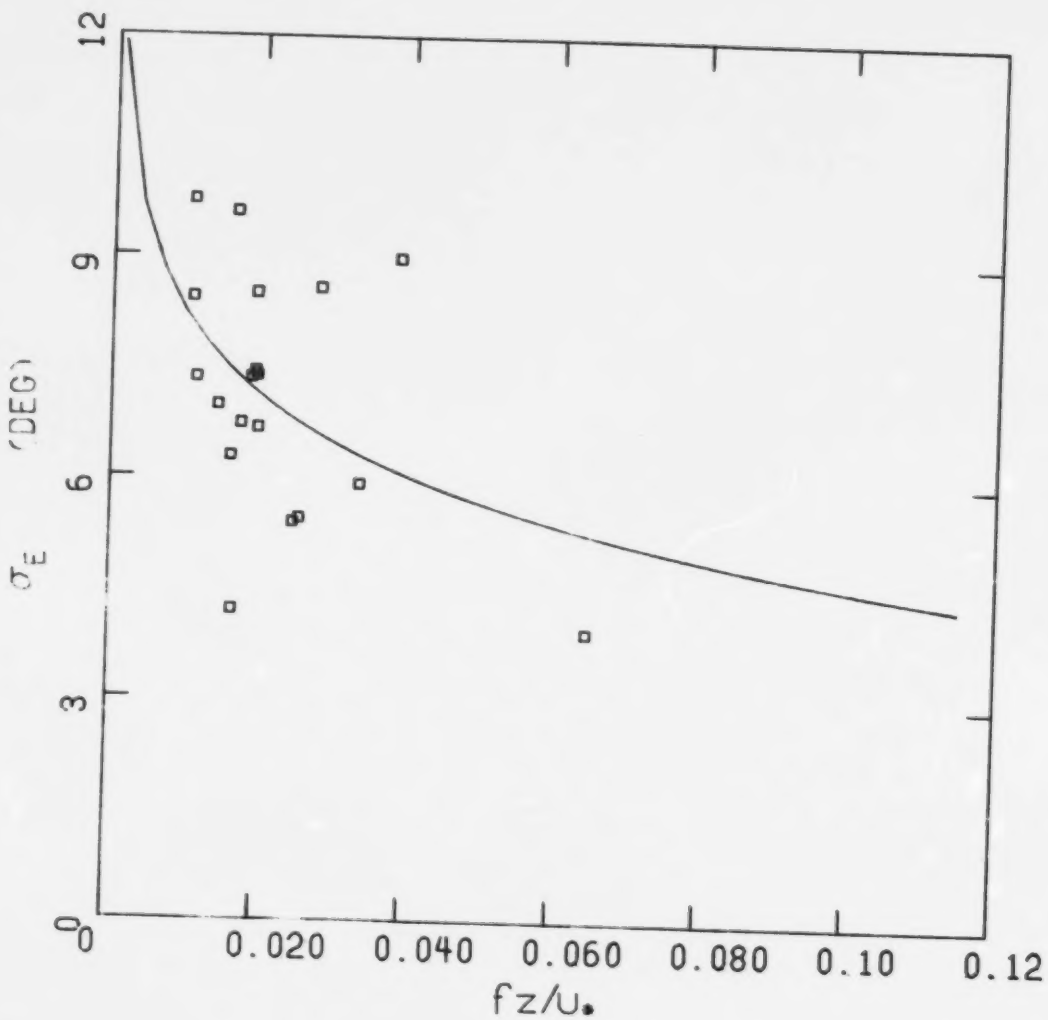

Figure 38. σ_E versus the scaling parameter, fz/u_*, for all levels (18.3 to 304.8 m) under unstable conditions ($-0.55 \leq z/L \leq -0.45$) defined at all levels. The solid line is a regression fit that accounts for 18 percent of the variation of σ_E with ln fz/u_*.

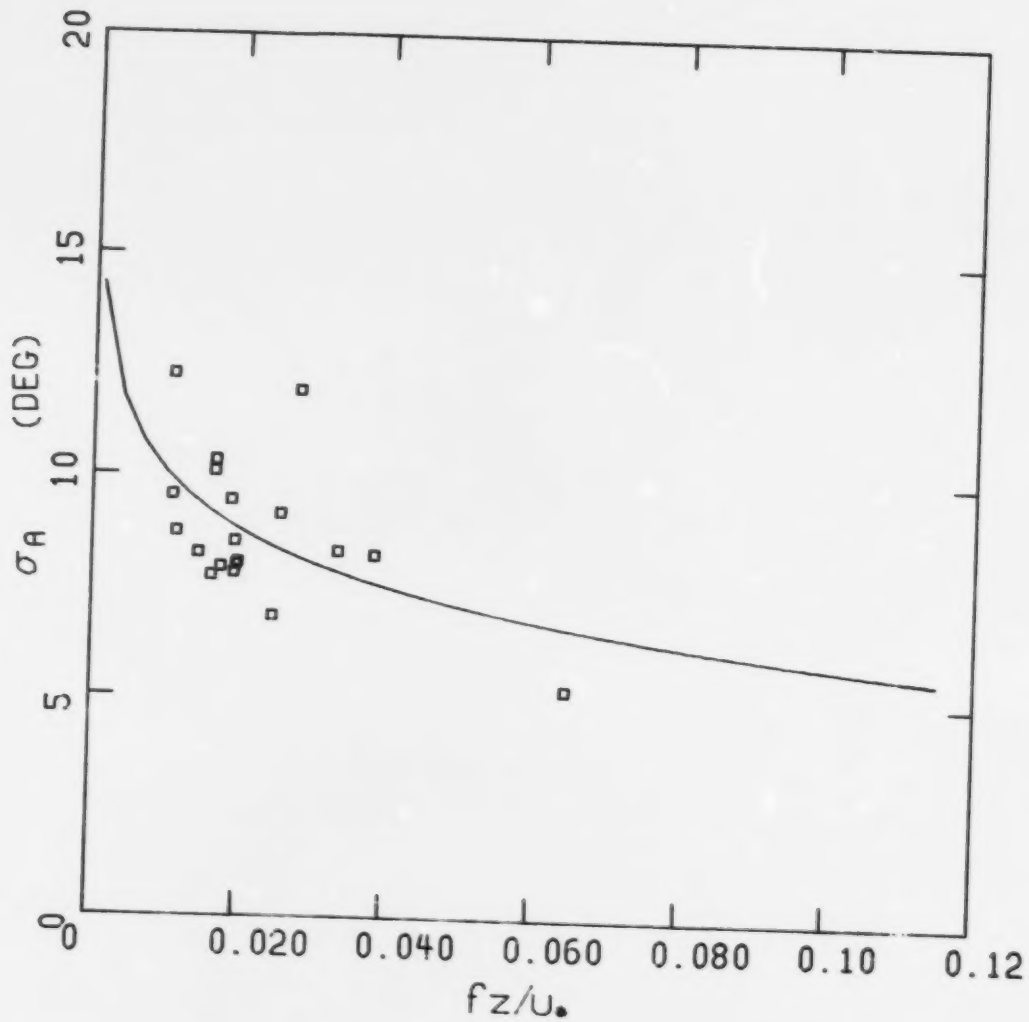

Figure 39. σ_A versus the scaling parameter, fz/u_*, for all levels (18.3 to 304.8 m) under unstable conditions ($-0.55 \leq z/L \leq -0.45$) defined at all levels. The solid line is a regression fit that accounts for 24.5 percent of the variation of σ_A with ln fz/u_*.

defined although a trend can still be seen in the σ_E relationship. The least responsiveness to this scaling parameter was generally found under unstable atmospheric conditions where there seemed to be little variation with fz/u_*. This implies that the parameter is irrelevant for these conditions as suggested by Deardorff (1970).

SECTION XVIII

EDDY VISCOSITY

The eddy viscosity, K_m, is defined by:

$$K_m = \frac{u_*^2}{\partial U/\partial z} \tag{18.1}$$

Under neutral conditions with homogeneous terrain the eddy viscosity can be expressed as:

$$K_m = u_*(z)kz \tag{18.2}$$

Using the results of Blackadar and Tennekes (1968) on the change of friction velocity with height, it can be shown that the vertical gradient of friction velocity in neutral, barotropic conditions can be expressed as:

$$\partial u_*/\partial z = -3.83 \times 10^{-4} \text{ sec}^{-1}. \tag{18.3}$$

If the above equation is integrated with respect to height and substituted back into the expression for K_m for neutral conditions one obtains:

$$K_m = u_*(0)kz - 3.83 \times 10^{-4} kz^2. \tag{18.4}$$

Eddy viscosities for neutral ($|z/L| < 0.05$) conditions were calculated from Eq. (18.1) using

$$\partial U/\partial z = \Delta U/\Delta z, \tag{18.5}$$

where ΔU was the difference in mean speeds between levels measured by the cup and bivane systems. The value Δz was the difference between levels and the derivative was assumed to apply at the mean height between levels. The friction velocity was obtained by taking the measured values at two consecutive levels, finding their mean, and squaring the result.

Figure 40 is the ensemble averaged eddy viscosity profile for neutral conditions. The solid line is the theoretical change of K_m

with height for neutral conditions using the change predicted by Blackadar and Tennekes. The average value of the friction velocity at the lower level for neutral conditions was 0.599 m/sec.

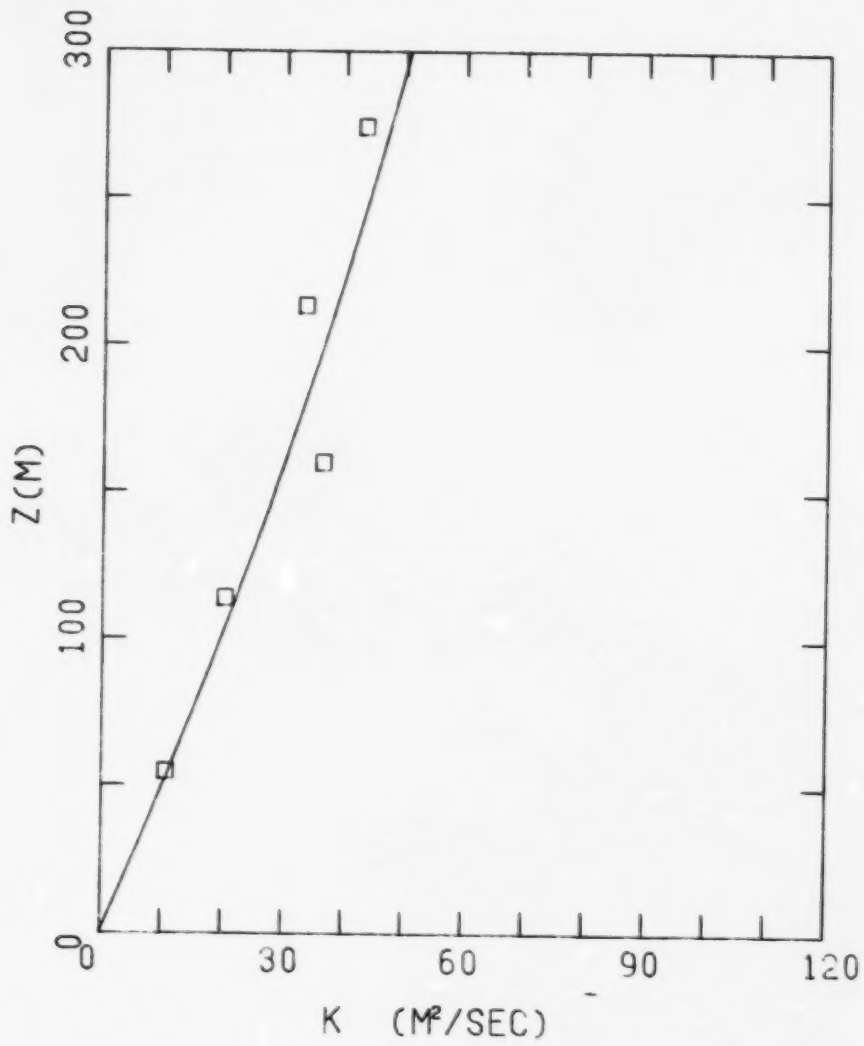

Figure 40. Eddy viscosity profile for neutral cases.

SECTION XIX

RATIO OF EDDY DIFFUSIVITIES, K_h/K_m

In the constant stress layer

$$K_h/K_m = \frac{\overline{w'\theta'}/\overline{u'w'}}{\partial\theta/\partial z}\,\frac{\partial U/\partial z}{} = \phi_m/\phi_h. \qquad (19.1)$$

It is frequently assumed that the ratio of heat and momentum diffusivities, K_h/K_m, is approximately unity in near neutral conditions. Businger et al. (1971) found that this ratio was roughly 1.35 and attributed the difference to k = 0.35 rather than the customarily accepted value of 0.4. Kitaigorodskii (1973) presented a plot containing K_h/K_m ratios from several different sources. The value near z/L = 0 appeared to be less than unity. Nickerson (1973) summarized results from various authors who found K_h/K_m ranging between 0.8 and 1.35 for near neutral stabilities.

For convenience in plotting the ratio, Panofsky has pointed out (personal communication) that it is preferable to use K_m/K_h instead of K_h/K_m, the reason being that the limiting value of the ratio as $z/L \to -\infty$ is zero. In particular, if the expressions derived by Businger et al. (1971) for ϕ_m and ϕ_h are the correct ones, the limiting values of K_m/K_h at extreme ranges of stabilities are

$$\lim_{z/L \to \infty} \phi_h/\phi_m = \lim_{z/L \to \infty} \frac{.74 + 4.7\ z/L}{1 + 4.7\ z/L} = 1.0\ , \qquad (19.2)$$

and

$$\lim_{z/L \to -\infty} \phi_h/\phi_m = \lim_{z/L \to -\infty} \frac{0.74(1 - 9\ z/L)^{-1/2}}{(1 - 15\ z/L)^{-1/4}} \to 0\ . \qquad (19.3)$$

Panofsky also points out that ϕ_h becomes indeterminate at z/L = 0. This causes considerable scatter of the data for near neutral conditions.

Figures 41 and 41a are plots of K_m/K_h vs z/L for the combined levels of 91.4 and 137.2 (Figure 41) and 182.8, 247.4, and 304.8 meters (Figure 41a). The ratios were calculated using the relationship,

$$K_m/K_h = \phi_h/\phi_m \ , \qquad (19.4)$$

where ϕ_m and ϕ_h were obtained from the regression technique. Although the scatter is large, a qualitative examination reveals that the ratios approach zero with increasing $|z/L|$ on the unstable side and seem to approach a discontinuity at $z/L = 0$. On the stable side the ratios are larger than on the unstable side and approach a value between 1 and 2 for large z/L. The large amount of scatter makes it difficult to see any height dependencies in the data.

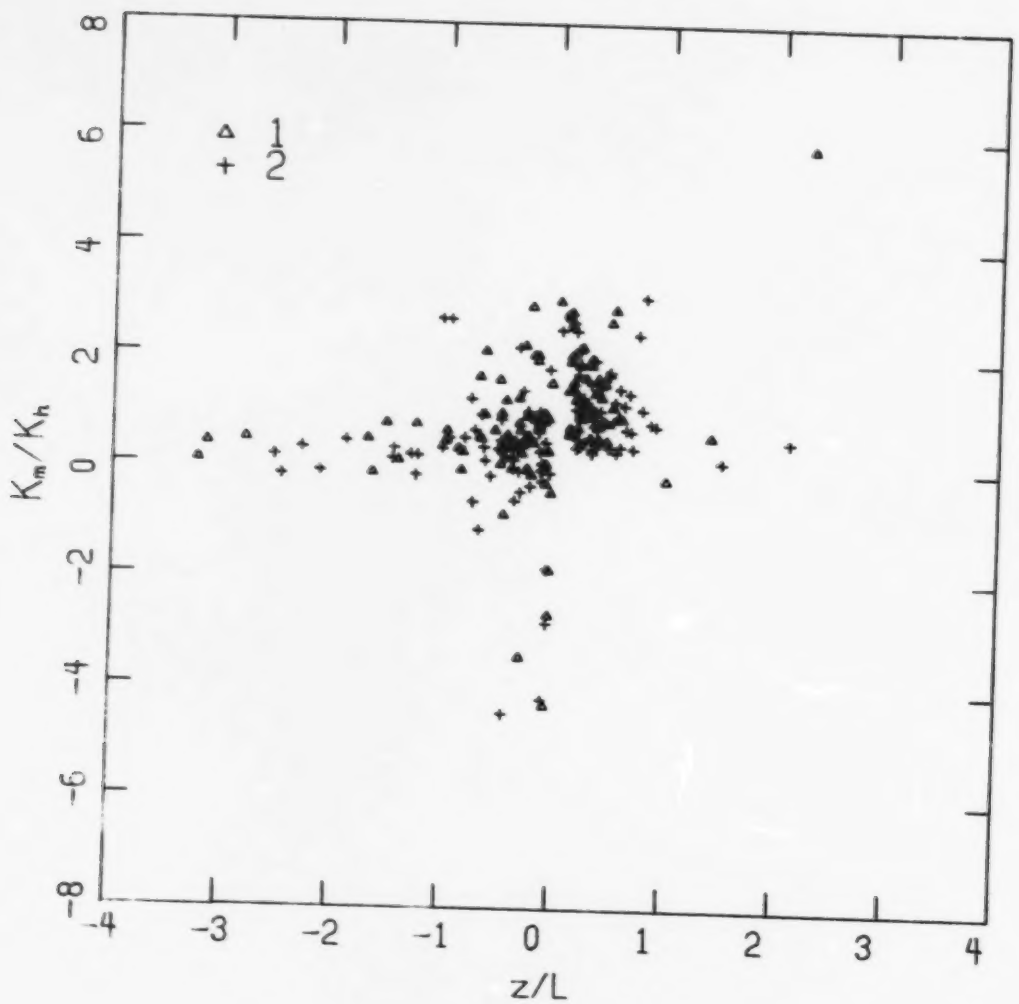

Figure 41. Ratio of momentum and heat diffusivity versus z/L (modes 1 and 2). Symbols correspond to measurement heights of 91 m (1) and 137 m (2).

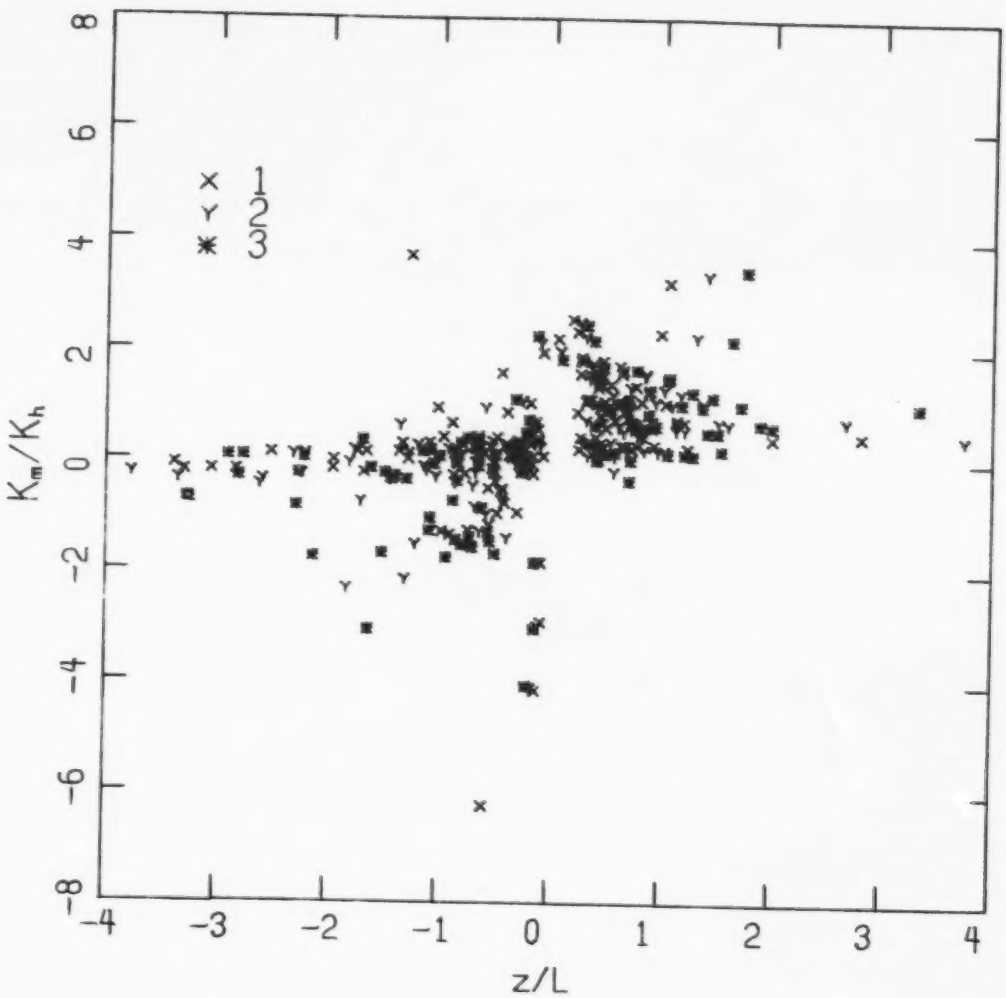

Figure 41a. Ratio of momentum and heat diffusivity versus z/L (modes 1 and 2). Symbols correspond to measurement heights of 183 m (1), 244 m (2), and 305 m (3).

SECTION XX

SPECTRAL SCALE, λ_m, OF THE VERTICAL COMPONENT AND MIXING LENGTH

Figure 42 is a vertical profile of λ_m, where λ_m is the wavelength corresponding to the maximum in the $nS_w(n)$ vs $\ln(n)$ spectrum. The peak nondimensional frequencies obtained from subjective analysis are related to λ_m, through the equations,

$$f = \frac{nz}{U} \quad \text{and} \quad \lambda_m = \frac{U}{n_m} \,, \tag{20.1}$$

where

- f is the nondimensional frequency,
- n is the frequency in (hertz),
- U is the magnitude of the mean vector wind (meters/sec)
- n_m is the frequency at the spectral maximum (hertz),
- λ_m is the wavelength (meters) corresponding to the peak.

Due to flatness of some of the spectra there was considerable scatter in the peak frequencies. The f values were determined by eye estimates of the peak in the vertical velocity spectra. In some cases aliasing made it impossible to determine the peak frequency. This involved only 27 cases out of 618 vertical velocity spectra analyzed.

The data were separated into different stability classes using z/L at 18.3 meters. The λ_m's were then averaged for each height and stability. Figure 42 shows that the results are consistent with Pasquill, 1972, for neutral, stable, and unstable conditions.

The wind profile over homogeneous terrain and neutral conditions can be obtained from:

$$\frac{dU}{dz} = u_*/\ell \ , \qquad (20.2)$$

where ℓ is the mixing length. According to Pasquill (1972), the relation between ℓ and λ_m in neutral conditions is $\ell \simeq \lambda_m/5$. Thus, by relabeling the scale on the abscissa in Figure 42, i.e., by dividing abscissa values by five one can estimate mixing lengths for neutral conditions.

Blackadar (1974) used concepts from Blackadar and Tennekes (1968) to show that the mixing length for the neutral planetary boundary layer could be functionally represented as:

$$\ell = kzF(fz/u_*) \ , \qquad (20.3)$$

where F is a universal function given by:

$$F = (1 + 63\ fz/u_*)^{-1} \ . \qquad (20.4)$$

However, Blackadar was able to obtain a better fit to the observed wind profile by using the expression:

$$\ell = 0.0063 \frac{u_*}{f} \tanh \frac{kzf}{0.0063u_*} \ . \qquad (20.5)$$

WJBF-SRL tower data was used to compute ℓ from Eqn. (20.5). The averaged profile is shown in Fig. 43. Non-neutral stability classes are shown for interest only. The estimates of mixing length by Eqn. (20.5) are smaller than those by Pasquill's $\lambda_m/5$ estimates.

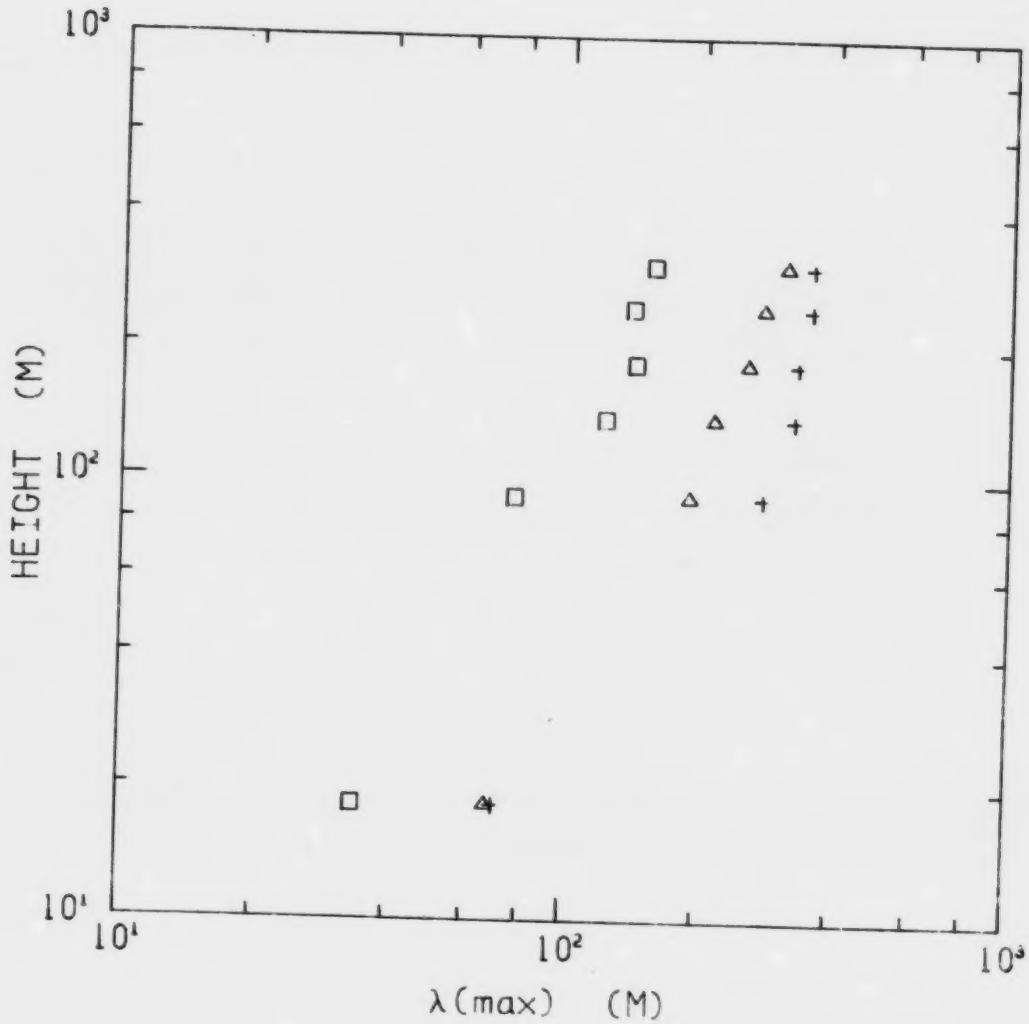

Figure 42. Vertical profile of the mean wavelength of the maximum of the vertical velocity spectra. Squares, triangles, and crosses are stable, neutral, and unstable cases, respectively.

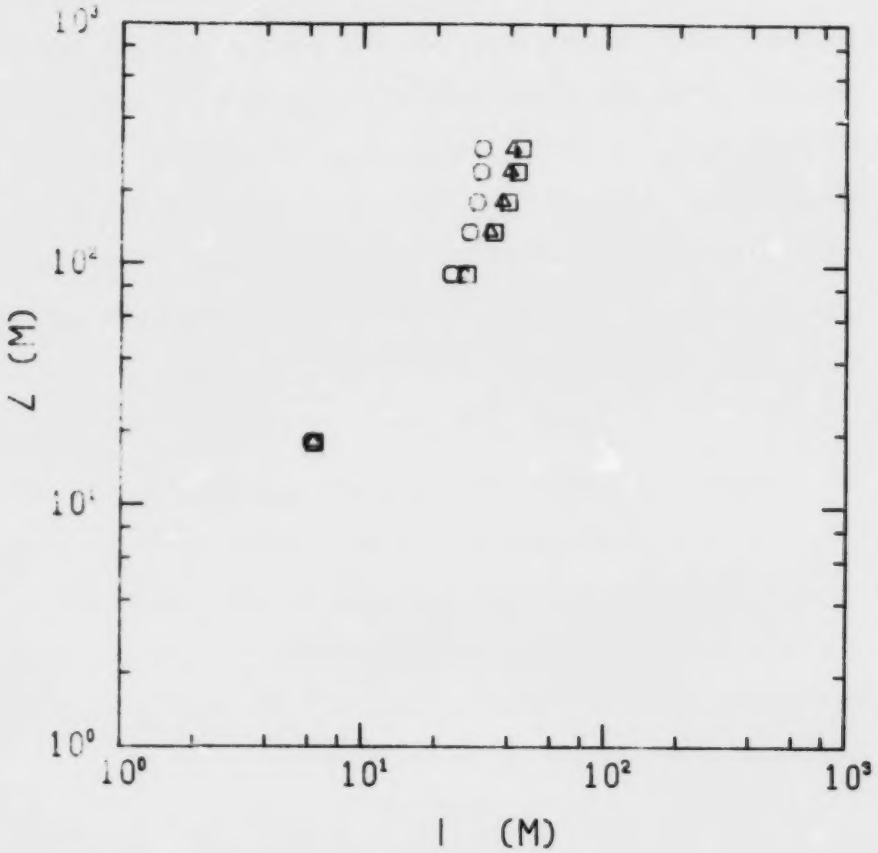

Figure 43. Mixing length profile for Blackadar's interpolation formula. Triangles, squares and octagons are unstable, neutral and stable cases, respectively.

SECTION XXI

SPECTRAL RATIOS

According to Kolmogorov's hypothesis all turbulent motions with sufficiently high Reynolds number possess local isotropy in the high frequency end of the spectrum. In this locally isotropic region, the turbulent properties of the fluid are determined by viscosity, ν, and dissipation, ε. At the low frequency end of the local isotropy range, viscosity has little effect on the power spectral density function, F(K). This region is called the inertial subrange. Therefore, in the inertial subrange, the power spectral density function is related to dissipation and wave number in the following manner:

$$F(K) = C\varepsilon^{2/3} K^{-5/3}. \qquad (21.1)$$

A theoretical result of Kolmogorov's hypothesis is that the constant for the v and w components of the one dimensional power spectral density function is equal to 4/3 of that for the u component.

As a consequence of Taylor's hypothesis, the inertial subrange power spectral density function (PSDF) can also be written in terms of frequency (Hertz). It can be shown that

$$nS(n) = KS(K) = C_1\varepsilon^{2/3} K^{-2/3} = C_2\varepsilon^{2/3} \left(\frac{n}{U}\right)^{-2/3}, \qquad (21.2)$$

so that, plotting spectra versus frequency on a log-log plot, causes the inertial subrange portion of the spectra to be indicated by a -2/3 slope. In order to confirm that local isotropy exists in this expected inertial subrange, the ratios of the v spectra to the u spectra, and of the w spectra to the u spectra, should yield a value of 4/3. In fact, confirmation of isotropy at high frequencies in the first 20 meters has been somewhat scarce. The 4/3 ratio between inertial subrange

spectral levels of the v and u components was not found in earlier experiments (Kaimal et al., 1972). A trend toward the 4/3 ratio in the Round Hill data was noted by Busch and Panofsky (1968). More recently, Kaimal et al. (1972) found good agreement with the 4/3 prediction for all but the most stable cases for dimensionless frequencies greater than one. Busch (1973) found that the frequency range in which the 4/3 ratio is obtained is shorter than the range where -5/3 slope is obtained. The conclusion is that isotropy exists only over the shorter of these two ranges. This has generally been found by those who have investigated. In fact, many times the -5/3 slope has been found while at the same time the required 4/3 spectral ratios have not. This is significant, since much of the theory concerning atmospheric turbulence is based upon the assumption of the existence of an inertial subrange and, therefore, of local isotropy at the high frequency end of the spectrum.

To determine whether the sonic spectra confirmed the existence of isotropy at the high frequency end of the spectrum and, therefore, the existence of an inertial subrange (this also requires a -2/3 slope for the logarithmic spectra), the ratios, $S_w(n)/S_u(n)$ and $S_v(n)/S_u(n)$, were calculated and plotted against nondimensional frequency, f, with the expectation that any trends in the ratios toward 4/3 could be detected. The plots contain symbols which identify each set of ratios with a particular z/L range. The nondimensional frequency, f, represents the abscissa and the spectral ratio is the ordinate. The magnitude of the mean vector wind, U, used in determining f ranged between 2.5 and 6.5 meters per second for this set of spectra. The ratios

were plotted using a semilog plot and again using a logarithmic plot. The linear scale was used to present a more graphic display of the amount of scatter.

Figure 44 is a plot of $S_w(n)/S_u(n)$ versus f. No systematic changes due to stability differences can be detected. This is probably due to the small range of stabilities used. Although there is considerable scatter in this plot, the ratios can be seen to approach 4/3 near f = 1. A realistic display of the scatter in the plot can be seen in Figure 45 An average of $S_w(n)/S_u(n)$ for f greater than 1, yielded a value of 1.23.

The ratio, $S_v(n)/S_u(n)$, is plotted in Figure 46. Kaimal *et al.* (1972) found that $S_v(n)/S_u(n)$ approached the 4/3 ratio at lower values of frequency than $S_w(n)/S_u(n)$ and this tendency can be seen on Figure 46 as well. The ratios on this plot appear to approach and nearly reach the 4/3 line around a nondimensional frequency of 0.5. The mean value of the ratios for frequencies greater than 1.0 is 1.27 with a variance of 0.07. As with the previous plot, there does not appear to be any systematic changes with z/L between the various spectra. This is probably because the range of z/L values is small. Figure 47 is a plot of $S_v(n)/S_u(n)$ versus f with a linearly scaled ordinate which emphasizes the amount of scatter.

In summary, it has been shown that the spectral ratios ($S_w(n)/S_u(n)$ and $S_v(n)/S_u(n)$) obtained from the one dimensional atmospheric turbulence velocity spectra computed from velocity fluctuations, which were measured on a sonic anemometer at a height of 18.3 meters under conditions of near neutral stability, exhibit a distinct trend towards the 4/3 ratio that should be expected at the nigh frequency end of the

spectrum if local isotropy and therefore the inertial subrange exists. The results displayed here are in general agreement with those of Kaimal et al. (1972) for a comparative stability range.

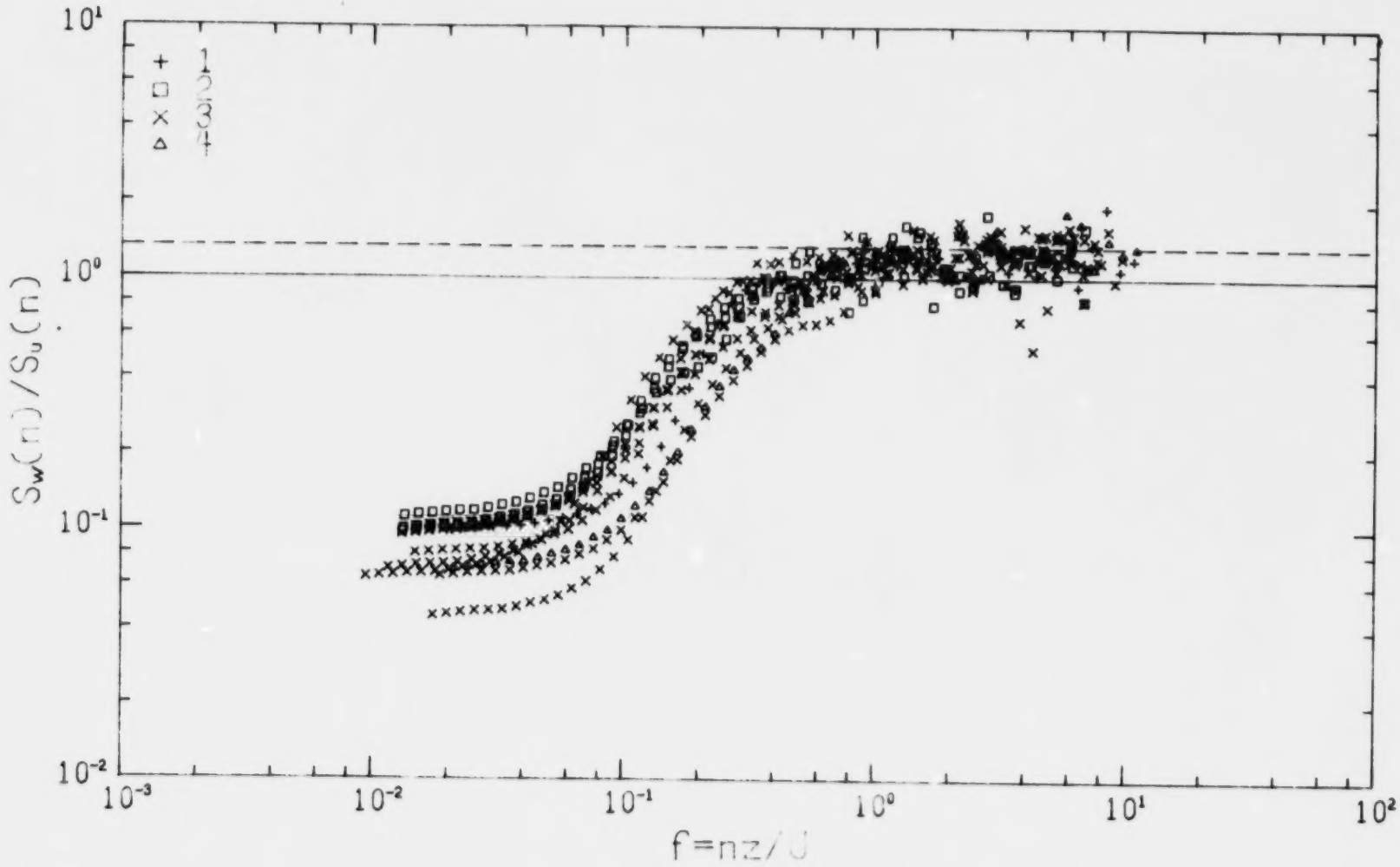

Figure 44. Ratio of w spectra to u spectra versus nondimensional frequency using logarithmic ordinate. Dashed line indicates an ordinate value of 4/3. Symbols designate ratios corresponding to the following z/L values: 1 - (z/L = -0.305), 2 - (-0.196 ≤ z/L ≤ -0.190), 3 - (-0.096 ≤ z/L ≤ 0.053), 4 - (z/L = 0.103).

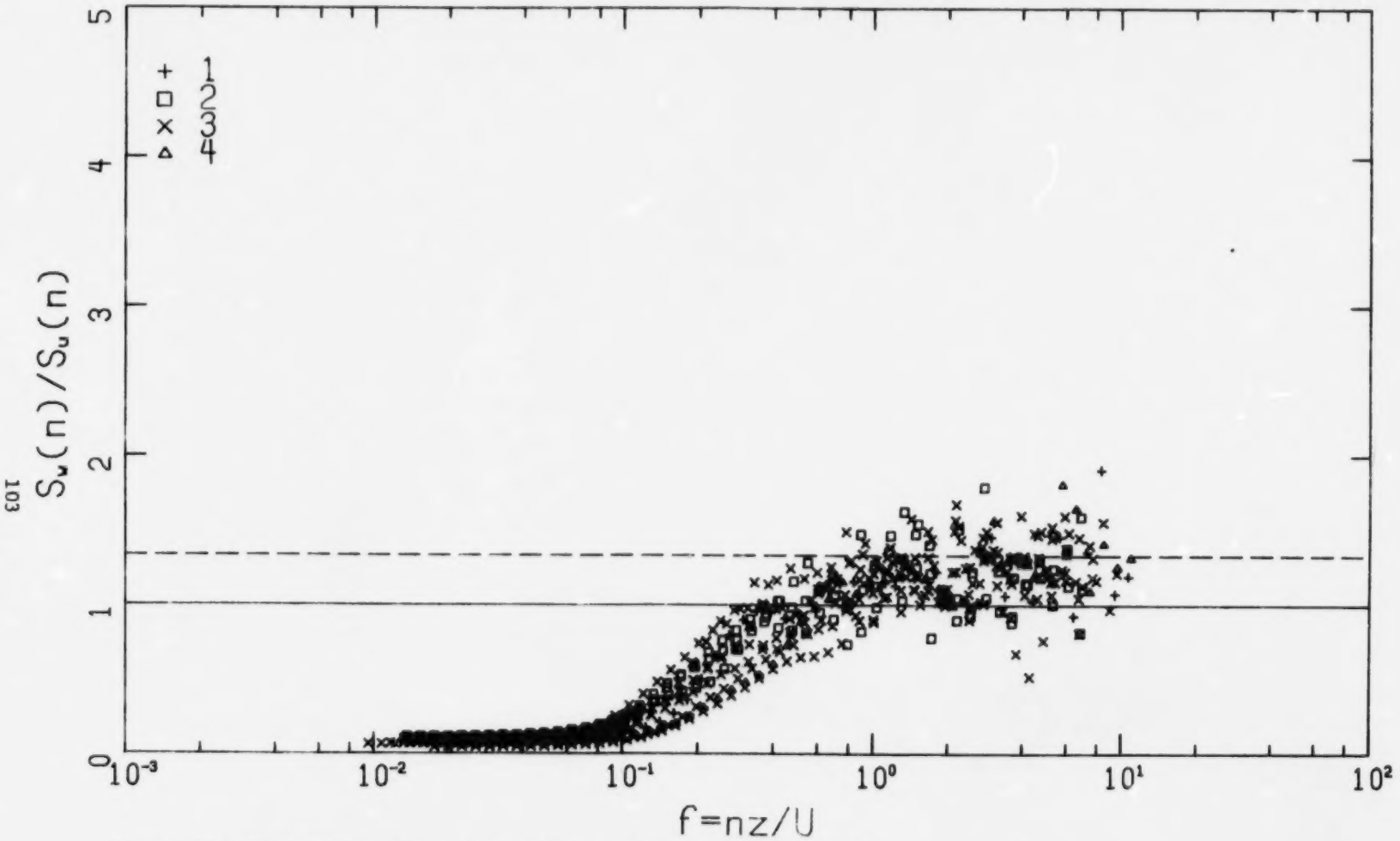

Figure 45. Ratio of w spectra to u spectra versus nondimensional frequency using linear ordinate. Dashed line indicates an ordinate value of 4/3. Symbols designate ratios corresponding to the following z/L values: 1 - (z/L = -0.305), 2 - (-0.196 ≤ z/L ≤ -0.190), 3 - (-0.096 ≤ z/L ≤ 0.053), 4 - (z/L = 0.103).

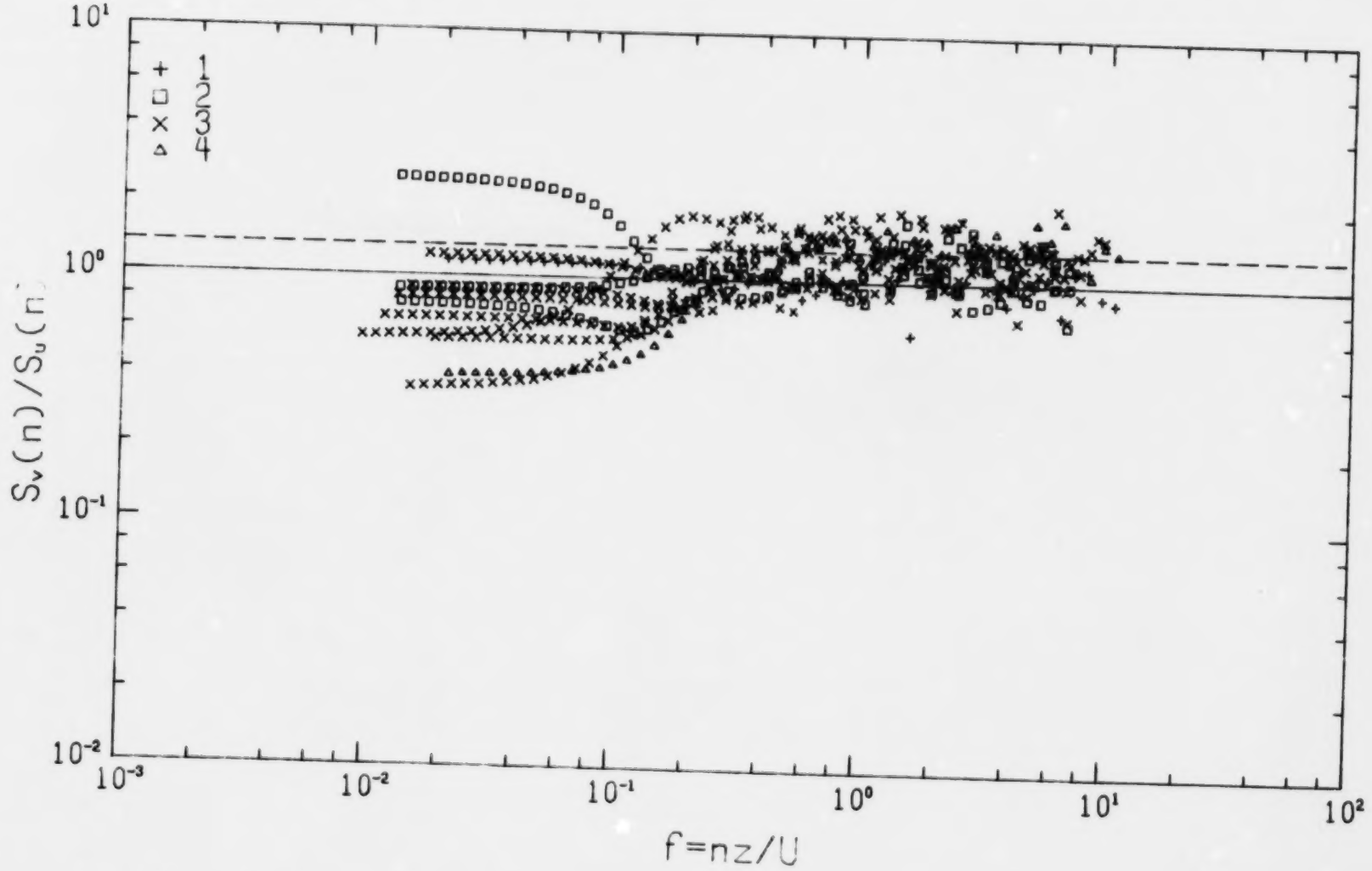

Figure 46. Ratio of v spectra to u spectra versus nondimensional frequency using logarithmic ordinate. Dashed line indicates an ordinate value of 4/3. Symbols designate ratios corresponding to the following z/L values: 1 - (z/L = -0.305), 2 - (-0.196 ≤ z/L ≤ -0.190), 3 - (-0.096 ≤ z/L ≤ 0.053), 4 - (z/L = 0.103).

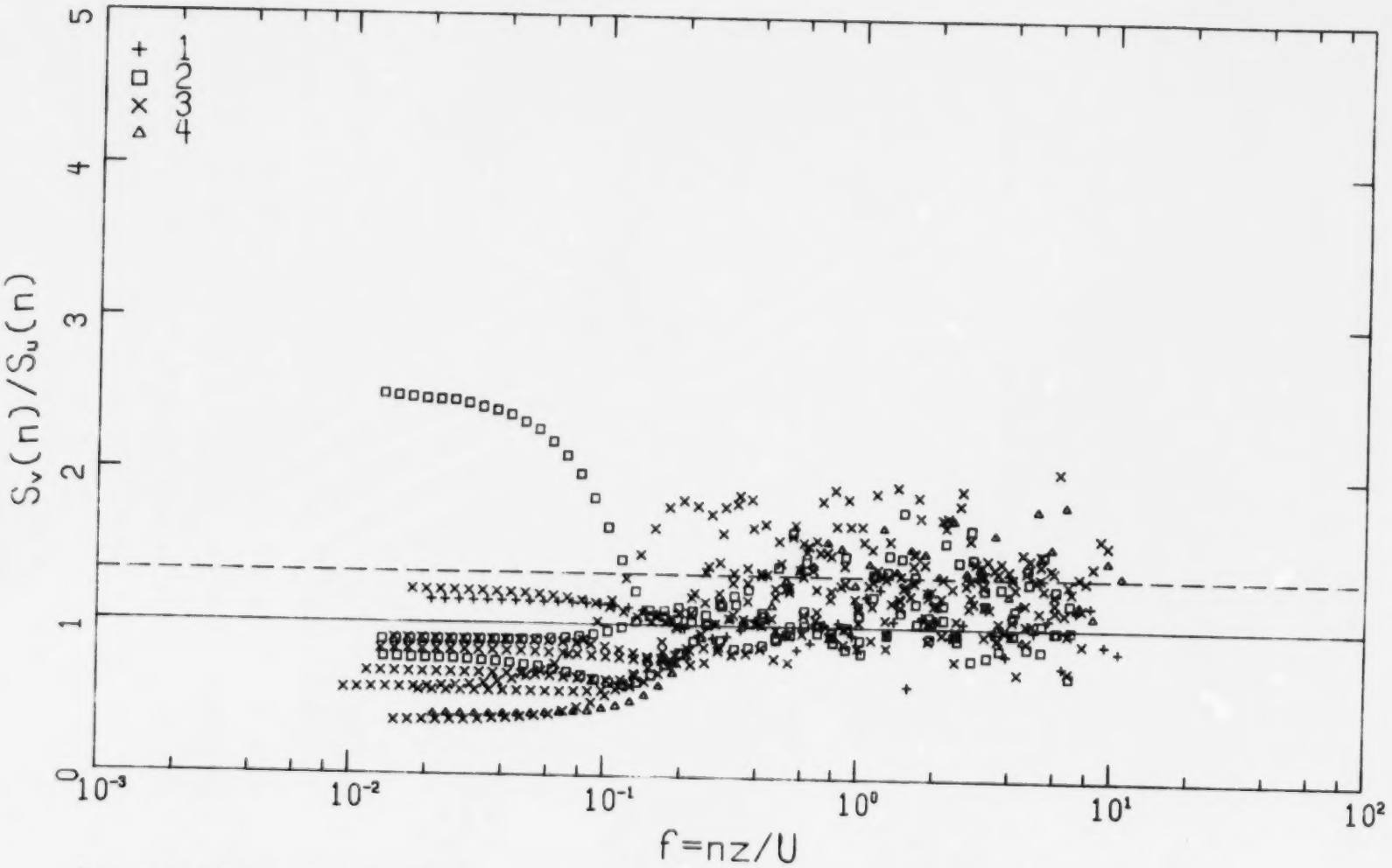

Figure 47. Ratio of v spectra to u spectra versus nondimensional frequency using linear ordinate. Dashed line indicates an ordinate value of 4/3. Symbols designate ratios corresponding to the following z/L values: 1 - (z/L = -0.305), 2 - (-0.196 ≤ z/L ≤ -0.190), 3 - (-0.096 ≤ z/L ≤ 0.053), 4 - (z/L = 0.103).

SECTION XXII

NORMALIZED TURBULENCE VELOCITY SPECTRA

Atmospheric turbulence velocity spectra were analyzed and plotted using a procedure which was used by Kaimal et al. (1972) in which the spectra were collapsed into universal curves in the inertial subrange. The spectral behavior at the lower frequencies were then observed as a function of z/L.

The inertial subrange one-dimensional velocity spectra normalized with u_*^2 (surface stress) can be written in the form,

$$\frac{nS(n)}{u_*^2} = \frac{\alpha}{(2\pi k)^{2/3}} \left(\frac{kz\varepsilon}{u_*^3}\right)^{2/3} \left(\frac{nz}{U}\right)^{-2/3} , \tag{22.1}$$

where

$$\frac{nz}{U} \equiv f , \tag{22.2}$$

$$\frac{kz\varepsilon}{u_*^3} \equiv \phi_\varepsilon , \text{ and} \tag{22.3}$$

$\alpha \equiv \alpha_1$, α_2, or α_3 depending upon the component of velocity, u, v, or w, respectively, being used.

The normalized velocity spectra rewritten in this notation become

$$\frac{nS(n)}{u_*^2} = \frac{\alpha}{(2\pi k)^{2/3}} \phi_\varepsilon^{2/3} f^{-2/3} . \tag{22.4}$$

The only parameter on the right that is dependent upon z/L is ϕ_ε. Dividing both sides of the equation by $\phi_\varepsilon^{2/3}$ results in an equation which is a function of the nondimensional frequency only. Normalizing the velocity spectra in this manner effectively removes the z/L dependence from the equations for the inertial subrange portion of the spectrum. This brings all spectra, regardless of stability, into

coincidence in the inertial subrange. The differences between these spectra at the low frequency end of the spectrum outside of the inertial subrange can then be attributed to z/L differences. It should be noted that, although u_*^2 appears in the normalization term, applying the definition of $\phi_\varepsilon^{2/3}$ results in cancelling the u_*^2 term leaving $(kz\varepsilon)^{2/3}$ as the normalizing factor.

Figure 48 is a plot of the w spectra versus nondimensional frequency where the spectra have been normalized using the method described above. Each individual spectrum is shown with a different symbol corresponding to a z/L value. This method of normalization seems to give reasonable results. The spectra have collapsed in the inertial subrange and exhibit a slope very nearly equal to -2/3. As indicated in Section XXI on spectral ratios, the inertial subrange can be expected to begin near a nondimensional frequency of one. There are 13 sets of spectra on this plot with stabilities in the range ($-0.3 \leq z/L \leq 0.1$). The two most stable spectra are arranged according to z/L at the low frequency end of the spectrum but the third stable spectrum, which is very near neutral (z/L = .0006) lies among the main group of unstable spectra. The unstable spectra do not seem to exhibit any particular trend with decreasing stability. A spectral maximum representative of the full range of stabilities plotted appears to be near 0.4 for f and 0.4 to 0.5 for the magnitude of the normalized spectra. These results are generally consistent with those from the 1968 Kansas experiment (Kaimal et al., 1972) for an equivalent stability range.

Figure 49 is a plot of the normalized spectra for the v component of the velocity. Again, as in Figure 48, the spectra collapse in the

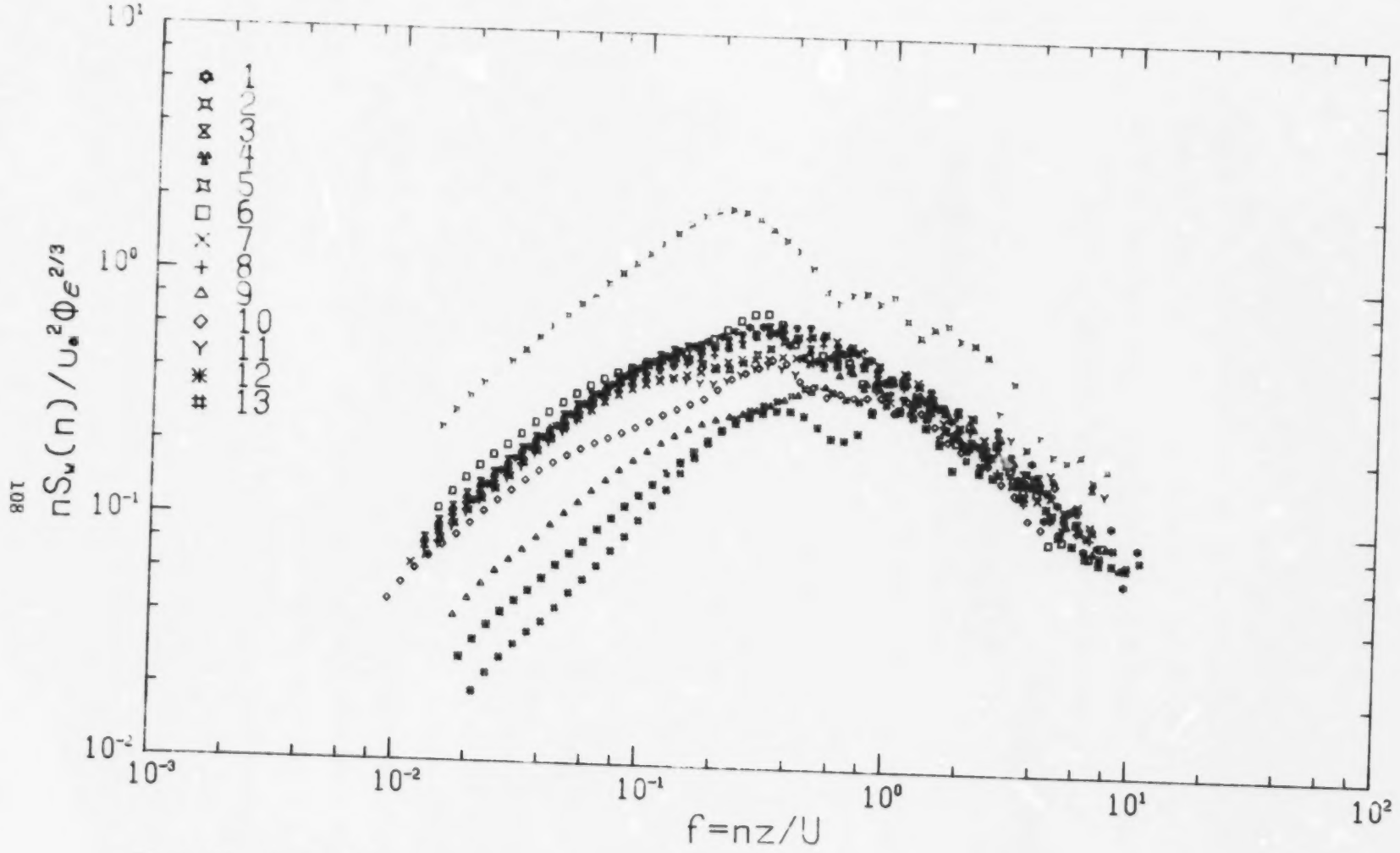

Figure 48. Normalized w spectra versus nondimensional frequency. Symbols designate spectra corresponding to the following z/L values: 1 - (-0.305), 2 - (-0.251), 3 - (-0.196), 4 - (-0.136), 5 - (-0.109), 6 - (-0.096), 7 - (-0.065), 8 - (-0.063), 9 - (-0.042), 10 - (-0.020), 11 - (0.0006), 12 - (0.053), and 13 - (0.103).

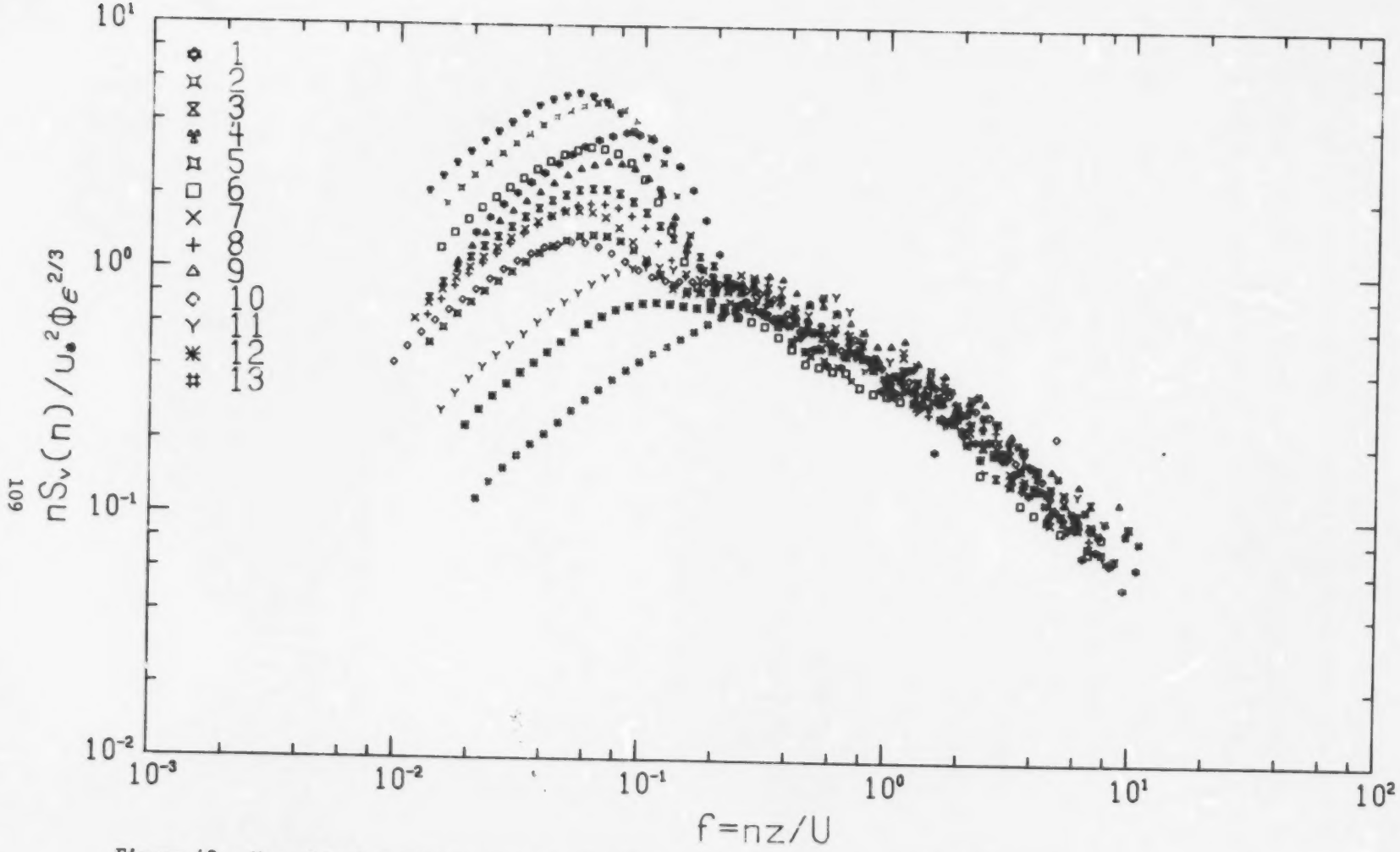

Figure 49. Normalized v spectra versus nondimensional frequency. Symbols designate spectra corresponding to the following z/L values: 1 - (-0.305), 2 - (-0.251), 3 - (-0.196), 4 - (-0.136), 5 - (-0.109), 6 - (-0.096), 7 - (-0.065), 8 - (-0.063), 9 - (-0.042), 10 - (-0.020), 11 - (0.0006), 12 - (0.053), and 13 - (0.103).

inertial subrange and a slope of -2/3 is observed. The stable spectra are arranged according to z/L. Of particular interest is the separation between the areas occupied by the stable and unstable spectra as though the spectra were excluded from this region. Kaimal et al. (1972) noted a similar property in the v component of the normalized spectra. This seems to indicate a sudden shift in the predominant scale of motion as z/L changes sign. The unstable spectra do not display any systematic changes with z/L and tend to be randomly clustered. A spectral peak representative of the stable spectra exists at approximately 0.7 and corresponds to a nondimensional frequency near 0.2. This value is to be compared with a peak value of 0.5 and a nondimensional frequency of 0.25 obtained in the 1968 Kansas experiment. The spectral peak for the unstable side which represents a z/L range of 0 to -0.3 falls between 1 and 5 and corresponds to a range of frequencies between 0.05 and 0.09.

Figure 50 is a plot of the normalized logarithmic u spectra. As with the w and v spectra, these exhibit the collapsing in the inertial subrange and also some progression with stability at the low frequency end of the spectrum for positive z/L values. The unstable spectra do not reveal a progression with z/L but appear to be clustered in a random fashion. A stable spectral peak of 1 to 1.5 is observed near a nondimensional frequency of approximately 0.1. The spectral peaks corresponding to the unstable range of z/L lie between 2 and 4 in a nondimensional frequency range of .05 to .08. These results compare favorably with those presented by Kaimal et al. (1972).

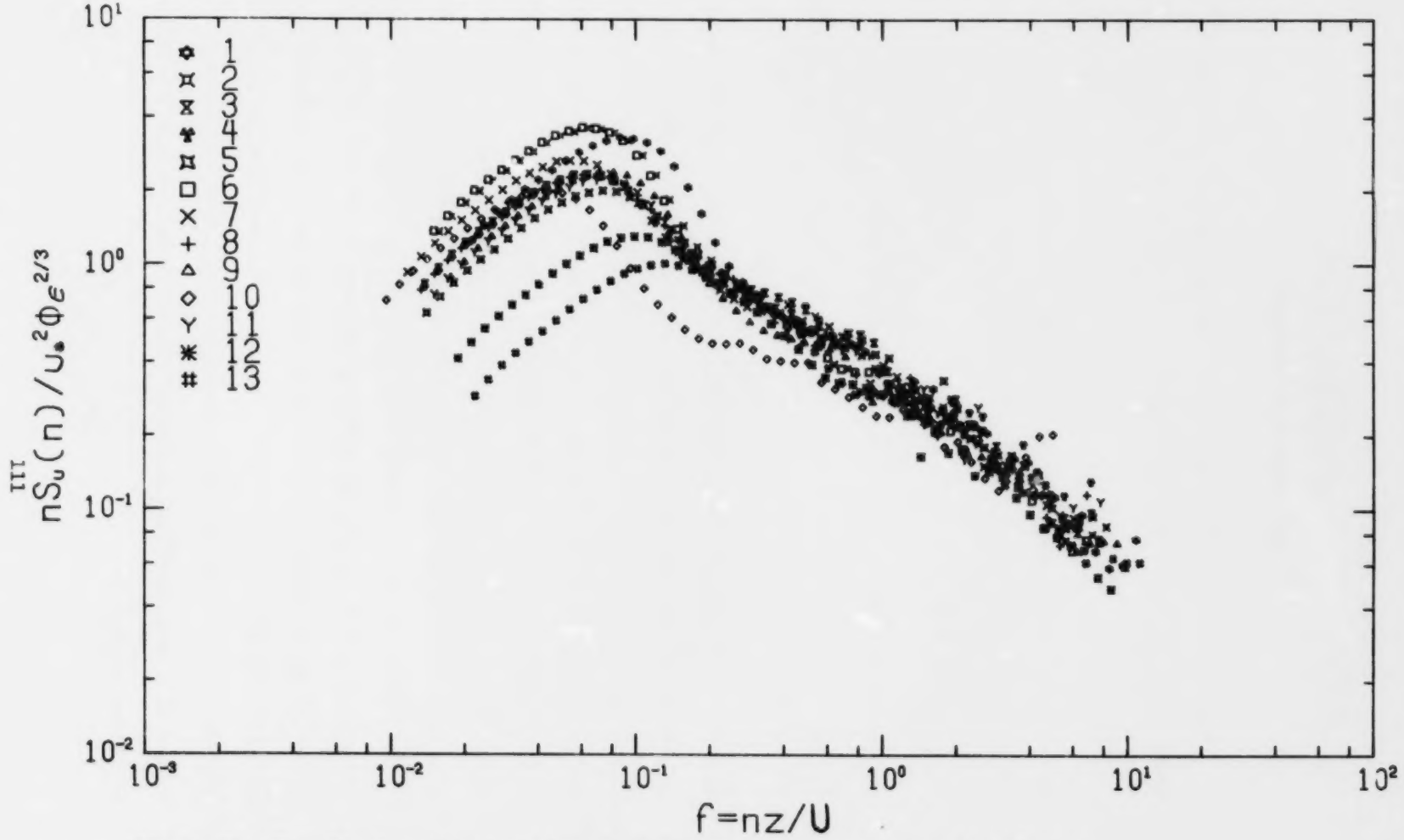

Figure 50. Normalized u spectra versus nondimensional frequency. Symbols designate spectra corresponding to the following z/L values: 1 - (-0.305), 2 - (-0.251), 3 - (-0.196), 4 - (-0.136), 5 - (-0.109), 6 - (-0.096), 7 - (-0.065), 8 - (-0.063), 9 - (-0.042), 10 - (-0.020), 11 - (0.0006), 12 - (0.053), and 13 - (0.103).

SECTION XXIII

THE KOLMOGOROV CONSTANT

The logarithmic u spectra for the inertial subrange in terms of frequency in Hertz can be expressed as

$$nS_u(n) = \alpha_1 \frac{2\pi n}{U} \varepsilon^{2/3} \left(\frac{2\pi n}{U}\right)^{-5/3} . \qquad (23.1)$$

Under conditions of steady state, horizontal uniformity, and neutral atmospheric stability, the dissipation is generally assumed to be

$$\varepsilon = \frac{u_*^3}{kz} . \qquad (23.2)$$

Thus the logarithmic u spectra for the inertial subrange can be rewritten as

$$nS_u(n) = \frac{\alpha_1}{(2\pi)^{2/3}} \frac{u_*^2}{k^{2/3}} f^{-2/3} . \qquad (23.3)$$

From the above equation it is apparent that determination of the value of the Kolmogorov constant depends upon the value assumed for the von Karman constant. In order to examine the relationship between these two constants, six sonic u spectra corresponding to near neutral stability were used. Selected inertial subrange u spectra values corresponding to nondimensional frequencies greater than 1 were required to correspond to a point where $S_w(n)/S_u(n)$ and $S_v(n)/S_u(n)$ were both near 4/3 in value. Table 13 lists the set of u spectra values that were used along with the corresponding nondimensional frequency and time of observation. Also listed is the u_* corresponding to each spectrum and a term labeled "factor" (defined in the table). The factor for each time period was calculated and the average value was determined. Three different values of k were then used to estimate three values for α_1. The results are shown in Table 14.

Table 13. PARAMETERS USED TO CALCULATE α_1 AS A FUNCTION OF k.

Time	z/L	f	$nS_u(n)$	u_*	Factor
139 1235	-0.110	3.14116	0.02405	0.66405	0.48450
139 1355	-0.048	4.20622	0.02976	0.42556	1.63002
139 1555	-0.072	4.08560	0.02860	0.57572	1.06410
140 1740	0.001	4.07796	0.02789	0.58587	0.86167
140 1820	0.060	3.06275	0.03129	0.38838	1.84713
144 1334	-0.022	1.20109	0.19433	1.01300	1.00473

$$\alpha_1 = \left[\frac{(2\pi f)^{2/3}\, nS_u(n)}{u_*^2}\right] k^{2/3}$$ where the bracketed term represents "factor".

Mean Factor = 0.92195, Stnd. Error, Factor = 0.44655

Table 14. VALUES OF α_1 CORRESPONDING TO SELECTED VALUES OF k.

k	α_1	α_1 Stnd. Error
0.35	0.458	0.222
0.40	0.501	0.242
0.44	0.533	0.238

Frenzen (1973) in his investigations of Kolmogorov-von Karman products found that for k = 0.393, α_1 = 0.50. Kaimal et al. (1972) showed that α_1 was 0.50 ±0.05. Boston (1970) obtained a value of 0.51 for α_1. The result presented in this investigation of α_1 = 0.50 which corresponds to a von Karman constant of 0.40 is in general agreement with those cited above. Others have found values of α_1 ranging from 0.53 (Wyngaard and Pao, 1972) to 0.69 (Gibson et al., 1970).

SECTION XXIV

ENERGY BUDGET THEORY AND DISSIPATION OF TURBULENCE ENERGY

In high Reynolds number atmospheric turbulence, the budget of turbulent kinetic energy per unit mass is expressed (Lumley and Panofsky, 1964):

$$\frac{1}{2}\frac{\partial}{\partial t}(\overline{u_i'u_i'}) + \frac{U_j}{2}\frac{\partial}{\partial x_j}(\overline{u_i'u_i'}) + \overline{u_i'u_j'}\frac{\partial U_i}{\partial x_j} - \frac{g}{\theta}\overline{u_3'\theta'}$$

$$+ \frac{1}{2}\frac{\partial}{\partial x_j}(\overline{u_i'u_i'u_j'}) + \nu\overline{\frac{\partial u_i'}{\partial x_j}\frac{\partial u_i'}{\partial x_j}} + \frac{1}{\rho}\overline{\frac{\partial p'u_i'}{\partial x_i}} = 0. \quad (24.1)$$

In the above expression, the primes designate fluctuating parts and the unprimed terms represent the mean parts of the velocity in the x_i direction. Repeated indices are summed. The overbar designates a time average.

Assuming horizontal homogeneity and steady-state conditions and taking the coordinate system so that the x-axis lies parallel to the mean vector wind, results in the much simplified energy budget equation:

$$\overline{u'w'}\frac{\partial U}{\partial z} - \frac{g}{\theta}\overline{w'\theta'} + \frac{1}{2}\frac{\partial}{\partial z}[\overline{(u'u' + v'v' + w'w')w'}]$$

$$+ \nu[\overline{(\frac{\partial u'}{\partial z})^2} + \overline{(\frac{\partial v'}{\partial z})^2} + \overline{(\frac{\partial w'}{\partial z})^2}] + \frac{1}{\rho}\overline{\frac{\partial p'w'}{\partial z}} = 0, \quad (24.2)$$

and after further simplification:

$$\overline{u'w'}\frac{\partial U}{\partial z} - \frac{g}{\theta}\overline{w'\theta'} + \frac{1}{2}\overline{\frac{\partial w'q^2}{\partial z}} + \varepsilon + \frac{1}{\rho}\overline{\frac{\partial p'w'}{\partial z}} = 0. \quad (24.3)$$

The terrain surrounding the tower where the turbulence statistics were obtained for this experiment cast serious doubt upon the assumption of horizontal homogeneity used to simplify the energy budget equation.

The error due to this assumption will be combined with the $\frac{1}{\rho}\frac{\partial\overline{p'w'}}{\partial z}$ term and be designated, I, (Wyngaard and Coté, 1971) for whatever imbalance may exist as a result of these assumptions and unmeasured terms.

Multiplying the equation by kz/u_*^3 results in the nondimensional equation:

$$-\frac{kz}{u_*}\frac{\partial U}{\partial z} - \frac{g}{\theta_o}\overline{w'\theta'}\frac{kz}{u_*^3} + \frac{kz}{u_*^3}\frac{\partial(\overline{w'q^2/2})}{\partial z} + \frac{kz\varepsilon}{u_*^3} + \frac{kzI}{u_*^3} = 0, \tag{24.4}$$

where

$$-\overline{u'w'} \simeq u_*^2 = \tau/\rho. \tag{24.5}$$

This approximation is generally made based upon the assumption that the term, $-\overline{v'w'}$, is small.

The first term is called nondimensional wind shear and is designated

$$\phi_m = \frac{kz}{u_*}\frac{\partial U}{\partial z}. \tag{24.6}$$

The second term represents the nondimensional form of the buoyant production of turbulent energy. It is designated

$$z/L = \frac{z}{\left(\frac{-u_*^3}{kg/\theta_o\,\overline{w'\theta'}}\right)}. \tag{24.7}$$

The third term represents the divergence of the vertical flux of kinetic energy or turbulent transport. It is designated

$$\phi_D = \frac{kz}{u_*^3}\frac{\partial(\overline{w'q^2/2})}{\partial z}. \tag{24.8}$$

The fourth term is the nondimensionalized form of dissipation designated:

$$\phi_\varepsilon = \frac{kz\varepsilon}{u_*^3} \quad . \tag{24.9}$$

The last term is the nondimensionalized imbalance term which includes the unmeasured pressure transport term and errors.

Monin and Obukhov (1954), using methods of the theory of similitude, related the averaged characteristics of the surface layer of the atmosphere to momentum, heat, and humidity fluxes (u_*, $\overline{w'\theta'}$, $\overline{w'q_e'}$ respectively). The Monin-Obukhov similarity theory predicts that the dimensionless quantities (ϕ_m and ϕ_h) are functions of z/L in the surface layer up to a height of near 50 m. Other similarity hypotheses that have been subsequently proposed are that the quantities (ϕ_ε, σ_w/u_*, σ_v/u_*, and σ_u/u_*) are functions of z/L only in the surface layer. Many experimental results have shown that similarity theory may be followed as high as 150 m, e.g. Panofsky (1972).

Dissipation of turbulence energy, ε, was calculated from 13 sonic spectra corresponding to z/L values ranging from -0.3 to +0.1 as follows. The inertial subrange had been determined to exist at nondimensional frequencies greater than 1. This determination was based upon a -2/3 slope for the logarithmic spectra, as well as the trend for the spectral ratios to approach 4/3 with increasing frequency in accordance with Kolmogorov's hypothesis. Points within the inertial subrange were selected using criteria of spectral ratios near 4/3 while requiring that the w and v spectra be approximately equal. The logarithmic u spectra can be written in the following form:

$$nS_u(n) = [\alpha_1/(2\pi)^{2/3}] \; \varepsilon^{2/3} \; (nU)^{-2/3} \quad . \tag{24.10}$$

If Kolmogorov's constant for the u spectra is taken as 0.5, (Kaimal et al., 1972) (also see Kolmogorov Constant section) then the logarithmic u spectra can be written as

$$nS_u(n) = 0.147(\varepsilon z)^{2/3} f^{-2/3} . \qquad (24.11)$$

As a result of Kolmogorov's hypothesis the universal constants for the v and w spectra are 4/3 times the constant for the u spectra, so that

$$nS_v(n) = nS_w(n) = 0.196 (\varepsilon z)^{2/3} f^{-2/3} . \qquad (24.12)$$

These equations were solved for ε, the dissipation, after substituting the appropriate values for the logarithmic spectra, the nondimensional frequency, and the height, which was 18.3 meters. Since ε should equal the same value regardless of which component of the spectra it was derived from, the three values of dissipation which were obtained were then averaged and the resulting value was taken to represent dissipation for the particula. data time block under consideration.

Blackadar et al. (1974) found that at 30 meters and below, ε is estimated by

$$\varepsilon = \frac{2.5}{z} u_*^3 (1 - 16\ z/L)^{-1/4} \quad (z/L \leq 0) , \qquad (24.13)$$

where a value of 0.4 is being used for the von Karman constant. This expression was used to calculate ε values which were then compared with the corresponding values obtained from the sonic spectra. For $z/L \geq 0$ the expression,

$$\varepsilon = \frac{2.5}{z} u_*^3 (1 + 4.7\ z/L), \qquad (24.14)$$

was used to calculate the dissipation values for comparing with the sonic derived values of ε. Table 15 is a listing of the z/L values along with the corresponding calculated and observed dissipations.

Table 15. z/L, CALCULATED ε, AND ε FROM SONIC SPECTRA. THESE VALUES CORRESPONDING TO THE INDICATED z/L VALUES WERE PLOTTED IN FIGURE 51.

z/L	Calculated ε	Sonic Observed ε
-0.110	0.031	0.011
-0.048	0.009	0.020
-0.072	0.022	0.019
-0.074	0.033	0.027
0.001	0.028	0.018
0.060	0.010	0.017
-0.022	0.132	0.100
-0.287	0.013	0.014
-0.224	0.015	0.017
-0.155	0.019	0.018
-0.124	0.031	0.024
0.118	0.008	0.009
-0.348	0.012	0.016

The "Calculated ε" were obtained from the relation

$$\varepsilon = \frac{2.5\ u_*^3}{z}\ (1 - 16\ z/L)^{-1/4}\ ,\ z/L \leq 0$$

$$\varepsilon = \frac{2.5\ u_*^3}{z}\ (1 + 4.7\ z/L)\ ,\ z/L \geq 0.$$

A visual comparison of dissipation obtained from the two sources is shown in Figure 51. In this figure the ordinate represents observed dissipation obtained from the sonic spectra and the abscissa indicates dissipation calculated using the above two equations. The dashed line is the line along which dissipation obtained from both methods is equal. The scatter of points is centered about the dashed line indicating that the equations used to estimate ε represent a reasonable approximation for the observed values.

By making appropriate assumptions and simplifications, many authors have attempted to reduce the energy budget to fewer and more easily obtained terms. In particular, two kinds of simplification have been suggested. Lumley and Panofsky (1964) suggest that under unstable conditions as an approximate result, dissipation equals production of mechanical energy, so that

$$\phi_m = \phi_\varepsilon, \quad z/L \leq 0 . \tag{24.15}$$

It has also been suggested that the sum of buoyant and mechanical energy production is equal to dissipation,

$$\phi_m - z/L = \phi_\varepsilon, \quad z/L \leq 0 . \tag{24.16}$$

Busch and Panofsky (1968) found in checking the validity of these equations for the range, $-0.4 < z/L < 0.5$, that ϕ_ε did not vary with z/L on the unstable side. On the stable side they discovered that the line represented by

$$\phi_\varepsilon = \phi_m - z/L = 1 + 9\, z/L , \tag{24.17}$$

fits a collection of data from several different sites and heights up to 91 m. Blackadar et al. (1974) implied that for unstable conditions, dissipation was balanced by buoyant and mechanical energy production

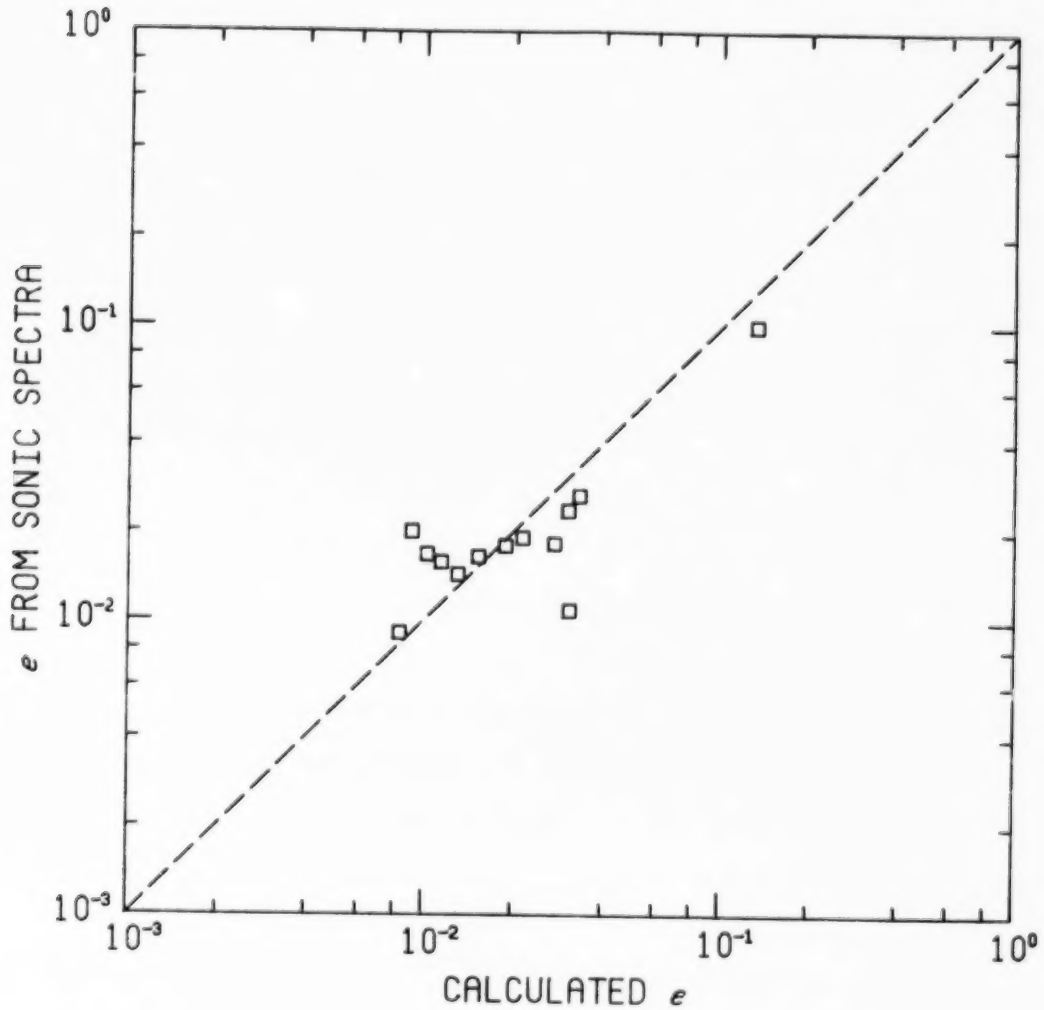

Figure 51. Dissipation, ε, obtained from sonic anemometer spectra versus ε calculated using empirical relationships. Reference height is 18.3 meters. The dashed line is the line along which the dissipation from either source is equal.

at 30 meters and above and that dissipation was equal to turbulent energy production below 30 meters. Fichtl and McVehil (1970) determined that the data collected at Cape Kennedy tended to favor a balance between dissipation and production of energy at 18 meters.

Because the sonic spectra apparently support a $k \approx 0.4$ (see Section XXIII on Kolmogorov Constant) if a Kolmogorov constant of about 0.5 is assumed, the z/L values used in this particular analysis were calculated using this value for k. Nondimensional dissipation, ϕ_ε, was then plotted against z/L. The resulting plot is shown in Figure 52. The solid line represents the results of Busch and Panofsky (1968), where

$$\phi_\varepsilon = 1, \; z/L \leq 0 \text{ and} \tag{24.18}$$

$$\phi_\varepsilon = 1 + 9\, z/L, \; z/L \geq 0. \tag{24.19}$$

The dashed line represents the relationship, $\phi_\varepsilon = \phi_m$ where

$$\phi_m = (1 - 16\, z/L)^{-1/4}, \; z/L \leq 0 \text{ and} \tag{24.20}$$

$$\phi_m = (1 + 4.7\, z/L), \; z/L \geq 0 \text{ (Businger } \underline{\text{et al.}}\text{, 1971).} \tag{24.21}$$

The points are generally low on the unstable side and seem to be nearly constant with z/L. The two points on the stable side are nearly centered about the solid line in apparent agreement with the results of Busch and Panofsky (1968).

Another plot of ϕ_ε versus z/L was produced using a u_* from 18 meter level cup and bivane measurements (Figure 53). The solid line is the same as on the previous plot. The dashed line represents the relation,

$$\phi_\varepsilon = \phi_m - z/L, \tag{24.22}$$

where ϕ_m is represented by the previously stated empirical equations. On the unstable side, the data tend to follow either line equally well.

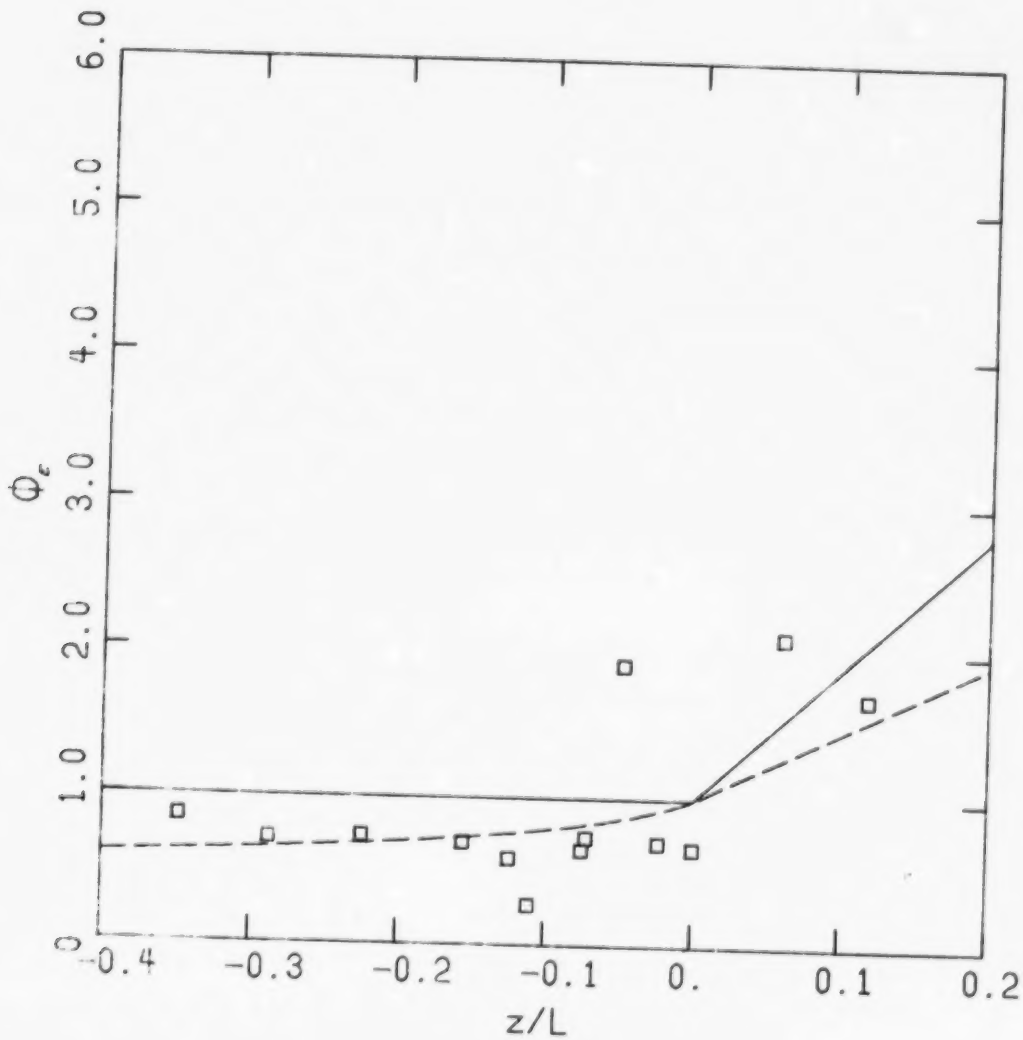

Figure 52. Nondimensional dissipation, ϕ_ε, versus z/L at 18.3 meters (sonic data). The dashed line represents the relation $\phi_\varepsilon = \phi_m$ where $\phi_m = (1 - 16\ z/L)^{-1/4}$ for $z/L \leq 0$ and $\phi_m = (1 + 4.7\ z/L)$ for $z/L \geq 0$. The solid line represents the results of Bush and Panofsky (1968): $\phi_\varepsilon = 1$ for $z/L \leq 0$ and $\phi_\varepsilon = \phi_m - z/L = 1 + 9\ z/L$ for $z/L \geq 0$.

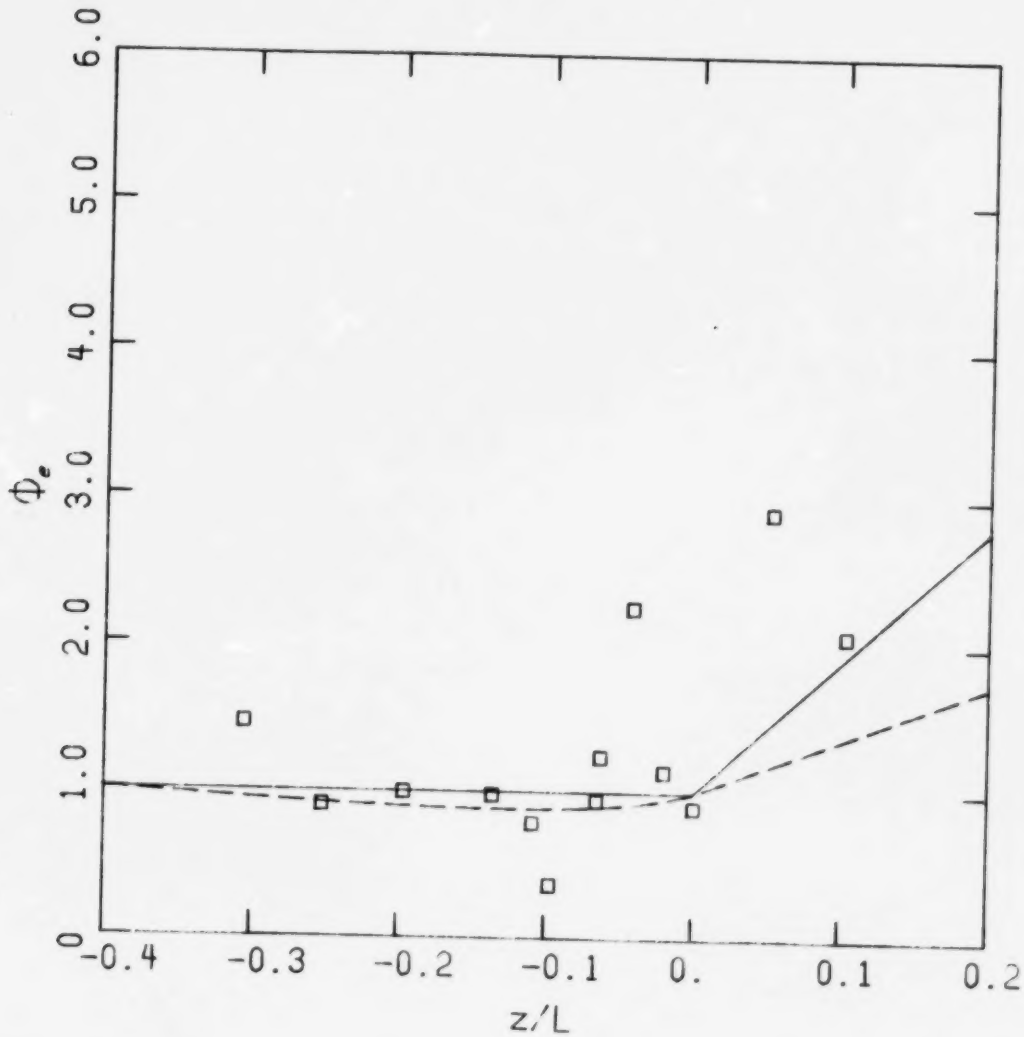

Figure 53. Nondimensional dissipation, ϕ_ε, versus z/L at 18.3 meters using cup and bivane measured friction velocities. The dashed line represents the relation, $\phi_\varepsilon = \phi_m - z/L$ where $\phi_m = (1 - 16\ z/L)^{-1/4}$ for $z/L \leq 0$ and $\phi_m = 1 + 4.7\ z/L$ for $z/L \geq 0$. The solid line represents the results of Bush and Panofsky (1968): $\phi_\varepsilon = 1$ for $z/L \leq 0$ and $\phi_\varepsilon = \phi_m - z/L = 1 + 9\ z/L$ for $z/L \geq 0$.

The stable side suffers from a shortage of points. This plot seems to support the contention that dissipation is balanced by the sum of buoyant and mechanical production at 18.3 m in agreement with the results of Busch and Panofsky (1968).

SECTION XV

DIMENSIONLESS TEMPERATURE GRADIENT, ϕ_h

Dimensional reasoning dictates that if the momentum and heat flux are used to nondimensionalize the potential temperature gradient, the dimensionless temperature gradient, ϕ_h, must be in the following form:

$$\phi_h = \frac{-kzu_*}{\overline{w'\theta'}} \frac{\partial\theta}{\partial z} \quad . \tag{25.1}$$

Similarity theory predicts that ϕ_h is a function of z/L in the surface layer of the atmosphere. To test the validity of this hypothesis and to determine whether it could be extended to levels above the surface layer, ϕ_h was calculated using two different techniques and then plotted against z/L. The two techniques were used in order to determine whether one produced superior results.

Method 1. The potential temperatures for the 6 levels of the tower (3, 36.6, 91.4, 137.2, 182.8 and 335.3 m) were fitted on ln z with a least squares polynomial regression of degree 2 for each of the 119 edited time periods. The resulting regression equations were differentiated with respect to ln z obtaining equations for $\partial\theta/\partial \ln z$ representing each time block. The dimensionless temperature gradients were then calculated for 91.4, 137.2, 182.9, 243.8, and 304.8 m using the relation below:

$$\phi_h = \frac{-ku_*}{\overline{w'\theta'}} \frac{\partial\theta}{\partial \ln z} \quad , \tag{25.2}$$

where calculations of u_* and $\overline{w'\theta'}$ from the 18.3 meter level were used as representative of the surface or constant flux layer.

Method 2. A finite difference approximation for $\partial\theta/\partial z$ was used in terms of the same potential temperatures as in Method 1. The

dimensionless temperature gradient was calculated using the expression:

$$\phi_h = \frac{-k\bar{z}}{\overline{w'\theta'}} \frac{\Delta\theta}{\Delta z} , \qquad (25.3)$$

where $\bar{z} = \frac{z_2 - z_1}{\ln \frac{z_2}{z_1}}$ is the height to which ϕ_h is referenced.

Values of ϕ_h were calculated for 5 levels intermediate (as determined by $\bar{z}$) to the 6 levels from which the potential temperatures were measured.

Plots of ϕ_h versus z/L were produced corresponding to each level for which ϕ_h was calculated using Method 1 (Figures 54 through 59). For positive z/L values the plots display considerable scatter which increases with height. For z/L values less than zero the ϕ_h's are suppressed and tend to fall slightly below the line. The solid lines on all of the plots are from the empirical expressions (Businger et al., 1971):

$$\phi_h = \frac{0.74}{(1 - 9\ z/L)^{1/2}} \quad z/L \leq 0 \text{ and} \qquad (25.4)$$

$$\phi_h = 0.74 + 4.7\ z/L \quad z/L \geq 0. \qquad (25.5)$$

Plots of ϕ_h calculated using Method 2 appear in Figures 60 through 64. These are similar in most respects to those using Method 1. Of particular interest is the fact that only one point appears at the highest level plotted (289.1 m) for $z/L < 0$. In closely examining all plots using either method, it can be seen that the number of points plotted decreases with height. The reason for this in most cases is because the stability as indicated by the vertical heat flux ($\overline{-w'\theta'}$) does not agree in sign with the stability as indicated by the potential

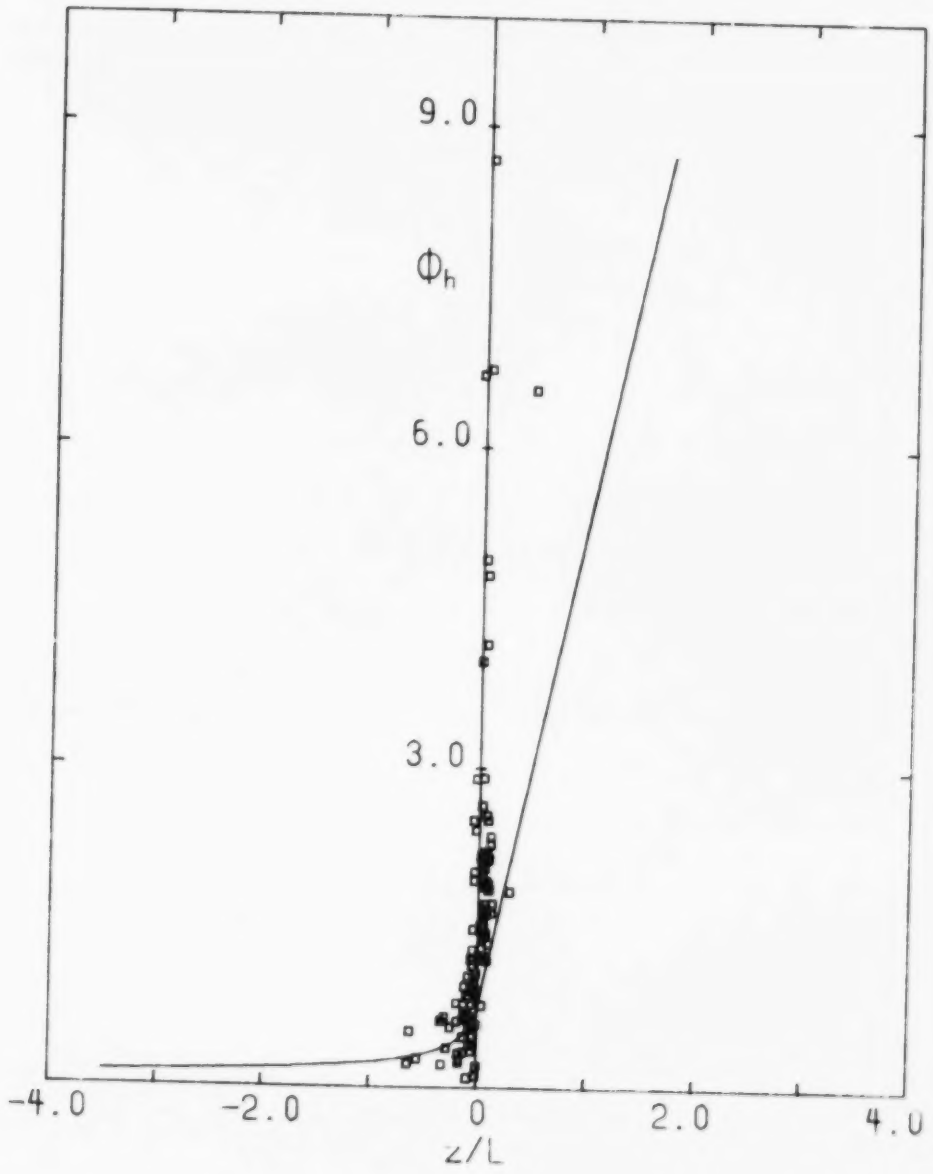

Figure 54. Nondimensional temperature gradient, ϕ_h (Method 1) versus z/L at 18.3 meters. The solid line represents the results of Businger et al. (1971): $\phi_h = 0.74\ (1 - 9\ z/L)^{-1/2}$ for $z/L \leq 0$ and $\phi_h = 0.74 + 4.7\ z/L$ for $z/L \geq 0$.

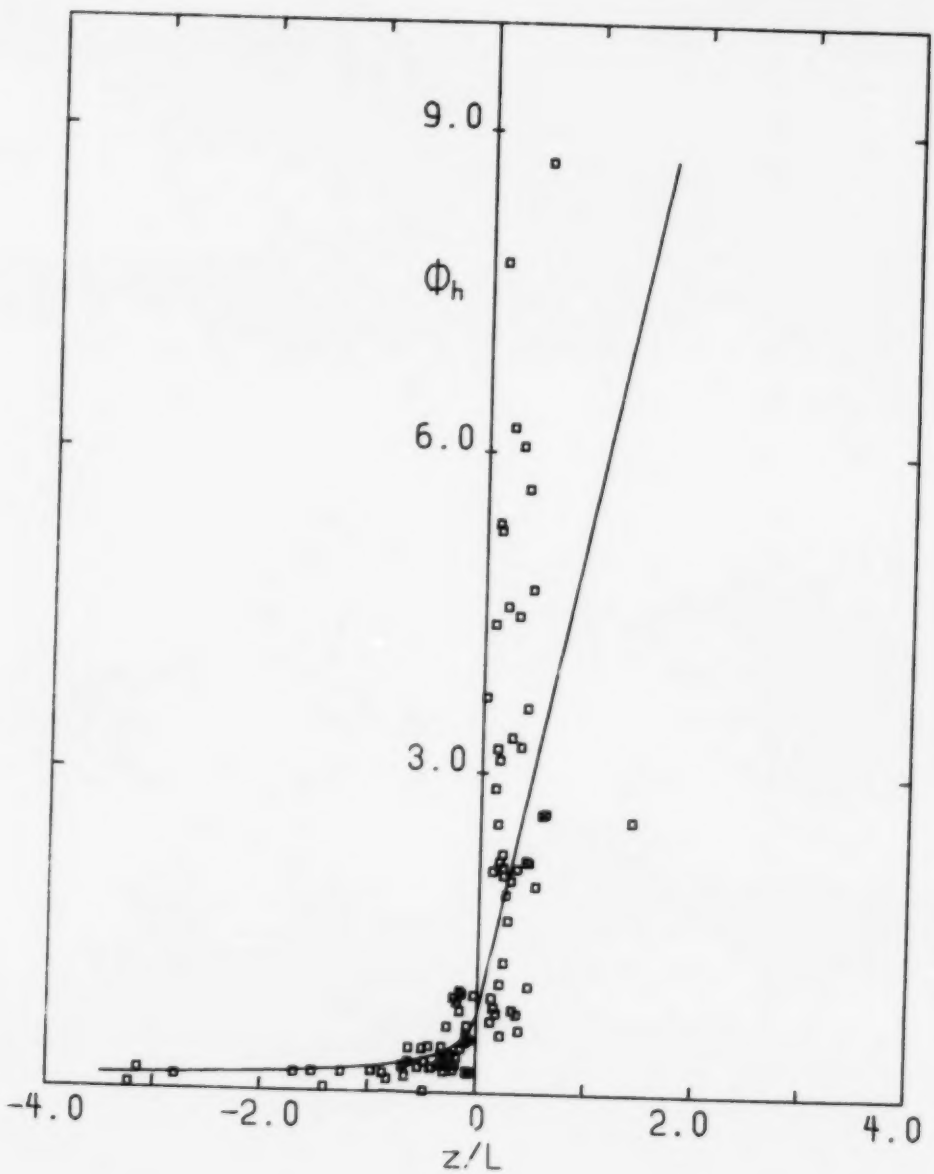

Figure 55. Nondimensional temperature gradient, ϕ_h, (Method 1) versus z/L at 91.4 meters. The solid line represents the results of Businger et al. (1971): $\phi_h = 0.74\ (1 - 9\ z/L)^{-1/2}$ for $z/L \leq 0$ and $\phi_h = 0.74 + 4.7\ z/L$ for $z/L \geq 0$.

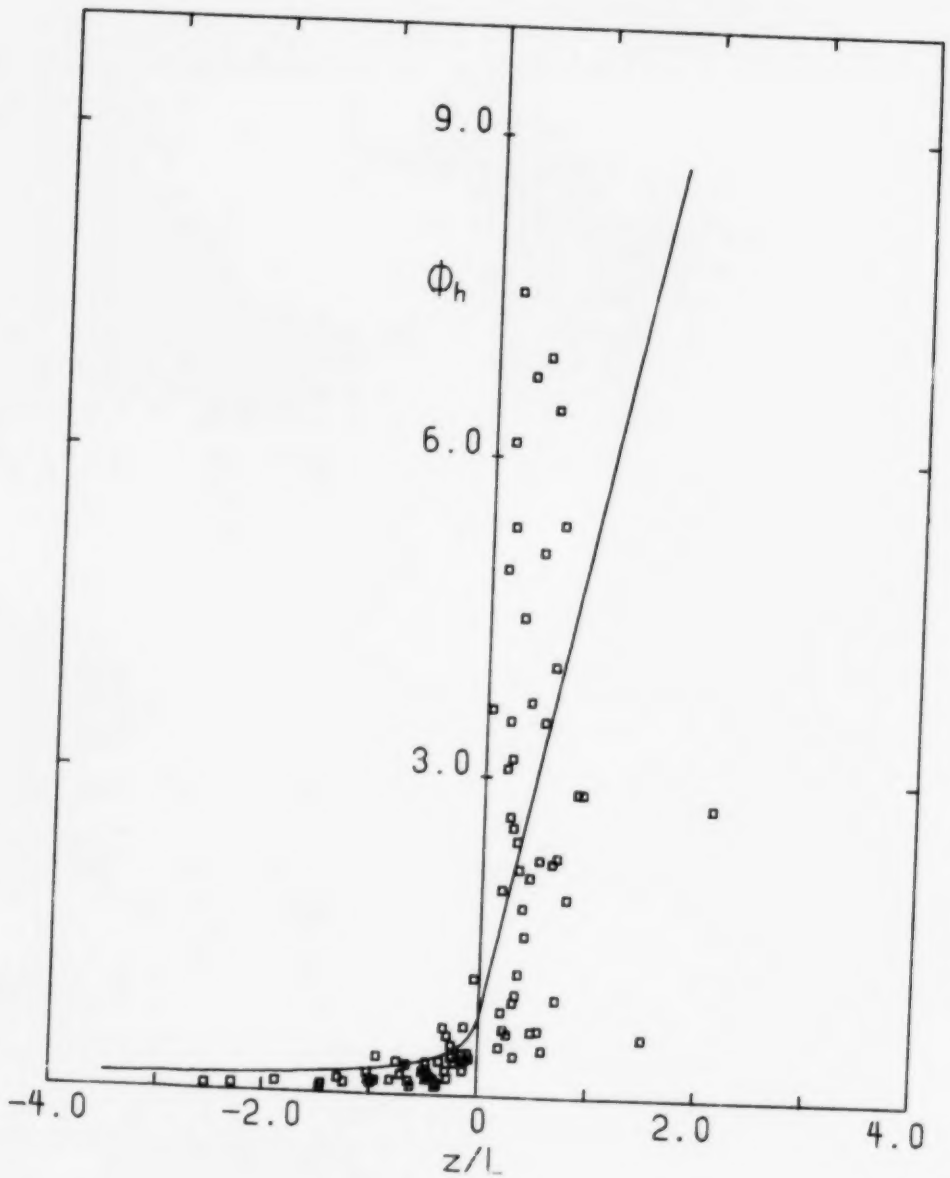

Figure 56. Nondimensional temperature gradient, ϕ_h, (Method 1) versus z/L at 137.2 meters. The solid line represents the results of Businger et al. (1971): $\phi_h = 0.74\ (1 - 9\ z/L)^{-1/2}$ for $z/L \leq 0$ and $\phi_h = 0.74 + 4.7\ z/L$ for $z/L \geq 0$.

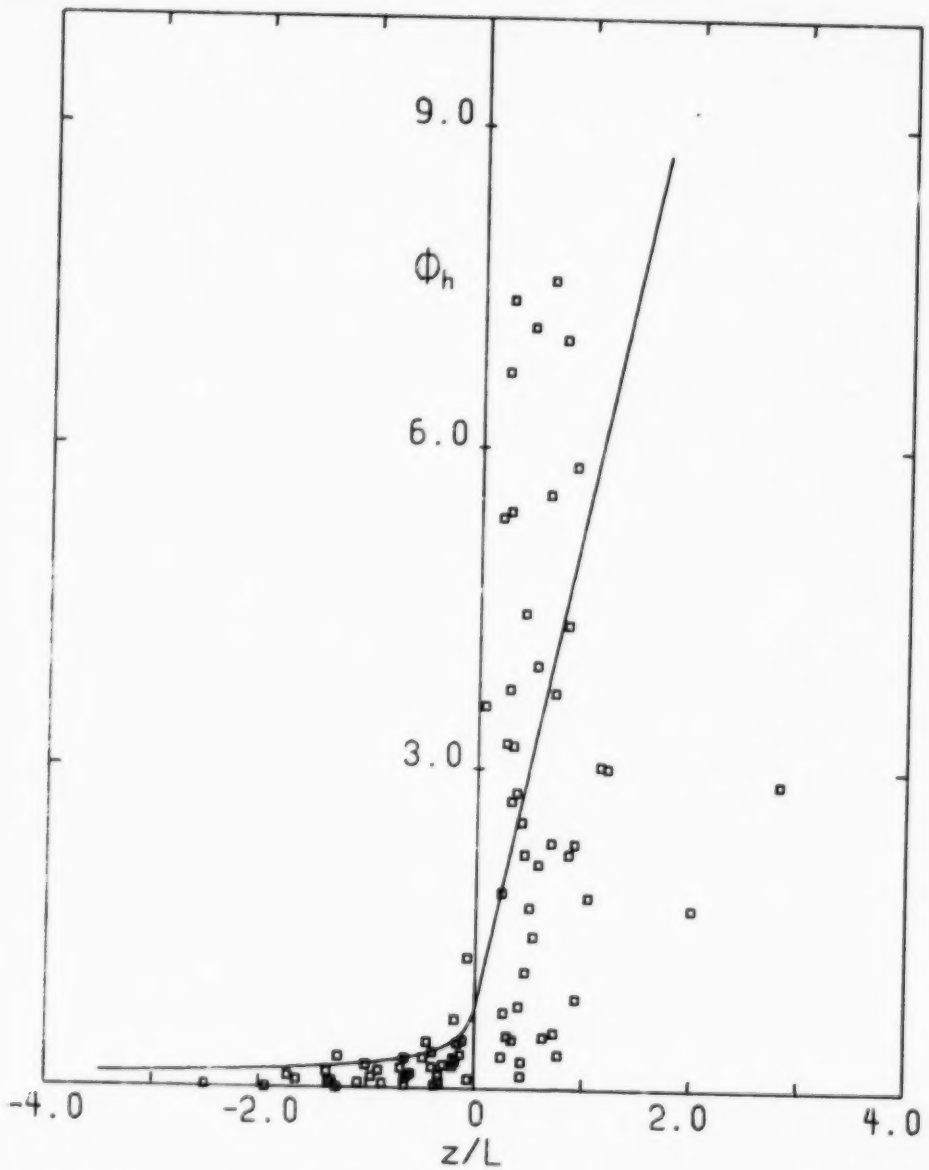

Figure 57. Nondimensional temperature gradient, ϕ_h, (Method 1) versus z/L at 182.9 meters. The solid line represents the results of Businger *et al.* (1971): $\phi_h = 0.74\ (1 - 9\ z/L)^{-1/2}$ for $z/L \leq 0$ and $\phi_h = 0.74 + 4.7\ z/L$ for $z/L \geq 0$.

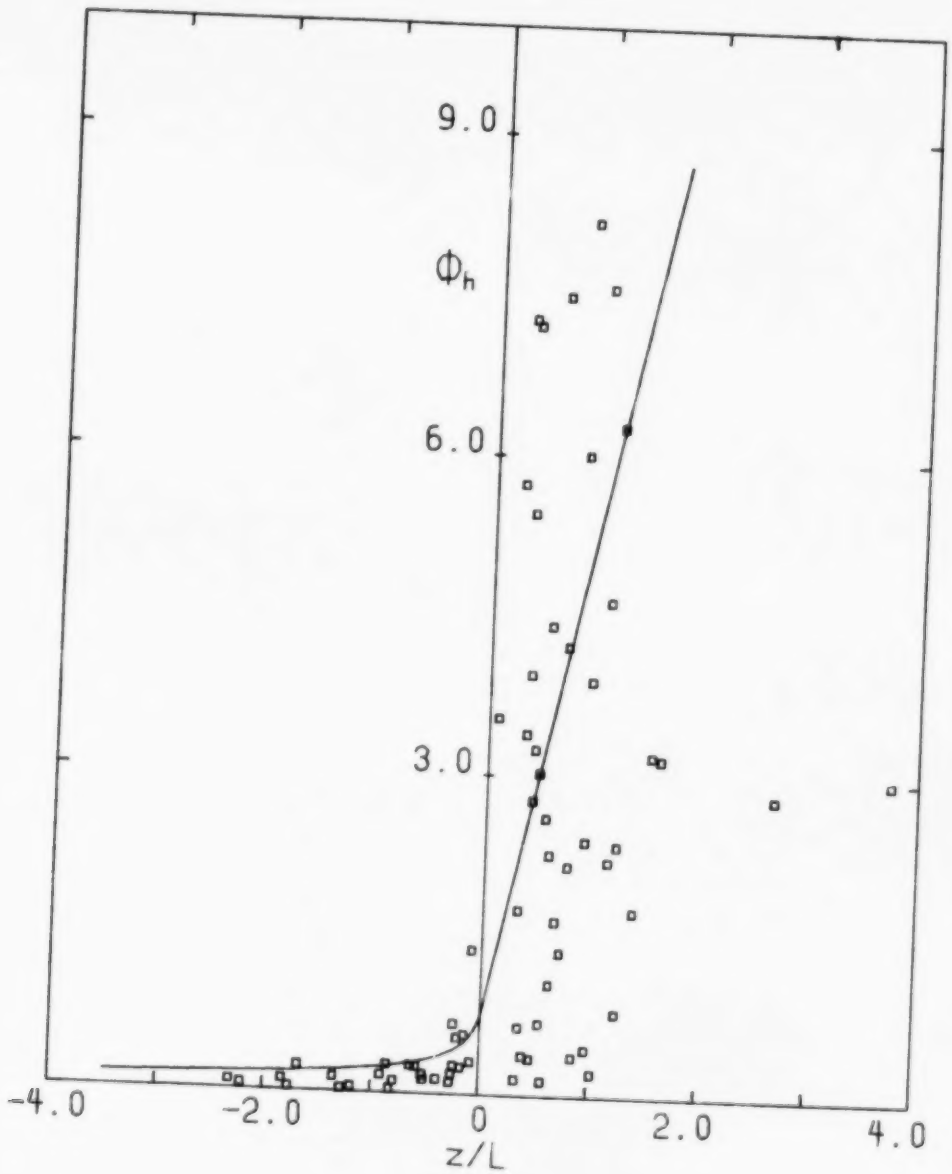

Figure 58. Nondimensional temperature gradient, ϕ_h, (Method 1) versus z/L at 243.8 meters. The solid line represents the results of Businger *et al.* (1971): $\phi_h = 0.74\ (1 - 9\ z/L)^{-1/2}$ for $z/L \leq 0$ and $\phi_h = 0.74 + 4.7\ z/L$ for $z/L \geq 0$.

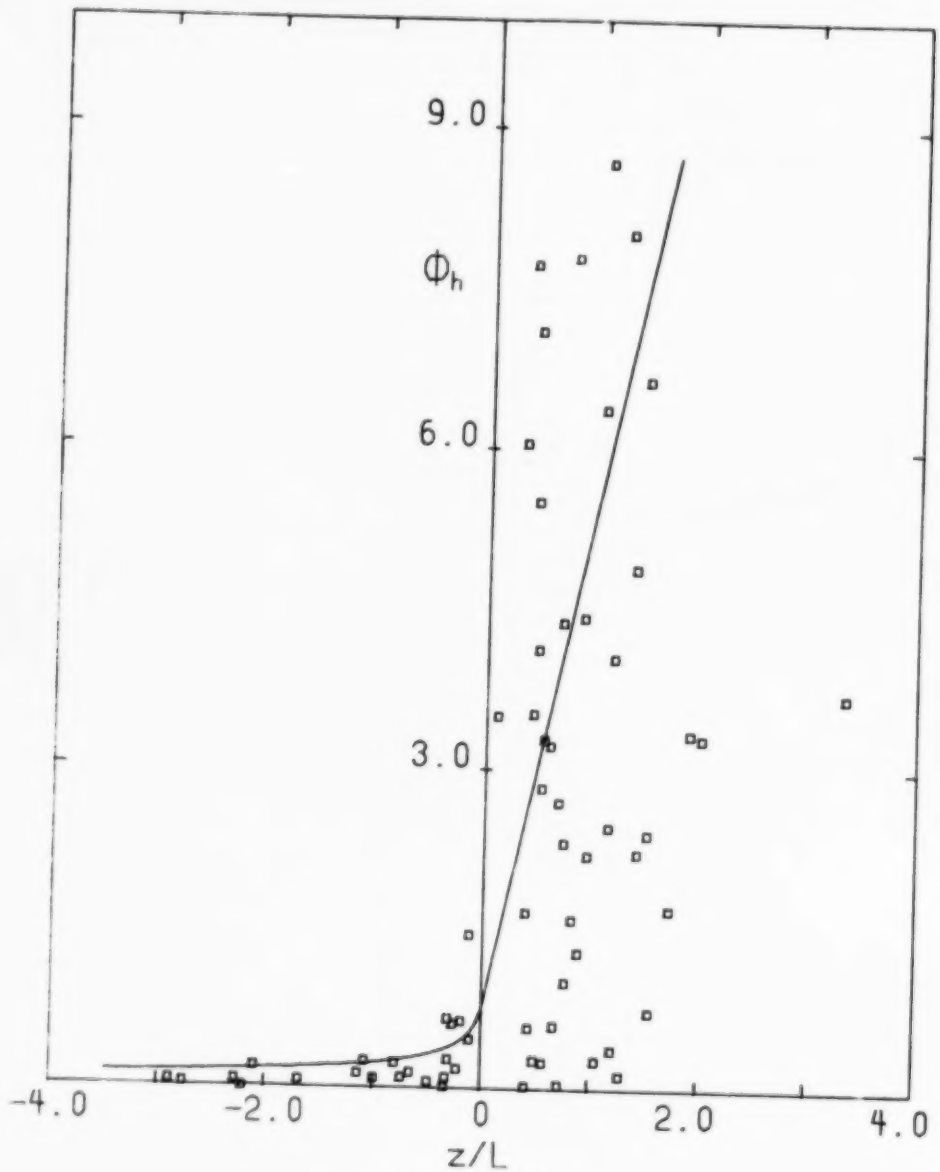

Figure 59. Nondimensional temperature gradient, ϕ_h, (Method 1) versus z/L at 304.8 meters. The solid line represents the results of Businger et al. (1971): $\phi_h = 0.74\ (1 - 9\ z/L)^{-1/2}$ for $z/L \leq 0$ and $\phi_h = 0.74 + 4.7\ z/L$ for $z/L \geq 0$.

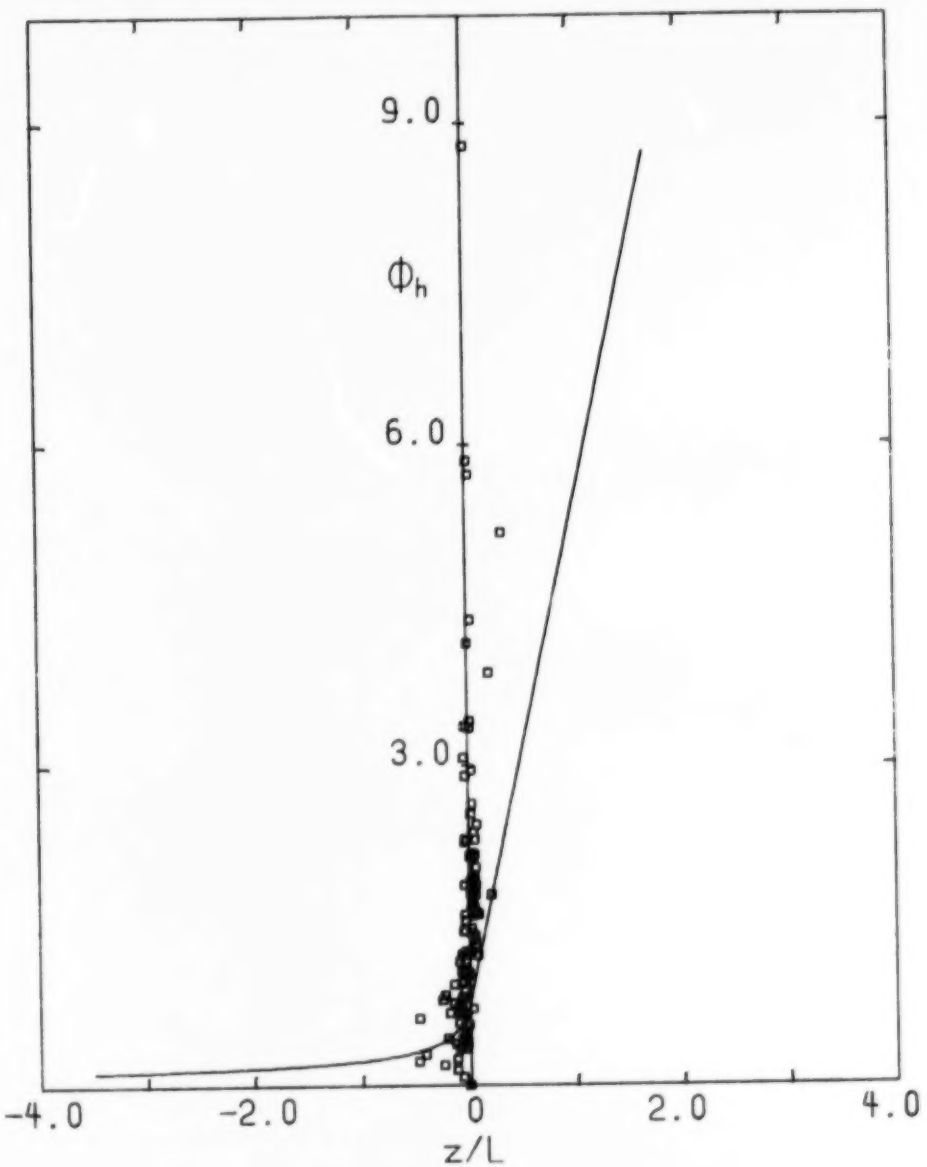

Figure 60. Nondimensional temperature gradient, ϕ_h, (Method 2) versus z/L at 13.5 meters. The solid line represents the results of Businger et al. (1971): $\phi_h = 0.74\ (1 - 9\ z/L)^{-1/2}$ for $z/L \leq 0$ and $\phi_h = 0.74 + 4.7\ z/L$ for $z/L \geq 0$).

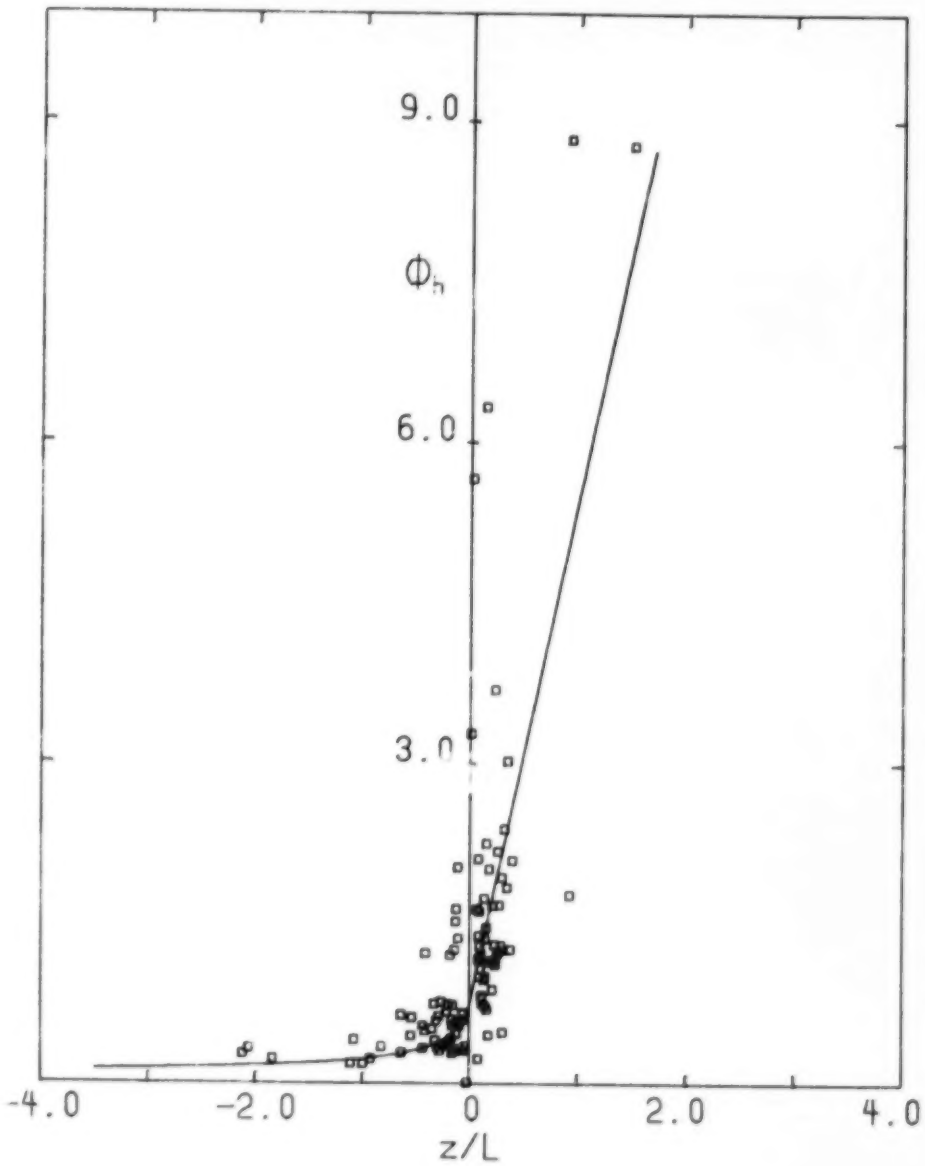

Figure 61. Nondimensional temperature gradient, ϕ_h, (Method 2) versus z/L at 59.9 meters. The solid line represents the results of Businger *et al.* (1971): $\phi_h = 0.74\ (1 - 9\ z/L)^{-1/2}$ for $z/L \leq 0$ and $\phi_h = 0.74 + 4.7\ z/L$ for $z/L \geq 0$.

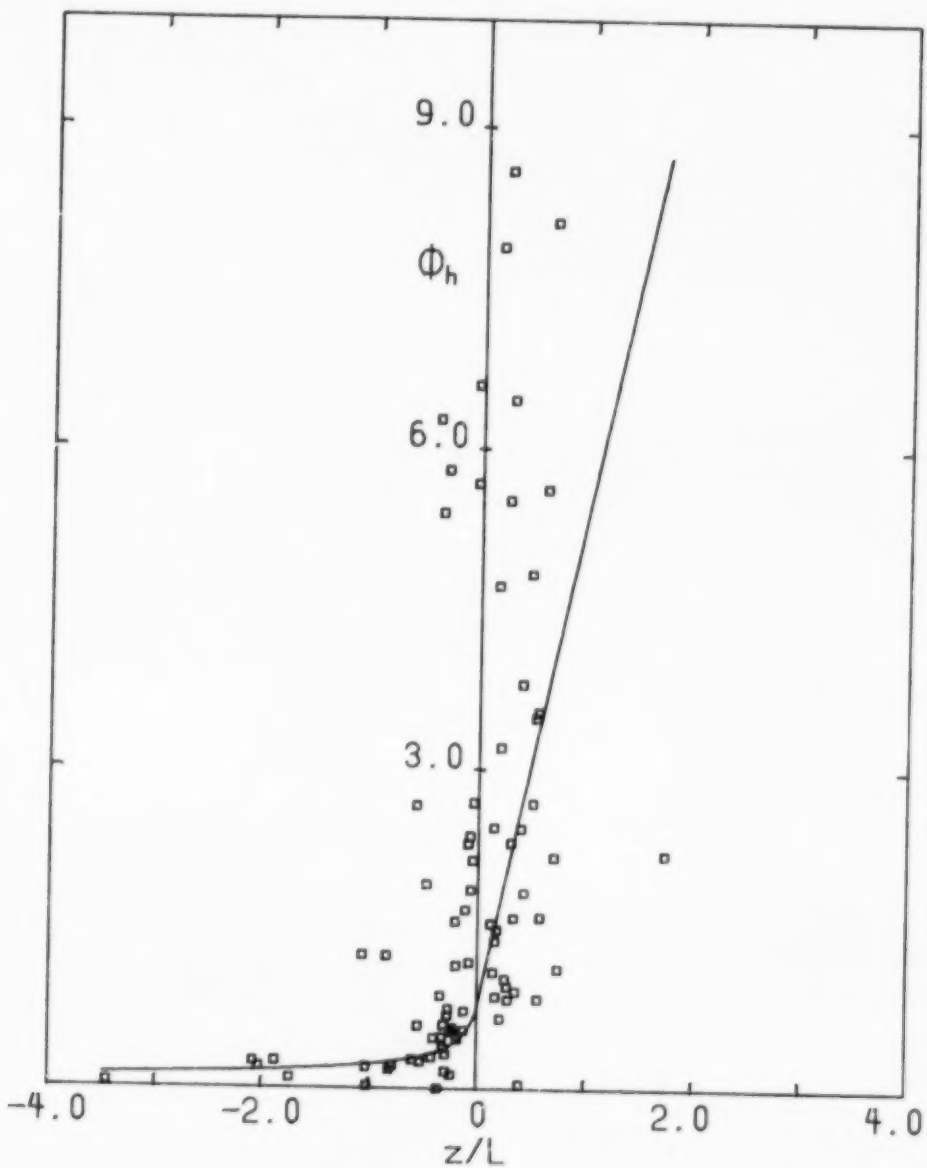

Figure 62. Nondimensional temperature gradient, ϕ_h, (Method 2) versus z/L at 112.8 meters. The solid line represents the results of Businger *et al.* (1971): $\phi_h = 0.74\ (1 - 9\ z/L)^{-1/2}$ for $z/L \leq 0$ and $\phi_h = 0.74 + 4.7\ z/L$ for $z/L \geq 0$.

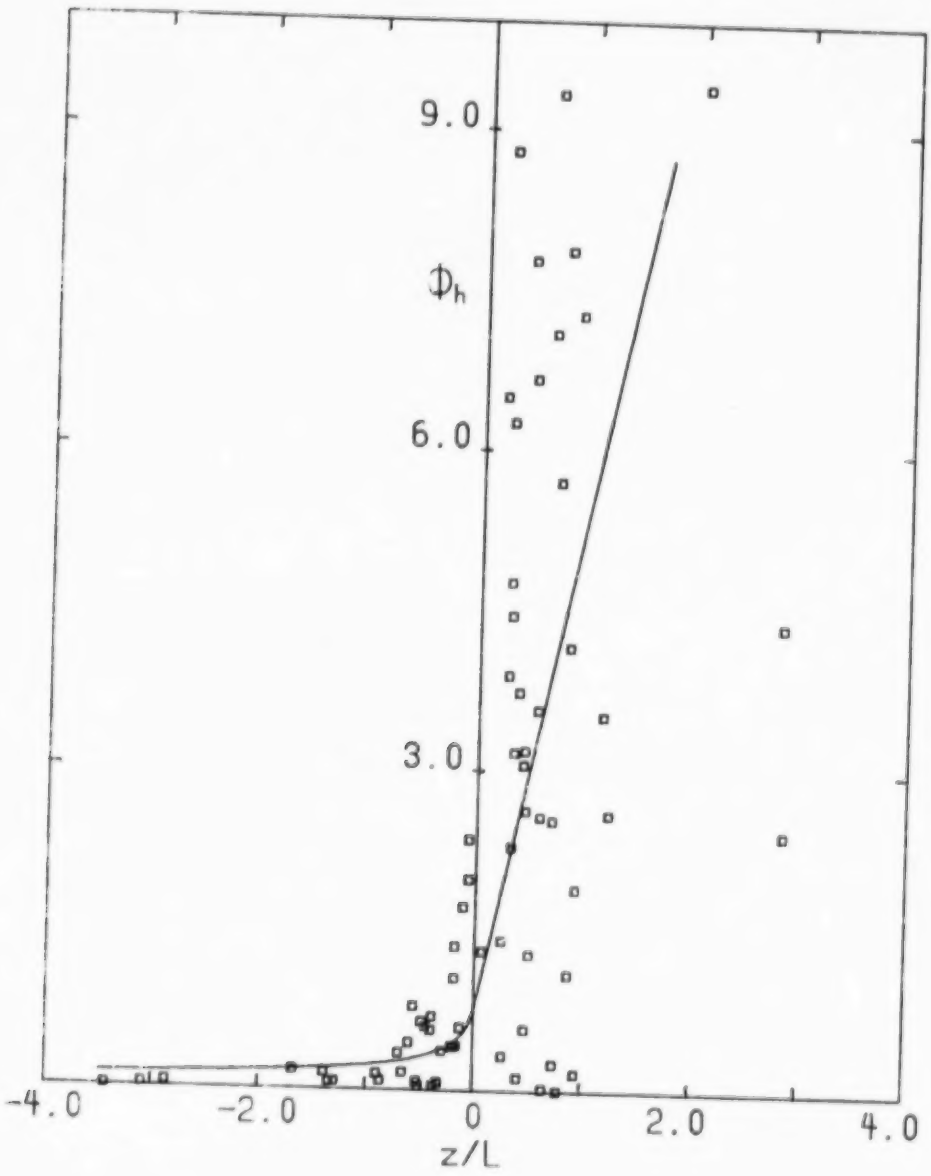

Figure 63. Nondimensional temperature gradient, ϕ_h, (Method 2) versus z/L at 185.4 meters. The solid line represents the results of Businger et al. (1971): $\phi_h = 0.74\ (1 - 9\ z/L)^{-1/2}$ for $z/L \leq 0$ and $\phi_h = 0.74 + 4.7\ z/L$ for $z/L \geq 0$.

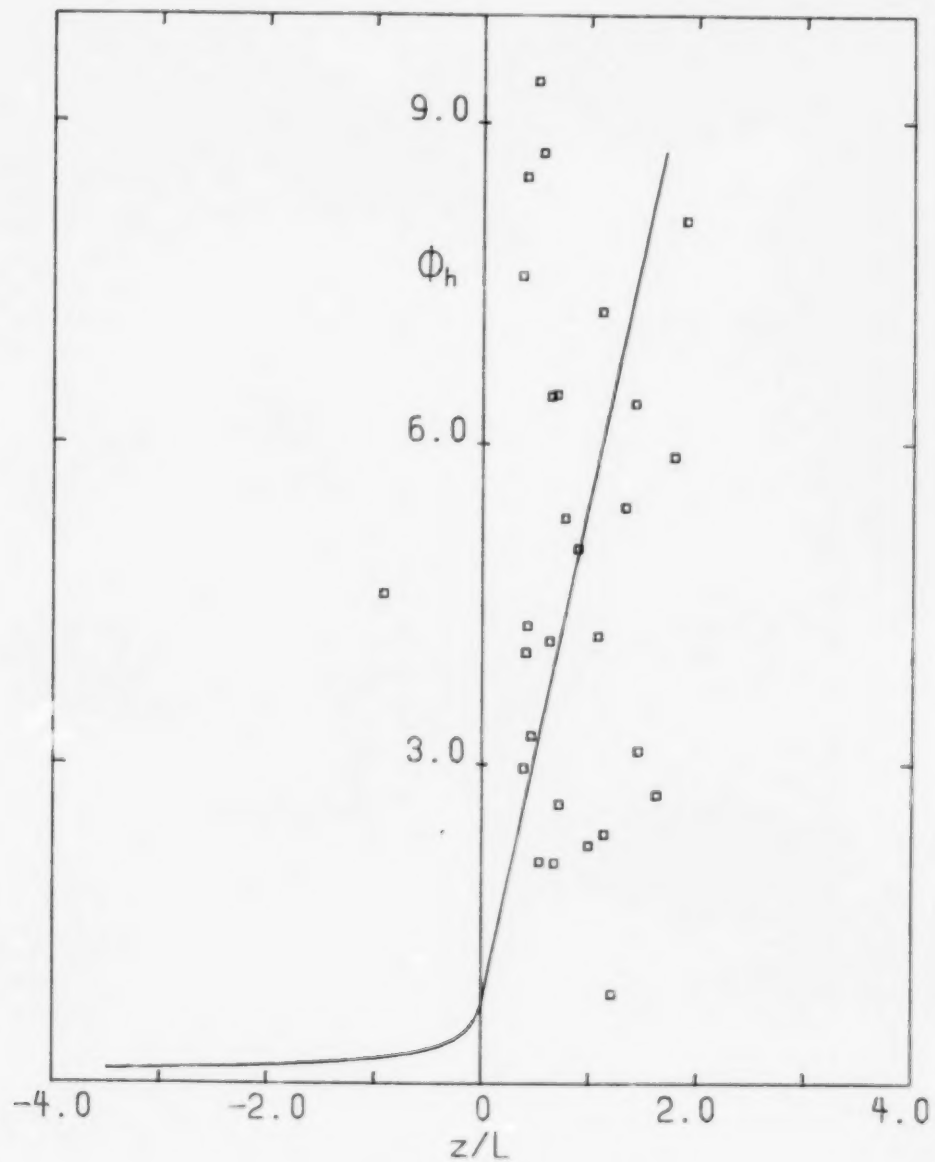

Figure 64. Nondimensional temperature gradient, ϕ_h, (Method 2) versus z/L at 289.1 meters. The solid line represents the results of Businger et al. (1971): $\phi_h = 0.74\ (1 - 9\ z/L)^{-1/2}$ for $z/L \leq 0$ and $\phi_h = 0.74 + 4.7\ z/L$ for $z/L \geq 0$.

temperature gradient ($\partial\theta/\partial z$). The heat flux indicates a dynamic or turbulent stability while the potential temperature indicates a static stability. It can be seen from the definition of the dimensionless temperature gradient that, ideally, ϕ_h approaches an indeterminate value as z/L approaches 0 (i.e. $\lim_{z/L \to 0} \frac{\partial\theta/\partial z}{\overline{w'\theta'}} \to \frac{0}{0}$). This explains the large amount of scatter near zero.

Neither method of calculating ϕ_h produced clearly superior results. In general, the plots from both methods contain considerable scatter and roughly 1/3 of the total number of points were not plotted because of negative ϕ_h values (in most cases) and also because ϕ_h fell outside of the bounds of the plot in the case of those non-negative values not plotted.

SECTION XXVI

REFERENCES

1. Air Ministry, 1961: Handbook of Meteorological Instruments, Part II, Instruments for Upper Air Observations. Her Majesty's Stationery Office, London.

2. Bendat, J. S., and A. G. Piersol, 1971: Random Data; Analysis and Measurement Procedures. Wiley-Intersciences, New York.

3. Blackadar, A. K., and H. Tennekes, 1968: Asymptotic similarity in neutral barotropic planetary boundary layers. Journal of the Atmospheric Sciences, vol. 25, pp. 1015-1020.

4. Blackadar, A. K., H. A. Panofsky, and F. Fiedler, 1974: Investigation of the turbulent wind field below 500 feet altitude at the Eastern Test Range, Florida. NASA Contractor Report, NASA CR-2438.

5. Boston, N., 1970: An investigation of high wave number temperature and velocity spectra in air. Ph.D. Thesis, University of British Columbia, Vancouver, British Columbia.

6. Busch, N. E., 1973: The surface boundary layer. Boundary-Layer Meteorology, vol. 4, pp. 213-240.

7. Busch, N. E., and H. A. Panofsky, 1968: Recent spectra of atmospheric turbulence. Quarterly Journal of the Royal Meteorological Society, vol. 94, pp. 132-148.

8. Businger, J. A., 1972: Turbulent transfer in the atmospheric surface layer. Workshop on Micrometeorology, American Meteorological Society, Boston, Massachusetts, pp. 1-69.

9. Businger, J. A., J. C. Wyngaard, Y. Izumi, and E. F. Bradley, 1971: Flux-profile relationships in the atmospheric surface layer. Journal of the Atmospheric Sciences, vol. 28, pp. 181-189.

10. Clark, R. H., 1970: Observational studies in the atmospheric boundary layer. Quarterly Journal of the Royal Meteorological Society, vol. 96, pp. 91-119.

11. Cooper, R. E., and B. C. Rusche, 1968: The SRL Meteorological Program and Off-Site Dose Calculations. E. I. DuPont de Nemours & Company, Aiken, South Carolina.

12. Cramer, H. E., 1964: Meteorological Prediction on Techniques and Data Systems. Report GCA-64-3-6, Geophysical Corporation of America, Bedford, Massachusetts.

13. Crawford, T. V., 1974: Progress Report Dose-To-Man FY 1973. E. I. DuPont de Nemours & Company, Aiken, South Carolina.

14. Deardorff, J. W., 1970: Preliminary results from numerical integrations of the unstable planetary boundary layer. Journal of the Atmospheric Sciences, vol. 27, pp. 1209-1211.

15. Fichtl, G. H., and G. E. McVehil, 1970: Longitudinal and lateral spectra of turbulence in the atmospheric boundary layer at the Kennedy Space Center. Journal of Applied Meteorology, vol. 9, pp. 51-63.

16. Frenzen, P., 1973: The observed relation between the Kolmogorov and von Karman constants in the surface boundary layer. Boundary-Layer Meteorology, vol. 3, pp. 348-358.

17. Gibson, C. H., G. R. Stegen, and R. B. Williams, 1970: Statistics of the fine structure of turbulent velocity and temperature fields measured at high Reynolds number. Journal of Fluid Mechanics, vol. 41, pp. 153-167.

18. Gill, G. C. et al., 1967: Accuracy of wind measurements on towers and stacks. Bulletin, American Meteorological Society, vol. 48, pp. 665-674.

19. Gurvic, A. S., 1960: An experimental investigation of the frequency spectra of the vertical component of the wind velocity in the bottom layer of the atmosphere. Academy Science, Union of Soviet Socialist Republic, vol. 130, pp. 806-809.

20. Horst, T. W., 1973: Corrections for Response Errors in a Three Component Propeller Anemometer. BNWL-SA-4262, Battelle Memorial Institute, Pacific Northwest Laboratories, Richland, Washington.

21. Irwin, J. S., 1974: Analysis of turbulence parameters in the lowest 300 meters of the atmosphere. Master's Thesis (unpublished), Department of Geosciences, North Carolina State University, Raleigh, North Carolina.

22. Kaimal, J. C., and D. A. Haugen, 1967: Characteristics of vertical velocity fluctuations observed on a 430 m. tower. Quarterly Journal of the Royal Meteorological Society, vol. 93, pp. 305-317.

23. Kaimal, J. C., and C. N. Touart, 1967: Critical examination of a transformation to vector-mean coordinates. Journal of Applied Meteorology, vol. 6, pp. 583-587.

24. Kaimal, J. C., J. C. Wyngaard, Y. Izumi, and O. R. Coté, 1972: Spectral characteristics of surface-layer turbulence. Quarterly Journal of the Royal Meteorological Society, vol. 98, pp. 563-589.

25. Kitaigorodskii, S. A., 1973: The Physics of Air-Sea Interaction. Israel Program for Scientific Translations Ltd., Jerusalem, Israel, p. 19.

26. Lumley, J. L., and H. A. Panofsky, 1964: The Structure of Atmospheric Turbulence. Interscience Publishers, New York.

27. Mitsuta, Y., M. Miyake, and Y. Kobori, 1967: Three dimensional sonic anemometer-thermometer for atmospheric turbulence measurement. In Development of Sonic Anemometer-Thermometer and Its Applications to the Study of Atmospheric Surface Layer. Kyoto University, Kyoto, Japan, pp. 37-56.

28. Monin, A. S., and A. M. Obukhov, 1954: Basic regularity in turbulent mixing in the surface layer of the atmosphere. Academy Science, Union of Soviet Socialist Republic, no. 24, pp. 163-178.

29. Nickerson, E. C., 1973: Atmospheric boundary layer models. Lecture Notes (unpublished), University of Tennessee Space Institute, Knoxville, Tennessee.

30. Panofsky, H. A., 1972: Tower micrometeorlogy. Workshop on Micrometeorology, American Meteorological Society, Boston, Massachusetts, pp. 1-69.

31. Panofsky, H. A., and G. W. Brier, 1958: Some Applications of Statistics to Meteorology. The Pennsylvania State University, University Park, Pennsylvania.

32. Panofsky, H. A., and R. A. McCormick, 1960: The spectrum of vertical velocity near the surface. Quarterly Journal of the Royal Meteorological Society, vol. 86, pp. 495-503.

33. Panofsky, H. A., and B. Prasad, 1965: Similarity theories and diffusion. Journal of Air and Water Pollution, vol. 9, pp. 419-430.

34. Panofsky, H. A., and A. A. Townsend, 1964: Change of terrain roughness and the wind profile. Quarterly Journal of the Royal Meteorological Society, vol. 90, pp. 147-155.

35. Pasquill, F., 1962: Recent broad-band spectral measurements of turbulence in the lower atmosphere. Journal of Geophysical Research, vol. 67, pp. 3025-3029.

36. Pasquill, F., 1972: Some aspects of boundary layer description. Quarterly Journal of the Royal Meteorological Society, vol. 98, pp. 469-494.

37. Paulson, C. A., 1970: The mathematical representation of wind speed and temperature profiles in the unstable atmospheric surface layer. Journal of Applied Meteorology, vol. 9, pp. 857-861.

38. Petersen, W. B., 1974: Analysis of turbulence parameters from the 366 meter SRL-WJBF tower. Master's Thesis (unpublished), Department of Geosciences, North Carolina State University, Raleigh, North Carolina.

39. Singleton, R. C., 1969: An algorithm for computing the Mixed Radix Fast Fourier Transform. IEEE Transactions on Audio Electroacoustics, vol. AU-17, No. 2.

40. Slade, D. H., 1969: Wind measurements on a tall tower in rough inhomogeneous terrain. Journal of Applied Meteorology, vol. 8, pp. 293-297.

41. Smith, M., 1968: ASME Guide for Prediction of the Dispersion of Airborn Effluents. American Society of Mechanical Engineers, New York, New York.

42. Stearns, C. R., 1970: Conversion of profile differences to true gradients at the geometric mean height in the surface layer. Boundary-Layer Meteorology, vol. 1, pp. 146-154.

43. Tennekes, H., 1972: Similarity laws and scale relations in planetary boundary layers. Workshop on Micrometeorology, American Meteorological Society, Boston, Massachusetts, pp. 1-56.

44. Weber, A. H., and L. D. Sanders, 1970: Evaluation of roughness lengths at the NSSL-WKY Meteorological Tower. ESSA Technical Memorandum, ERLTM-NSSL 47.

45. Wyngaard, J. C., and O. R. Cote, 1971: The budgets of turbulent kinetic energy and temperature variance in the atmospheric surface layer. Journal of the Atmospheric Sciences, vol. 28, pp. 190-201.

46. Wyngaard, J. C., and Y. H Pao, 1972: Some measurements of the fine structure of large Reynolds number turbulence. Proceedings, Symposium on Statistical Models and Turbulence, La Jolla, Cal. 1971, Springer-Verlag, Berlin, pp. 384-401.

47. Yokoyama, O., 1971: An experimental study of the structure of turbulence in the lowest 500 meters of the atmosphere and diffusion in it. Reports of the National Institute for Pollution and Resources, Tokyo, Japan.

SECTION XXVII

APPENDICES

		Page
A.	Leveling Procedure	141
B.	Thermistor Discussion	142
C.	Details of Data Editing	143
D.	σ_E, σ_A Functions of fz/u_*	146

APPENDIX A

Leveling Procedure

The cup and bivane system was mounted on the end of an extremely rigid, heavy steel boom whose length was 6 meters. The actual mounting of the booms and installation of instruments was performed by subcontractors for SRL. Prior to collecting data for this experiment, it was found that the instruments had no guarantee of being level with respect to gravity. To eliminate this source of error a means was devised for leveling the instruments. First the booms were retracted and the cup and bivane masts were leveled. (Each boom had two degrees of freedom of movement; up and down and rotational). Then a portable reference mast was strapped at approximately 2.5 meters from the back end of the boom. The mast was attached to the boom by means of a saddle which securely held its position fixed. The reference mast was leveled and the boom was then pushed out in its extended position. By using the portable mast as a reference the boom was leveled and bolted in position. The sensitivity of the level was within 1/500 of a degree.

The Gill and Sonic anemometers had electrostatic levels installed on the base of each instrument. Guy-wires were attached to hold the flexible aluminum booms steady. Using a remote sensor and by tightening and loosening turnbuckles mounted on the guy-wires the Gill and Sonic instruments were leveled to 1/10 of a degree.

APPENDIX B

Thermistor Discussion

The thermistor and bridge circuit were provided by Battelle Northwest. The thermistor, a Ceco microbead thermistor (#31A401C), was purchased from Victory Engineering Corporation. The voltage signals from the thermistor bridge circuit were amplified and connected to the DAS. The DAS amplified by a factor of 10 with a maximum range of ±10 volts. Thus the output from the bridge circuit was limited to be less than one volt by setting the initial amplifier gain. The bridge circuit was designed by Battelle Northwest to yield a nearly linear relationship between voltage output and temperature fluctuations.

The characteristic time (τ) and dissipation constant of the thermistor were 0.03 sec. (in water) and 0.045 watts/sec., respectively. The low value of the dissipation constant means that self heat effects were negligible and the low value of τ means that the response of the thermistor was fast enough to obtain meaningful temperature fluctuations while sampling at 10 times per second.

APPENDIX C

Details of Data Editing

Time	Code	Time	Code	Time	Code
139/10:40:22	3	142/01:00:24	1	143/15:49:23	4
139/11:55:04	U	142/01:40:24	1	144/07:59:23	5
139/12:35:04	U	142/02:20:24	3	144/08:39:23	N
139/13:15:04	1	142/03:00:24	3	144/09:19:23	U
139/13:55:16	N	142/03:40:24	2	144/09:59:23	U
139/14:35:40	1	142/04:20:24	4	144/10:39:47	N
139/15:15:40	U	142/12:54:49	U	144/12:08:57	U
139/15:55:52	U	142/13:34:49	U	144/12:48:57	N
139/16:35:52	4	142/14:14:49	1	144/13:34:47	N
140/12:18:12	U	142/14:54:49	U	144/14:14:59	N
140/12:58:12	1	142/15:34:49	1	144/14:54:59	N
140/13:38:12	U	142/16:14:47	U	144/15:34:59	4
140/14:18:12	1	142/16:54:47	N	144/16:40:11	N
140/14:58:12	U	142/17:34:47	1	144/17:20:11	N
140/15:38:12	U	142/18:14:47	1	144/18:41:25	N
140/16:18:12	4	142/18:54:47	1	144/19:21:25	N
140/17:40:11	N	142/19:34:47	1	144/20:01:25	S
140/18:20:11	S	142/20:43:11	1	144/21:03:01	S
140/19:00:11	S	142/21:23:11	1	144/21:43:01	S
140/19:40:11	2	142/22:03:11	4	144/22:23:01	S
140/20:20:11	2	142/22:29:24	1	144/23:03:01	S
140/21:00:11	2	142/23:09:24	2	144/23:43:01	S
140/21:40:11	4	142/23:49:24	1	145/00:23:01	S
140/22:30:25	1	143/00:29:24	2	145/01:03:01	1
140/23:10:25	2	143/01:09:24	1	145/01:43:01	4
140/23:50:25	2	143/01:49:24	1	145/08:20:42	5
141/00:30:25	2	143/02:29:24	1	145/10:11:28	U
141/01:10:25	2	143/03:09:24	1	145/11:31:05	U
141/01:50:25	2	143/03:49:24	1	145/12:57:10	1
141/02:30:25	1	143/04:29:24	1	145/14:09:41	U
141/03:10:25	S	143/05:09:24	S	145/14:49:41	4
141/03:50:25	1	143/05:49:24	1	145/15:42:24	1
141/04:30:25	2	143/06:29:24	4	145/16:22:48	1
141/05:10:25	1	143/07:09:23	1	145/17:02:48	U
141/05:50:25	1	143/07:49:23	5	145/17:43:12	U
141/06:30:25	6	143/08:29:23	U	145/18:23:12	3
141/18:20:24	3	143/09:09:23	N	145/19:03:12	2
141/19:00:24	3	143/09:49:23	U	145/19:43:12	1
141/19:40:24	1	143/10:29:23	U	145/20:23:12	1
141/20:20:24	1	143/11:09:23	N	145/21:03:12	4
141/21:00:24	1	143/11:49:23	N	145/21:43:36	1
141/21:40:24	1	143/12:29:23	U	145/22:23:36	2
141/22:20:24	1	143/13:09:23	N	145/23:03:36	1
141/23:00:24	1	143/13:49:23	N	145/23:43:36	3
141/23:40:24	1	143/14:29:23	U	146/00:23:36	3
142/00:20:24	3	143/15:09:23	U	146/01:03:36	1

Time	Code	Time	Code	Time	Code
146/01:43:36	1	147/23:08:13	S	148/23:40:46	S
146/02:23:36	1	147/23:48:13	S	149/00:52:48	N
146/12:21:24	U	148/00:28:13	S	149/01:32:48	N
146/13:01:24	U	148/01:08:13	S	149/02:12:48	N
146/13:41:24	1	148/01:48:13	S	149/02:52:48	N
146/14:21:24	U	148/02:40:17	N	149/03:32:48	N
146/15:01:24	U	148/03:20:17	N	149/04:12:48	N
146/15:41:24	U	148/04:00:17	N	149/04:52:48	N
146/16:21:24	1	148/04:40:41	N	149/06:37:35	1
146/17:01:24	1	148/05:20:41	N	149/07:17:35	S
146/17:41:24	N	148/06:00:41	N	149/07:57:35	4
146/18:21:24	1	148/06:40:41	N	149/09:03:24	1
146/19:01:24	1	148/07:20:41	4	149/16:15:08	N
146/19:41:24	1	148/08:00:24	N	149/16:55:08	N
146/20:21:24	1	148/08:40:24	N	149/17:35:08	U
146/21:37:02	1	148/09:20:24	N	149/18:15:08	1
146/22:17:02	1	148/10:00:24	N	149/18:55:08	1
146/22:57:02	1	148/11:22:17	U	149/19:35:08	1
146/23:37:02	1	148/12:02:17	N	149/20:25:10	1
147/10:44:24	3	148/12:42:17	N	149/21:05:10	1
147/11:29:05	3	148/13:22:17	U	149/21:42:24	1
147/12:09:05	U	148/14:02:17	N	149/22:22:24	1
147/12:49:29	U	148/14:42:17	N	149/23:02:24	1
147/13:29:29	U	148/15:22:17	N	149/23:42:24	S
147/14:09:29	U	148/16:02:17	N	150/00:22:24	1
147/15:30:05	U	148/16:42:17	N	150/01:02:24	S
147/16:10:05	U	148/17:22:17	N	150/01:42:24	1
147/16:50:05	N	148/18:02:17	N	150/02:22:24	2
147/17:30:05	N	148/18:42:17	4	150/03:39:10	1
147/18:10:05	S	148/20:20:46	N	150/04:19:10	1
147/18:50:05	4	148/21:00:46	N	150/04:59:10	1
147/20:26:08	N	148/21:40:46	N	150/05:39:10	1
147/21:06:08	S	148/22:20:46	S	150/06:19:10	2
147/21:46:08	S	148/23:00:46	S		

Code

Time: day/hour:minutes:seconds

1 : u_* less than zero

2 : variance of the vertical velocity fluctuations less than 0.01 $m^{-2}s^{-2}$

3 : bad thermistor values

4 : period does not contain full 40 minutes of data

5 : morning time situation where z/L was not representative of the stability through the tower

6 : fog

N : neutral

S : stable

U : unstable

APPENDIX D

σ_E, σ_A Functions of fz/u_*

That σ_E and σ_A are functions of ln fz/u_* can be justified on the basis of theory after making some appropriate assumptions and simplifications. It has been shown that

$$\sigma_E = \frac{\sigma_w}{U} \quad \text{(see Section XV)}.$$

In the Ekman layer,

$$\frac{U}{u_*} = \frac{U_g}{u_*} + \frac{1}{k} \ln fz/u_* + \text{const}$$

under conditions of a neutral, barotropic, horizontally homogeneous planetary boundary layer (see Blackadar and Tennekes, 1968). Since the tower heights represent the lower part of the Ekman layer, V = 0 is a valid assumption. This was assumed to be a boundary condition when the velocity defect law was derived.

A result of similarity theory is that the variance of the vertical velocity is a universal function of z/L. For near neutral conditions

$$\frac{\sigma_w}{u_*} = C \phi_w(z/L) = 1.25$$

(see Panofsky 1972; Busch and Panofsky, 1968). Thus

$$\sigma_E = \frac{1.25\, u_*}{U} = \frac{1.25}{\frac{U_g}{u_*} + \frac{1}{k} \ln \frac{fz}{u_*} + \text{const}} = \frac{1.25\, C_D^{1/2}}{1 + \frac{C_D^{1/2}}{k} (\ln \frac{fz}{u_*} + \text{const})},$$

where σ_E is in radians and $C_D = (u_*/U_g)^2$ is the geostrophic drag coefficient. Thus σ_E can be expressed as a function of ln fz/u_* and C_D after making a few simplifying assumptions and approximations. Knowing σ_E, C_D, and fz/u_* simultaneously will allow the unknown constant in the above equation to be calculated.

An analogous expression can be derived for σ_A.

APPENDIX E

The BWIB Lines

The expressions used for ϕ_m in this report are often referred to as the BWIB lines. They are:

$$\phi_m = (1 - \gamma\ z/L)^{-1/4} \quad , \ z/L < 0 \qquad \text{(E.1)}$$

and

$$\phi_m = (1 + 4.7\ z/L) \quad , \ z/L > 0. \qquad \text{(E.2)}$$

The value of the coefficient, γ, of z/L in Eqn. (E.1) is sometimes used as 16 and sometimes 15. The value, 15, is the most recent one by Businger (1971). However, for the purposes of this report, there is no significant difference between the plots using either value. Figure 65 is a plot of the Eqn. (E.1) and (E.2) using values of 15 and 16. The difference is too small to be seen on the computer produced plot.

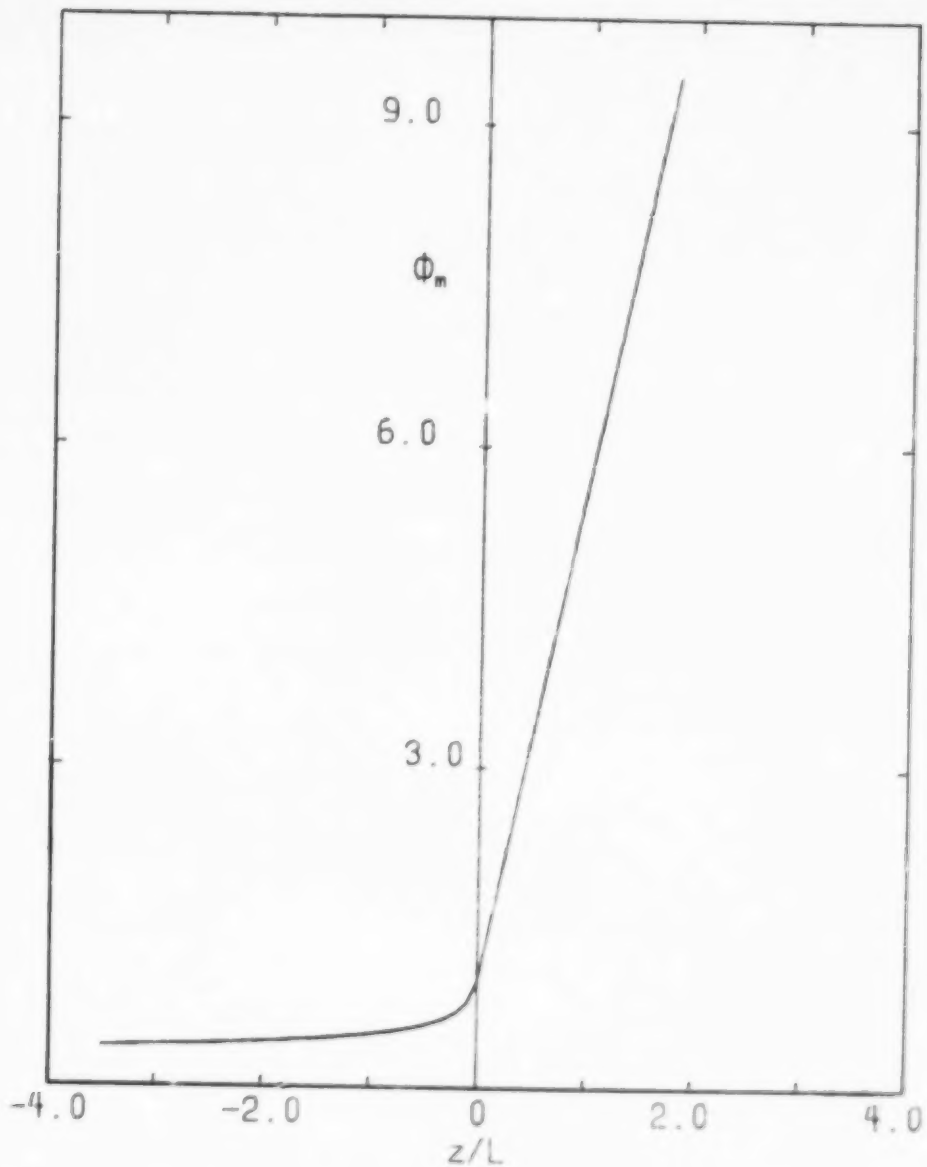

Figure 65. Nondimensional wind shear, ϕ_m versus z/L computed from the equations $\phi_m = (1 + 4.7\ z/L)$, $z/L > 0$; $\phi_m = (1 - 15\ z/L)^{-1/4}$, $z/L < 0$; and $\phi_m = (1 - 16\ z/L)^{-1/4}$, $z/L < 0$. The two curves on the unstable side are almost indistinguishable.